BRNO UNIVERSITY OF TECHNOLOGY

VYSOKÉ UČENÍ TECHNICKÉ V BRNĚ

CENTRAL EUROPEAN INSTITUTE OF TECHNOLOGY BUT

STŘEDOEVROPSKÝ TECHNOLOGICKÝ INSTITUT VUT

IN VIVO APPLICATION OF HOLOGRAPHIC ENDOSCOPY

IN VIVO APLIKACE HOLOGRAFICKÉ ENDOSKOPIE

DOCTORAL THESIS

DIZERTAČNÍ PRÁCE

AUTHOR — Mgr. Tereza Tučková

AUTOR PRÁCE

SUPERVISOR — Ing. Hana Uhlířová, Ph.D.

ŠKOLITEL

BRNO 2022

Abstract

The progress in understanding of complex brain function is conditioned by the ability to optically access any chosen structure and area in the living brain with minimal tissue damage and with sub-cellular resolution,

The progress in accessing deeper into the light-scattering tissue stands nowadays largely on the development of optical endoscopic probes such as microendoscopes with incorporated graded index (GRIN) lenses and fibre-optic bundles. Due to recent advancements in holographic light shaping methodology, using multimode optical fibres (MMF) as imaging elements has become promising for high resolution imaging deep in the tissue. In comparison to GRIN-based endoscopes and fibre bundles endoscopes, MMFs provide the highest ratio of image resolution and probe thickness causing minimal tissue damage.

This thesis first provides an overview of the current state-of-the-art *in vivo* deep brain imaging technology, multi-mode fibre-based endoscopy and its principles to introduce the related technology. The main technological focus of the thesis stands on using a digital micro-mirror device (DMD) to modulate light through the MMF probes. This enables fast raster scanning of the fluorescent sample at the imaging plane of the fibre distal facet. An optical setup exploiting this principle has been built, its imaging properties carefully evaluated, and high stability reached. Its imaging abilities have been demonstrated on 2D and 3D fluorescent phantom samples.

Consequently, we have developed an image post-processing procedure to enhance the detected image and reach the full diffraction-limited resolution potential. Using algorithms, one based on a regularised iterative inversion and second on regularised direct pseudo-inversion, lead to enhancement of the image contrast and resolution.
Further, we used genetically modified mice to move towards *ex vivo* and *in vivo* imaging. Suitable mouse models were identified and its *ex vivo* brain imaging showed that the images suffer from strong background fluorescent signal from out-of-focus planes. Therefore, further work focused on technological development for light attenuation based on the confocal principle.

An optical setup for confocal “pinhole” filtration has been built using a custom-made probe consisting of graded-index MMF spliced at the tip of the step-index MMF and a second DMD. The fluorescent signal collected by the GRIN-SI-MMF was filtered in the probe far field where for every scanning focal point it forms an annular ring. This ring-signal, and thus also the out-of-focus signal, was then separated using a mask on DMD2. On a set of experiments using phantom sample of fluorescent microspheres and fixed brain tissue it has been demonstrated that this confocal filtering leads to attenuation of the background signal, the signal from the out-of-focus planes thus enhancing the images contrast and resolution. This principle of confocal filtering in the holographic endoscope has been also demonstrated using a novel side-view MMF probe.

This work shows a piece of a puzzle in a long-term complex development of an optimal tool for deep-tissue and high-resolution imaging. The MMF-based holographic endoscope has been advanced to routine imaging of biological tissue in range of hours with the feature of

out-of-focus light attenuation. The endoscope has been tested on imaging of phantom samples as well as fixed mouse brain slices and *in vivo* vasculature down to depth of 5 mm.

Keywords

Holographic endoscopy, microendoscopy, optical fibre, multimode fibre, light modulator, digital micro-mirror device, transmission matrix, fluorescence imaging, computation image enhancement, mouse model, genotypization, tissue preparation, *ex vivo* imaging, confocal imaging, out-of-focus light suppression, *in vivo* imaging

Abstrakt

Pokrok v porozumění komplexním mozkovým funkcím závisí na schopnosti opticky dosáhnout jakékoli vybrané struktury a oblasti živého mozku se subbuněčným rozlišením při minimálním poškození tkáně.

Zpřístupňování hlubších oblastí tkání rozptylujících světlo je v současnosti umožněno zejména vývojem optických endoskopických sond, například mikroendoskopy s gradientními čočkami (GRIN) a svazky optických vláken. Pokrok v metodách holografické modulace světla dosažený v poslední době přinesl jako další nadějný směr pro zobrazování s vysokým rozlišením hluboko ve tkáních použití vícevidových optických vláken (MMF) jako zobrazovacích prvků. Ve srovnání s endoskopy založenými na GRIN čočkách a svazcích optických vláken poskytují MMF nejvyšší poměr rozlišení obrazu ku tloušťce sondy a způsobují minimální poškození tkáně.

Úvodní část práce poskytuje přehled o nejmodernějších technologiích hloubkového zobrazování mozku *in vivo*, vícevidové vláknové endoskopii a jejích principech s cílem představit související technologii. Hlavním technologickým zaměřením práce je použití digitálního mikrozrcátkového zařízení (DMD) k modulaci světla, šířící se MMF sondou. To umožňuje rychlé rastrování fluorescenčního vzorku v zobrazovací rovině za distální hranou vlákna. Byla sestrojena optická sestava využívající tohoto principu, bylo dosaženo vysoké stability a byly pečlivě vyhodnoceny zobrazovací vlastnosti. Ty byly demonstrovány na 2D a 3D fluorescenčních fantomových vzorcích.

Dále jsme vyvinuli metodu zpracování obrazu, zlepšující jeho kvalitu a umožňující dosáhnout plného potenciálu difrakčně omezeného rozlišení. Použití algoritmů využívajících regularizované iterativní inverze, případně regularizované přímé pseudoinverze, zvyšuje kontrast a rozlišení obrazu.

Další cestou k *ex vivo* a *in vivo* zobrazování bylo použití geneticky modifikované myši. Identifikovali jsme vhodné myší modely a *ex vivo* zobrazování mozku ukázalo, že snímky trpí silným fluorescenčním signálem pozadí z oblastí mimo ohniskovou rovinu. Proto se další práce zaměřila na vývoj technologie útlumu světla založené na konfokálním principu.

Byla sestrojena optická sestava pro konfokální filtraci "dírkovou clonkou" s použitím speciální sondy složené z MMF s odstupňovaným indexem lomu spojeného s MMF se skokovým indexem, a druhého DMD. Během zobrazování byl fluorescenční signál shromážděný GRIN-SI-MMF sondou filtrován ve vzdáleném poli sondy, kde se pro každý skenovací ohniskový bod vytváří prstenec. Prstencovitý signál se pak oddělí pomocí masky na DMD2, čímž se také oddělí signál pocházející z ohniska od signálu vznikajícího mimo ohnisko. Na experimentech s použitím fantomového vzorku fluorescenčních mikrokuliček i fixované mozkové tkáně bylo prokázáno, že toto konfokální filtrování vede k zeslabení signálu pozadí, tedy signálu z mimoohniskových rovin, čímž se zvyšuje kontrast a rozlišení snímků. Tento princip konfokální filtrace v holografickém endoskopu byl rovněž demonstrován pomocí nové MMF sondy s bočním zobrazováním.

Práce ukazuje jen kousek skládačky dlouhodobého komplexní vývoje optimálního nástroje pro hloubkové tkáňové zobrazování s vysokým rozlišením. Holografický endoskop využívající MMF byl zdokonalen tak, že může sloužit k rutinnímu několikahodinovému zobrazování biologických tkání s možností útlumu světla pocházejícího mimo ohniskovou rovinu. Endoskop byl testován při zobrazování fantomových vzorků i fixovaných plátků myšího mozku a *in vivo* cév až do hloubky 5 mm.

Klíčová slova

Holografická endoskopie, mikroendoskopie, optické vlákno, vícevidové vlákno, modulátor světla, digitální mikro-zrcátkové zařízení, přenosová matice, fluorescenční zobrazování, výpočetní vylepšení obrazu, myší modely, genotypizace, příprava vzorku tkáně, zobrazování *ex vivo*, konfokální zobrazování, potlačení světla z oblastí mimo ohniskovou rovinu, zobrazování *in vivo*

Acknowledgment

I would like to express my sincere gratitude towards my supervisor Dr. Hana Uhlířová for introducing me to the world of neuroscience and microscopy, for her patient, thorough and forthcoming supervision and guidance through my whole Ph.D. study. She has been a great mentor to me, always ready and keen to discuss various scientific problems. I am grateful for all the advancement, professional and personal, I have made because of her.
My sincere gratitude also belongs to prof. Tomáš Čižmár for the opportunity to be part of the project and research team. I am glad he was the thought-leader of the project and that he was constantly creating a nurturing environment for the team to function. I am grateful to prof. Pavel Zemánek for allowing the project to nest at the Institute, for taking care of the environment and everything necessary for the research. I would like to thank also my colleagues – Dr. Martin Šiler, Dr. Petr Jákl, Dr. Sergey Tuartev, Dr. Dirk Boonzajer Flaes – for sharing their experience and wisdom, and to MVDr. Petra Ondráčková who guided me through the world of laboratory animals, gave me courage and with her enthusiasm motivated me to advance further.
I will always remember and be thankful my closest colleagues - Tom Pikálek and Mirek Stibůrek – whose support, friendship and attitude always pushed me a step further.
I am also especially thankful to prof. Radim Chmelík, whose research group I used to be a part of, for all the care and support, for scientific discussions and advice and for allowing us to use the group's lab.
My eternal thanks go to my husband Marek for immediate and intense support and to my whole family for always being there for me.
I am grateful to CEITEC BUT and ISI ASCR for supporting my studies, courses, conferences and professional growth.

The European Regional Development Fund-Project Holographic endoscopy for in vivo applications (CZ.02.1.01/ 0.0/ 0.0/ 15_003/0000476, LO1212); European Commission (101016787, CZ.1.05/ 2.1.00/ 01.0017) and CAS (L01212, CZ.1.05/2.1.00/01.0017, RVO:68081731 are gratefully acknowledged for the support of this work.

I declare that I have written this thesis entitled *In vivo application of holographic endoscopy* independently, under the guidance of the supervisor, Ing. Hana Uhlířová, Ph.D., and using the technical literature and other sources of information, all adequately cited in the thesis, with a detailed list of references provided at the end of the thesis.

Mgr. Tereza Tučková

Contents

1. Introduction

Since the origin, there has been a strong desire to understand what is the essence of humankind. What is the drive that gives people desires, ideas, and cravings for the understanding of life and the universe? Already in Ancient Egypt four thousand years ago, the human body was studied in morphology and physiology. However, due to the limited opportunities in those times, it was feasible only postmortem and by observation of the human behavior. Therefore, to explain and describe the very principle of brain function was impossible. It was not until the blossoming of science at the end of the 19th century before a significant progression in the field of neuroscience happened. The advancement in microscopy, labelling of the tissue, imaging using X-rays and electroencephalography enabled to reveal the structure of the brain and indirectly record its activity for the first time.

In the second half of the 20th century, the rapid progress in molecular biology, biochemical processes, electrophysiology, and computational methods enabled to study connectivity between single neurons. The neuronal study offers an expansion of our understanding of social evolution as well as cognitive and behavioral development or the process of making decisions. Due to the ever increasing precision of technology, a rapidly growing number of patients became diagnosed with neurodegenerative diseases such as Alzheimer's and Parkinson´s as well as with epilepsy, migraine strokes, and others. This motivates an urgent need for understanding of brain mechanism and its functional connectivity. Most of these pathologies are difficult to study *ex vivo*, therefore the progress of neurological/neurobiological research has greatly depended on technology enabling to exploit animal models. Among all animal models, mouse became the most popular because of its small size, fast reproduction cycle, yet up to ~85% conformity of protein-coding regions with the human [1].

The current non-invasive methods, which can also be used in humans, such as computation tomography (CT), positron emission tomography (PET), nuclear magnetic resonance (NMR), or ultrasound enable to investigate the structural changes or in the case of functional magnetic resonance imaging (fMRI) functional processes and connectivity in the brain. These techniques yield macroscopic information from the whole brain due to their high penetration, however with limited resolution sufficient for distinguishing of individual cells, as summarized in Fig. 1.1.

Very soon it became clear that understanding the cause and early pathogenesis of neuronal diseases requires studying the underlying structural and functional changes on a cellular and sub-cellular level.

Current *in vivo* neuroscience research meets these needs mainly via optical microscopy providing high-resolution structural and functional imaging. However, optical methods suffer a fundamental trade-off between the penetration depth and resolution (Fig.1.1). To overcome this depth limitation, optical probes, such as endoscopes have to be used.

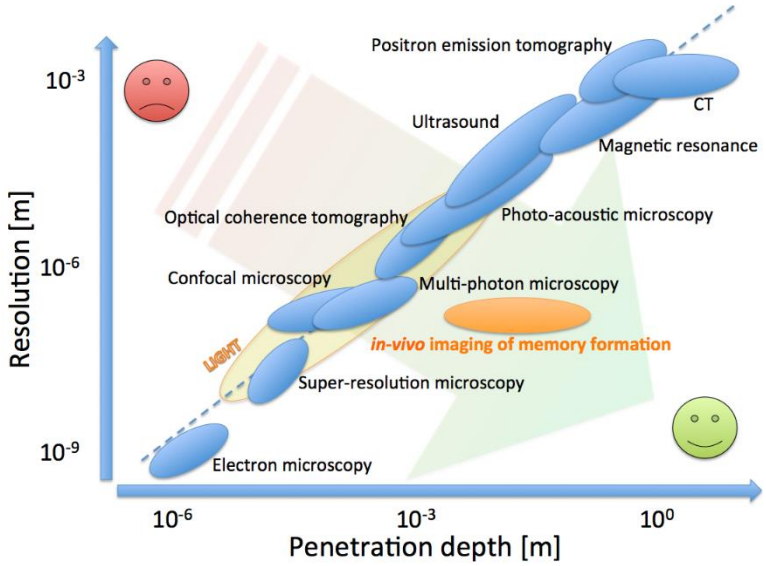

Figure 1.1: The trade-off between resolution and penetration depth for methods of biomedical and biological imaging. Reprinted from [2].

1.1 Current state-of-the-art optical methods for *in vivo* imaging in neuroscience

Light provides exquisite sensitivity to capture brain structure and function via intrinsic changes in absorption, scattering, or through the use of extrinsic contrast. Technological advancements in light laser scanning microscopy, digital acquisition, combination with electrophysiology, and progress in fluorescence labelling methods in the last two decades have enabled monitoring the activity of thousands of cells with their interactions within brain circuits with cellular or even sub-cellular resolution [3]. This has enabled us to study e.g. memory function through the examination of hippocampal circuits [4, 5], record intracellular Ca^{2+} dynamics of hundreds of individual neurons and astrocytes in live animals [6, 7, 8], study the relation between the brain´s neuronal network and its vessels – the neurovascular interactions [9, 10], the cerebral blood flow [11], vascular oxygenation during the hemodynamic response in relation to neuronal activity [12], migraine [13] and others. These and other studies bring us closer to understanding of the brain function in its complexity as well as on the level of individual cells and vessels.

1.1.1 Limits of optical imaging

One of the main challenges for optical technology is to acquire high-resolution images from deep within the brain *in vivo*. The optical methods presented in this work use for signal excitation scanning with a laser beam focused into a focal point. The quality of obtained resolution is intrinsically linked to the numerical aperture of the optical system and the wavelength of the illumination laser, as well as the refractive index of the imaging medium or sample. The optimal resolution of the imaging system is limited only by diffraction and is given by the size of the minimum focal point. The focal point takes a shape of an Airy disc – a bright spot surrounded by concentric rings. The size of the Airy disc is determined by the wavelength of the light and the size of the circular aperture

of a perfectly aligned system. Often, the Rayleigh resolution criterion is used to define the resolution limit for a diffraction-limited system: two point-sources are regarded as just resolved when the central maximum of one Airy disc coincides with the first minimum of the other one. The following equation defines the distance of such two point sources in the object space

$$R = 0.61\frac{\lambda}{\mathrm{NA}}, \tag{1.1}$$

where λ is the wavelength of the illumination beam and NA is the numerical aperture of the objective defined as $n \cdot \sin\theta$, where θ is an acceptance angle measured from the optical axis and n refractive index of the medium. The resolution limit along the optical axis can be described by the axial resolution of the focused point. It can be defined with Rayleigh criterion as well [14]: two point-sources are regarded as just resolved when the zero-order diffraction maximum of one Airy disc coincides with the first minimum of the other one. The following equation defines such distance in the space

$$R = \frac{2\lambda}{\mathrm{NA}^2}. \tag{1.2}$$

The depth to which the light can penetrate is affected by the optical properties of the sample. Living tissue is an optically turbid heterogeneous medium with a complex variety in the refractive index, absorption and high scattering properties which result in attenuation of the propagated light. This can be characterized by an attenuation coefficient $\mu_t = \mu_s + \mu_a$, as the sum of the scattering μ_s and absorption coefficients μ_a [15]. Scattering of light in most biological tissues is much more prominent compared to absorption; hence the absorption coefficient is often neglected, and the light attenuation is determined only by scattering $\mu_t = \mu_s$ [16]. The scattering coefficient depends on the wavelength and tends to decrease for longer wavelength in tissue. The dependency can be approximated empirically as

$$\mu_s \sim A\lambda^{-SP} \tag{1.3}$$

where A and SP are model parameters for scattering amplitude and scattering power, respectively [17, 18, 19, 20]. SP determines how strong the scattering changes with wavelength. and is related to the average size of the scatterers. In our case, we only consider the elastic scattering of light on the specimen when the photon energy is unchanged upon its deflection from its original direction. If the scattered objects are much smaller than the propagated wavelength (such as isolated atoms, molecules in a gas or membranes), the scattering is strongly dependent on wavelength with SP = 4 [15, 21] and is referred to as the Rayleigh scattering. Light scatters also on objects larger than the wavelength of light (mitochondria, nuclei, cells) but the dependency on the wavelength is weak in this case.

The change of the intensity of the scattered light can be described as an exponential attenuation with imaging depth along the optical axis (z) and, following Lambert-Beer´s law, expressed as

$$I = I_0\, e^{(-\mu_s z)} \tag{1.4}$$

where I_0 is the intensity of the incident light [15, 16]. The strength of the scattering is often described by the mean free path – the scattering length, by which the intensity of incident light decreases by a factor of $1/\mathrm{e}$. Substitution of $\frac{I_0}{e}$ into Eq. (1.4) yields the scattering length $z_{scat} = \frac{1}{\mu_s}$. Empirically measured, the scattering length is in the range ~20-100 μm for visible light [22] and ~220 μm for near-infra red light (NIR) [23, 24]. Imaging at depths of ~500 μm below the brain surface suffers hence from multiple scattering events, thus limiting the achievable contrast. These fundamental limits motivate a massive effort to develop imaging modalities robust to light scattering. The following sections offer a description of some of the most successful methods.

1.1.2 Confocal microscopy

Confocal microscopy exploits an optical process involving a single photon absorption followed by the emission of a single fluorescence photon of a longer wavelength. Thus, it is a linear optical technique where the probability of absorption of one photon depends on the incident light intensity linearly [25, 16]. Confocal microscopy has been developed to enable the imaging of thick samples, such as tissue sections. This technique effectively suppresses the light from planes other than the imaging one (the out-of-focus light), which has revolutionized fluorescence microscopy [26, 27, 28]. For the illumination, it uses a laser beam focused into a spot, and by the movement of a galvanic mirror, it is scanned within the sample across the focal plane. This is why it is often referred to as a confocal laser scanning microscopy (CLSM) [28, 29, 30]. The confocal microscope's essential part is the pinhole acting as a spatial filter at the conjugate image plane positioned directly in front of the detector, thus effectively forming a point detector. The pinhole rejects the photons emitted from out-of-focus areas or scattered photons. The blocked signal does not contribute to the image which dramatically improves contrast and the resolution [29, 30, 28]. Since the pinhole rejects a large part of the detected photons, high-intensity light sources need to be used for fluorescence excitation and sensitive detectors such as the photomultiplier tubes (PMT) for detection. A beneficial consequence of using the confocal pinhole is optical sectioning. The image is a two-dimensional optical section, which is created by scanning the focused beam across a transversal plane in the sample piecing together information from each individual focal point. By scanning planes at different axial positions a 3D reconstruction of the sample can be obtained [29, 31, 30].

The intensity function for the point object imaged by a confocal microscope is equal to the square of the intensity function for a conventional microscope. Therefore, the resolution of both systems is the same according to the Rayleigh criterion because zero points have identical positions. However, if we assess the resolution by the full width of the half maximum of the intensity function, the resolution of the confocal microscope is improved by a factor of $\sqrt{2}$, assuming the confocal pinholes have a negligible size with respect to the size of the Airy disc [34, 28, 33].

When using confocal microscopy, the lateral and axial resolutions can reach values around 180 nm and 500 nm, respectively [35, 32]. With the increasing imaging depth, the contrast of the image decreases very quickly. It is thus possible to image up to one to two scattering lengths.
Worth of noting is the fact that although the detected photons come from a thin optical section, the fluorescence is excited in the whole illuminated volume. Moreover, stronger illumination is needed with a decreasing size of the pinhole. The whole illuminated volume suffers therefore by photobleaching and phototoxicity as the tissue is repeatedly illuminated. [36].

1.1.3 Multiphoton microscopy

Multiphoton microscopy is currently a well-established microscopy technique for deep imaging within the intact brain or bulk tissue. It is a nonlinear technique involving multiple photons´ absorption followed by the emission of a fluorescent photon. The required energy for a molecule excitation is obtained by the absorption of multiple photons virtually simultaneously (within <1 fs). The photons usually have the same energy, nevertheless the excitation by the photons of different energies has been presented recently [37]. To provide a high peak flux of excitation photons and thus increase the probability of their absorption in a single quantitised event, multi-photon microscopy uses femtosecond pulsed lasers. During absorption, cumulated two or more photons combine their energies to promote the molecular transition, while their individual energies are relatively low. This enables the multi-photon microscopy to use excitation light of longer wavelengths, typically in the NIR range which are less scattered in biological tissue. This leads to a greater penetration depth compared to visible light (Fig. 1.2) [38, 39].

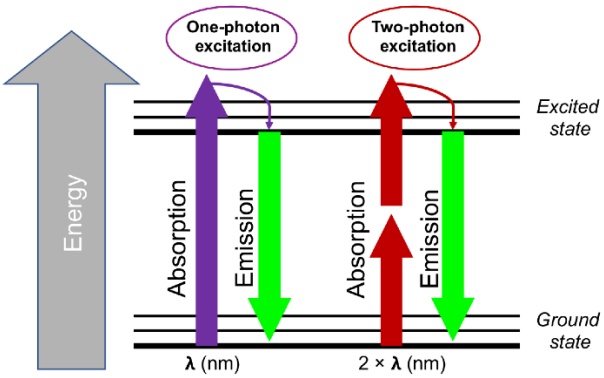

Figure 1.2: Jablonski Diagram representing the energy composition for single- and two-photon excitation. Reprinted from [40].

In the multiphoton excitation processes, the probability of absorption of more photons, is considered nonlinear because the rate at which it occurs, depends on the light intensity nonlinearly [41]. More specifically, the signal depends supralinearly on the light intensity, as $S \propto I^n$, where n corresponds to the number of photons involved in an absorption process/in the elementary process [16, 38].

Two-photon microscopy, which has been mostly used in the last two decades exploits excitation of two photons simultaneously. The probability of absorption is thus quadratically dependent on the incident intensity. The total fluorescence F_{total} generated from an illuminated plane A depends on the square of excitation light intensity $F_{total} \propto A\, I^2$. The illumination intensity can be expressed as a ratio between the incident laser power P and the illuminated crossectional area A, which is proportional to the square of the axial distance z from the focal plane, as $I = \frac{P}{A} \propto \frac{P}{z^2}$) (Fig. 1.3) [39]. Therefore, the total fluorescence can be expressed in equation as

$$F_{total} \propto AI^2 \propto \frac{P^2}{z^2}. \tag{1.5}$$

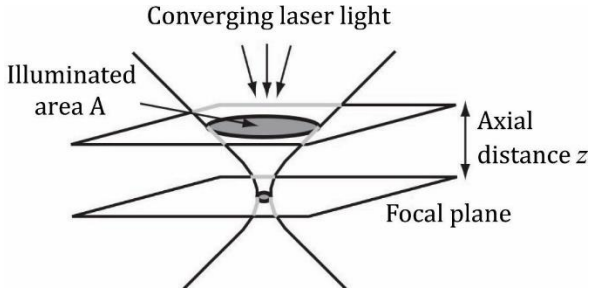

Figure 1.3: Illustration of the laser light near the focus of an objective. The shaded regions indicate the cross-sectional area in a given plane, normal to the direction of propagation, that is illuminated by the converging laser light. The illuminated cross-sectional area is seen to decrease as the distance to the focal plane decreases. Reprinted from [39].

Assuming that the energy flux is constant in every plane, the intensity of the excitation beam changes with a factor $\frac{1}{z^2}$. This results in the excitation process localized only in the small volume centred at the focal plane. Scanning such focus across the imaging plane yields an optical section inherently, without the need of the confocal pinhole. All fluorescence photons emitted from the focus can be therefore detected which results in an increased collection efficiency compared to the confocal detection. Moreover, only the fluorescence in the focal volume is excited and therefore the overall phototoxicity and photobleaching is reduced. Locally, in the focal plane, the phototoxicity and photobleaching can be however higher than in the single-photon process.

Due to the fact that two-photon microscopy uses NIR wavelength for the excitation, it enables to image down to the penetration depth of ~750 μm below the brain surface [16, 38, 42]. Thus, it greatly surpasses the single-photon microscopy in the imaging depth. An optical parametric oscillator (OPO) can extend wavelength of some lasers thus offering a tuneable wavelength up to ~1300 nm. This excellent source of radiation provides extended spectrum range, under which the scattering is even less significant and regions below depth of ~750 μm can be reached. It has been demonstrated that two-photon microscopy with the use of OPO can reach an imaging depth of 1.6 mm using prolonged 1280 nm wavelength [43].

Lasers with wavelengths around ~1300 nm and longer are used for three-photon microscopy, which brings with it the abovementioned greater penetration depths

for imaging. The dependence of the probability of photons absorption during a three-photon excitation on the incident intensity is cubic. Therefore, another advantage is, similar to two-photon microscopy, that although the emitted fluorescence photons are detected from the given focal spot, their amount is reduced away from the focal plane by the factor of $\frac{1}{z^4}$. Thus, the three-photon excitation reduces the out-of-focus signal even stronger and the phototoxicity is more localized than in the case of two-photon excitation. It has been demonstrated that with three-photon microscopy one can achieve high-resolution *in vivo* imaging at depth from ~1.100mm [44] up to ~1.600 mm below the brain surface [45, 46].

The multi-photon microscopy is currently the primary choice for optical far-field microscopy of brain *in vivo*. However, many structures important for higher brain functions, such as cognition and learning, lie below the achievable depth limit of multi-photon microscopy. One of the potential solutions would imply surgically removing the part of the tissue lying above the region of interest [47]. This approach however is very invasive and interferes with the physiology and function of the brain [48].

1.1.4 Micro-endoscopy

Micro-endoscopes are thin optical, usually rigid probes of 350-2000 μm in diameter. They guide the light to the hardly accessible areas of the tissue, and thus enable deep tissue imaging, also *in vivo*. Micro-endoscopes, despite their diversity in design and principle, primarily act as optical relays, and through them, several imaging techniques have been accomplished deep inside the brain, such as two-photon microscopy [49, 62], epifluorescence [50, 51], confocal [52, 53, 54], light-sheet microscopy [55] and super-resolution imaging [56].
Few relevant types of micro-endoscopes and their operating principles are introduced in the following chapters.

Endoscopy using GRIN lenses

One prominent type of micro-endoscopes is based on a gradient index (GRIN) miniature rod-like lenses with a parabolic profile of the refractive index [57]. They are mimicking Hopkins´ concept of conjugated lenses relaying the image from one facet of the probe to another.
The microendoscopic probes are formed by up to three GRIN lenses (singlet/doublet/triplet) – an objective lens, a relay lens, and a coupling lens (see Fig. 1.4). The GRIN probes are embedded into the brain tissue delivering illumination and relaying the emitted photons of fluorescence signal from one end of the probe (structure in the tissue) to another (microscope objective). All three types of GRIN probes can be conceptualized as two optical components in series: a micro-objective with an infinite tube length focusing the illumination to the sample and collecting the emitted signal and a relay lens receiving focused illumination and backward focusing the signal to the front focal

plane of the microscope´s objective. For the doublet, the GRIN relay microlens is coupled to a GRIN micro-objective. The relay microlens project a real image of the fluorescent sample collected with micro-objective to the microscope objective´s focal plane without needs of a coupling lens. Both functions occur within one optical element in the case of a singlet GRIN lens [58, 61].

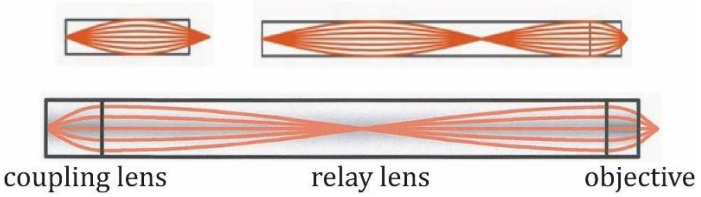

Figure 1.4: Different types of GRIN probes – singlet, doublet and triplet. Reprinted from [58].

The GRIN lenses are characterized by their length and numerical aperture NA. In the case of the triplet or doublet type, the relay lens has a smaller NA compared to the coupling and objective lenses, which leads to a longer axial length for full oscillations in beam diameter – pitch length. Thus, the probe has a sufficient length for reaching the desired depth in the sample [61].

The GRIN micro-endoscopes are commercially available with numerical apertures reaching up to ~0.8 and diameters ranging from 0.35 to 2.8 mm. For example, it has been tested and demonstrated by multiphoton fluorescent imaging using triplet GRIN lenses of various diameters of 1, 0.5 and 0.35 mm, that the lateral resolution can reach 1.26, 1.84 and 2.86 μm, respectively [58, 59]. Also, it has been demonstrated that using the GRIN microendoscopes of total diameter 1 mm one can reach lateral and axial resolution of ~1.21 μm and ~9.8 μm respectively [63], and ~0.85 μm and ~7.4 μm, respectively for 2-photon imaging [64]. For 3-photon microscopy was demonstrated resolution of ~1 μm and ~9.5 μm, respectively with the GRIN microendoscope of 1 mm as well [65]. It has been tested GRIN microendoscope of diameter 350 μm protected by a metal sheat thus having total diameter of 600 μm with multiphoton microscopy to reach lateral and axial resolution of ~1 μm and ~10 μm, respectively [62]. The urgent need for minimazitation of the microendoscope diameter has led to the latest demonstrated imaging through the ultra-thin GRIN microendoscope of total diameter of 350 μm with assembled aspheric lenses microfabricated with 3D micro-printing. Thus with 2-photon imaging we reached a resolution under 1 μm [60].

It has been successfully implemented in high-resolution *in vivo* laser-scanning imaging in animals [66, 60, 62] as well as in humans [67].

Even with advances in the development of index profiles optimized for imaging, the resolution of the system is more limited by optical aberrations within the endoscope probes rather than by diffraction [68]. Due to the shape of the index profile, the effective NA is not uniform across the facet; therefore, the highest resolution which can be achieved is restricted to the central region of the lens and strongly decreases towards the edges [69]. The pitch length of GRIN depends on the wavelength, which is the source of GRIN chromatic aberration [68]. Adaptive optics can provide correction of the aberrations [70, 71, 72, 73]. For example, for the case of two-photon microscopy through the GRIN

endoscope, the diffraction-limited performance recovery has been demonstrated with the use of the pupil-segmentation-based adaptive optics [72, 73].
Endoscopes with GRIN lenses have been successfully implemented for example in single-photon, two-photon [49, 74] or three-photon excitation microscopy [58, 62]. Miniaturization of the adjacent microscope components led to the development of head-fixed endo-microscopes for imaging in freely behaving animals using multi-photon [75, 76, 77, 78] or single-photon [79] excitation. GRIN lens-based microendoscopes are nowadays one of the significant tools for *in vivo* imaging of deep brain structures beyond the reach of multi-photon microscopy. In most cases, however, they require aspiration of part of the tissue lying above the location of interest, due to high diameter of the microendoscope, which can significantly interfere with the physiological function of the surrounding tissue or even the tissue under study [80].

Endoscopy using optical fibre bundles

A flexible alternative to rigid GRIN rod-probes are fibre bundles. The bundles diameter typically varies between ~80-300 μm, in some cases even up to a few millimetres, and their length is not limited by optical aberrations, thus enabling imaging in deep regions of the sample.
Fibre bundles are constructed from thousands of thin, densely packed single-mode optical fibres (SMF) of core diameters ~3-7 μm with a relatively low numerical aperture (~0.22), where each of them can transfer only a single spatial mode of light, one image pixel value at a time. Therefore, only packed together, they enable to obtain an image information (Fig. 1.5). The cores of SMFs in the bundle are isolated from each other by cladding of a lower refractive index preventing the propagated signal from different locations of the object from cross-talk.

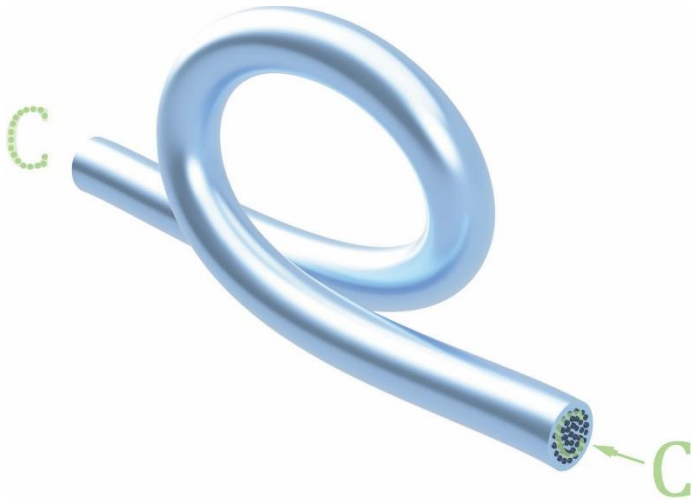

Figure 1.5: Transmission of the image in the fibre bundle consisting of many spatially separated cores. The light from the letter C is propagating only through the spatially separated cores placed within the cladding, all packed within one probe.

However, due to spatial separation of the cores of the SMFs (~3 μm or more), the detected light collection efficiency is low [82] and the images suffer from inherent pixelation

artefact leading to low lateral resolution [81, 82]. In the initial *in vivo* studies, it has been demonstrated that commercially available bundle probes of a diameter of 160 μm (1600 cores) cannot offer sufficient resolution for imaging of neuronal sub-cellular structures [83, 84]. To increase the resolution, magnifying optics (a set of microlenses [85] or a GRIN lens [86]) can be attached to the end of the bundle on the sample side. The probe size is preserved; however, the field of view gets smaller.

Several scanning techniques were implemented through the fibre bundles, for example confocal microscopy [53, 87]. By illuminating the input facet of the bundle, in the illuminated specimen plane is a whole FOV of a single spatial modes [53, 88, 89]. The same core can also act as a pinhole detector rejecting the out-of-focus light [89, 90, 91, 92]. However, there is still light loss due to the small NA of the single fibre cores and their spatial separation. Another approach is to add a miniature scanning mechanism – MEMS scanner at the input side of the fibre bundle and scan each of the SMF by the laser beam [93, 94]. These techniques enable an increase of resolution, due to added magnifying optics at the distal end of the fibre bundle and their total diameter (reaching up to several millimetres). The insertion of such endoscopes requires surgical removal of a significant volume of brain tissue, compromising again, the physiology [95].

Endoscopy using Step-Index (SI) Multi-Mode optical fibres (MMFs)

The strong invasiveness of the tissue removal for deep *in vivo* imaging can lead to mechanical lesions of the tissue compromising the physiology of neuronal networks and the behaviour of the animal [96, 97]. This was behind the search for a probe of a much smaller diameter which however would be capable of providing sub-cellular resolution. A promising prospect for this purpose is the use of multimode optical fibres (MMF), as summarized in Fig. 1.6. Multimode optical fibres are thin waveguides made of fused-silica glass (SiO_2) of high chemical purity. Step-index MMFs are comprised of a glass core surrounded by a cladding of a different glass with a lower refractive index. Thus, they form a closed cylindrical refractive index boundary serving to entrap the light. It is then guided in the core by total internal reflection. When coherent light enters the MMF, it is coupled into many propagating modes. The number of modes depends on the core diameter, refractive indices of the core and the cladding, and the wavelength of the propagated light. The MMF can guide through the core above 10 000 modes up to hundreds of thousands [98]. Therefore, it has a much larger information capacity, compared to a SMF. Also, the whole core is a light-guider which is beneficial for the efficiency of light collection. The whole NA of the MMF can be utilized and the image resolution is defined only by the wavelength of the propagated light and the NA and is fundamentally limited only by diffraction [99, 100, 93, 101, 102, 103]. The core of a MMF has a diameter typically in the range of ~10-1500 μm and the whole probe reaches the diameter in the range of ~110 - 1550 μm. The NA of MMFs can reach high values up to ~0.9 [104].

When the light arrives at the fibre input facet, only the rays of an incident angle within the cone defined by the acceptance (aperture) angle θ_a are coupled and propagate through the fibre in the form of propagating modes. The acceptance angle, measured from the optical axis, can be described as

$$\theta_a = \text{asin}NA \tag{1.6}$$

where NA is the numerical aperture of the fibre [57]. The MMF acts like a complex medium in which the light is subject to the process of multiple scrambling. The light rays propagate through the fibre in optical paths carrying the information, with different group velocities and the propagated rays come out with different phase shifts resulting in a speckle pattern. This prevents using the MMFs as an imaging element. However light transport through MMFs remains deterministic. Advances in wavefront control through highly scattering or turbid media, which use methods of digital holography, thus have opened the possibility of transferring images across a MMF [105, 100, 106, 107]. The development of digital holography methods allows modulating the coherent light and thus enables creation of the focus and imaging through this complex medium – MMF [100, 102, 108, 109]. The wavefront modulation technique has motivated and has been exploited in combination with approaches including iterative algorithms [109, 110], time-reversal [111, 112] or phase conjugation [113, 114], and the concept of transformation matrix (TM) [108, 115].

Among the described endoscopic probes, MMFs provide the highest resolution to probe thickness ratio (see Fig. 1.6). Thus, the MMF can much better serve as an atraumatic probe and can be inserted deep into the brain tissue. The use of probes of diameters up to ~200 μm does not require surgical removal of the tissue above the deep region of interest. For *in vivo* imaging, MMFs with a core diameter of ~50 μm and ~0.22 NA have been mostly used [103, 116, 117] down to 4 mm under the brain surface with lateral resolution of ~1.2 μm [103]. Since the MMF can guide light over several kilometres, there is no fundamental limit on the achievable penetration depth. All these features make MMFs excellent candidates for endoscopic probes for deep imaging of neuronal structure and function with sub-cellular resolution.

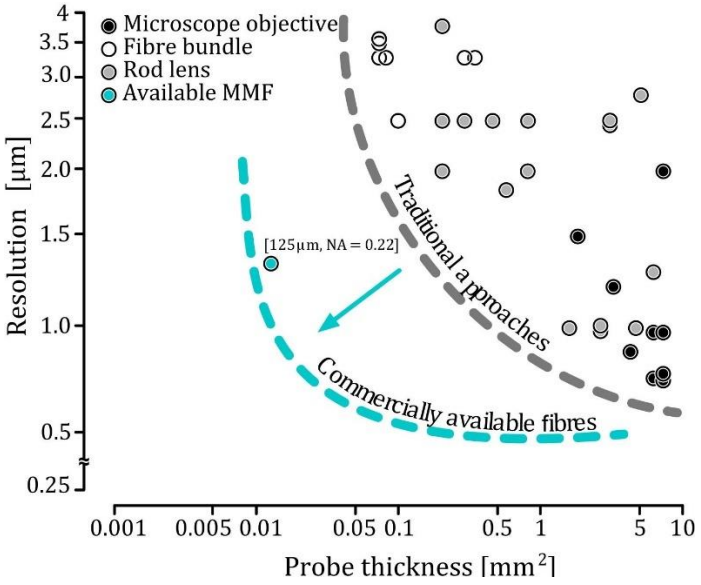

Figure 1.6: The relation between probe thickness and its resolution across the commercially available microendoscopes. Reprinted from [116].

1.2 Summary of the thesis

This Ph.D. work focuses on the development of imaging methods applied via the MMF-based endoscope for deep *in vivo* brain imaging.

The first part presents the current state-of-the-art optical techniques, which have also been used in this work. In the next part, the basics and principles of holographic endoscopy are introduced.

In the Result section, I first described the basic setup replicated in Brno according to the published work of the research group [103]. The imaging performance is demonstrated on fluorescent 2D and 3D model samples such as fluorescent micro-spheres and the USAF target. To enhance the image quality, two computational algorithms are introduced which enable to reconstruct the sample with increased contrast and resolution.

The collected knowledge has served as the starting point for building a setup of a new generation for *in vivo* brain studies in mouse models. Consecutively as the next step, Further, I present selected mice lines which represent the best available models for imaging along with their preparation and surgical procedures. Neuronal imaging of fixed brain slices revealed that despite sparse fluorescence expression high resolution imaging may be difficult due to the out-of-focus light imaged inherently in all one-photon excitation techniques.

This motivated our effort to implement one of the strategies for out-of-focus light attenuation. The last part of this thesis introduces a holographic endoscope which exploits a custom-designed probe spliced from two types of MMF for confocal filtering of the detected signal. The principle is demonstrated on both phantom samples as well as brain tissue.

1.3 Aims of the thesis

The following aims has been specified at the beginning of the PhD studies.

1. Holographic endoscopy through MMF

The first aim of the dissertation work is to build the multimode fibre-based holographic endoscope. The set-up should be designed according to the published work of the research group [103]. The set-up should be tested on model samples such as fluorescent beads and resolution targets. The performance of the setup imaging should be characterized with an appropriate metrics. Experience with this setup should serve as the starting point for building a setup of new generation for in vivo brain studies in mouse models.

2. Preparation for animal surgery

The second aim is establishing and testing of protocols for animal brain surgeries necessary for the endoscope fibre implantation. In the first step, the endoscopy will be carried out in acute experiments on anesthetized animals. In the next step, a protocol for chronic imaging in awake animals should be developed.

3. *In vivo* imaging and out-of-focus attenuation via MMF-based endoscopy

The third aim of the dissertation work comprises implementation of the endoscope setup as well as the developed animal preparation protocols in high resolution of deep brain structures and potentially functions *in vivo.* Suitable genetically modified mouse models have to be selected and the imaging of fluorescence deep in the tissue demonstrated. Imaging should be performed on anesthetized animals and potentially extended to awake head-fixed animals.

2. Holographic endoscopy based on MMFs

Although a MMF can transport the intensity information, it cannot relay the whole object´s image at once as a lens. When the wavefront of coherent light enters the fibre, the MMF behaves like a complex turbid medium and the light comes out as a speckle pattern. However, the light coupled to the waveguide´s modes propagates through the fibre, still carrying the information. In order to use MMF as an imaging tool, it is necessary to characterize the light propagation through this turbid medium. Using wavefront shaping, the scrambling of light in a MMF can be measured and corrected for in a way that the fibre becomes an optical relay. Then, it can be used to transmit and collect images similarly to scanning microscopy.

2.1 Light propagation through a multimode optical fibre

The propagation of the modes through the MMF varies based on the type of fibre, which can be a step-index (SI-) or gradient-index (GRIN-) MMF. Using MMFs as relay elements for imaging requires measurement and characterization of the propagated light through the fibres.

A step-index MMF (SI-MMF) is a cylindrical dielectric waveguide defined by constant refractive indices of two different values for the core (n_1) and the cladding (n_2). The common SI-MMF probes used for imaging have core diameters of 50 - 200 μm where the total diameter varies from 125-400 μm [118].
The modes propagating through a SI-MMF are solutions of the Helmholtz equation for the distribution of the electromagnetic wave. They are defined by the Cartesian components of electric and magnetic fields as well as their axial component. The solution of such wave propagation through the space along the optical axis is characterized by a propagation constant β. Each mode propagates with a different propagation constant.
Advanced theoretical description and experimental methods have demonstrated that MMFs behave like a highly predictable systems [57, 102].
It has been experimentally confirmed that the cylindrical symmetry gives the origin to mutually orthogonal propagation-invariant modes (PIMs). Each PIM has a characteristic field distribution in the transversal plane and a distinct propagation constant, which is conserved during propagation through the MMF. It has been shown that circularly polarized PIMs remain unaffected in their amplitude and phase by propagation through the SI-MMF. Therefore, the input and output phase of every PIM is preserved. Thus, they can enable the possibility to perform imaging with theoretically predicted fibre characterisation. This knowledge was beneficial for the light manipulation when the fibre band and thus the light propagation is distorted into chaos again [57, 102].

Light coupled into the fibre core is defined by the acceptance (aperture) angle θ_a. The modes then propagate within the fibre by total reflection of the core-to-cladding interface. The acceptance angle is thus crucial and can be described by the relation in Eq. (1.6),

where NA is the numerical aperture of the fibre defined by the refractive indicies of the core (n_1) and cladding (n_2) as NA = $(n_1{}^2 - n_2{}^2)^{1/2}$. The light entering the fibre input facet at angles larger than θ_a can be refracted into the core, but since the modes do not undergo total internal reflection, they propagate only for a short distance.

With respect to the electromagnetic nature of the light, we can determine the number of the modes supported by the fibre (single-mode or multi-mode) using the normalized frequency (V number) of the optical fibre

$$V = 2\pi \frac{d}{\lambda_0} \text{NA}. \tag{2.1}$$

Parameter d is the diameter of the core, λ_0 is a light wavelength and NA is the numerical aperture of the fibre. For MMF, the V number reaches high values ($\gg 1$), and the number of supported modes M of both polarizations traveling simultaneously can be estimated as

$$M \approx \frac{V^2}{2}. \tag{2.2}$$

Depending on the coupling angle, each mode propagates through the fibre with a different trajectory along the core axis with a different phase velocity. At the output, modes meet in one plane with different phase shifts yielding a speckle pattern (Fig. 2.1). However, this pattern is not very suitable for fluorescent imaging. It is necessary to manage this mode's dispersion at the output.

Figure 2.1: Coherent light coupled to the MMF exits as a spackle pattern due to different phase velocities of different propagating modes.

The light propagation through the MMF is considered a deterministic and linear system [115, 119]. Therefore, it can be analytically described, and the phase shifts can be compensated for by modulation of the phase and amplitude of the input wavefront. A linear operator transforming the input into the out wavefront is typically referred to as the transmission matrix (TM) [115].

2.2 Transmission matrix

The transmission matrix (TM) describes the relation of the optical light field at the input facet of the MMF (at the same time called a proximal facet to the DMD) and the output facet (distal facet to the DMD). It provides linear transformation between the input and output complex fields [115]. The components of the TM are thus complex numbers – changed phase and amplitude of the propagating light. Theoretically, the MMF has no backscattering; therefore, the TM is considered unitary [102].

The TM is practically measured by decomposing both complex fields into orthogonal bases of input and output modes. The input base can contain localized focal points or plane waves with varying incident angles [100, 102]. We measure the TM using input points on the facet and output points from the facet imaged into corresponding pixels on a camera (Fig. 2.2).

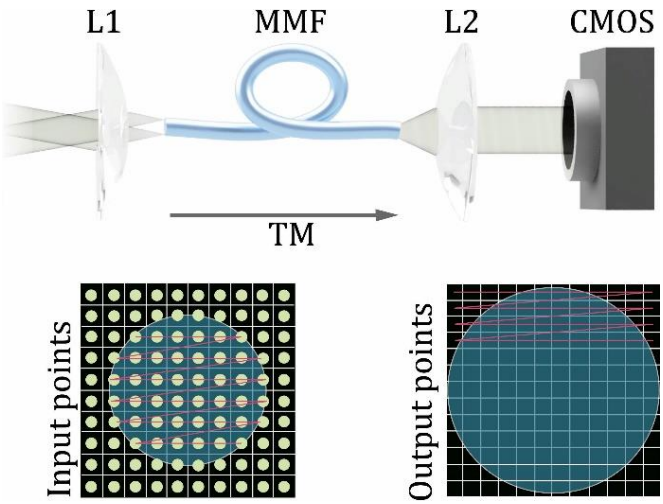

Figure 2.2: Orthogonal bases of input and output points used for TM measurement. The lens L1 focuses the beam which scanned across the input facet of MMF in the form of input points during the TM measurement. The outcoming light is then collimated with lens L2 onto chip of the camera (CMOS) (top panel). Illustration of the bases of the input points across the input fibre facet and the grid of the pixels of the camera creating an orthogonal base of output points (bottom panel).

Each output point (E_m^{out}) is then defined as

$$E_m^{out} = \sum_n t_{mn} E_n^{in}, \tag{2.3}$$

where t_{mn} are complex coefficients of the TM and E_n^{in} is the complex amplitude of the optical field in the n^{th} input point [107, 104, 115]. An example of an experimentally measured transmission matrix is shown in Fig. 2.3. Values of amplitudes and phases of each output point measured for all single input points are written into each row.

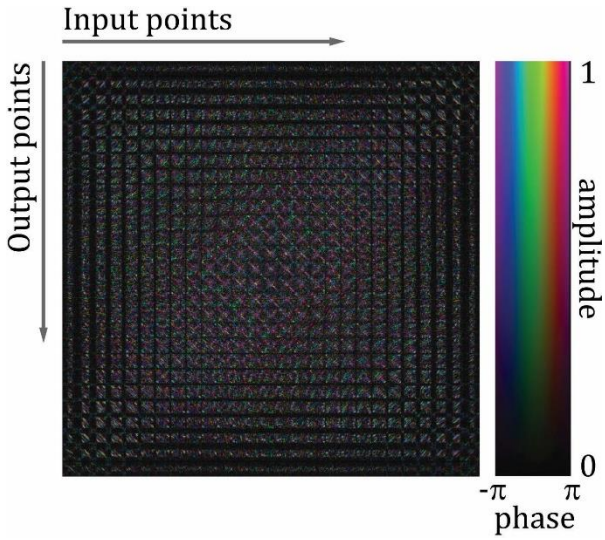

Figure 2.3: The example segment of measured transmission matrix with complex coefficients [102].

Measurement of the TM requires optical access to the distal end of the fibre. This measurement needs to be performed every time the configuration of the fibre changes. This is limiting; however, there are already some initial studies on how to obtain the TM without access to the distal end, for example, on the basis of numerical modelling [120]. The modelling approaches are however beyond the scope of this thesis and the TM will be measured always through at the distal end of the MMF.

2.3 Light modulation using a digital micro-mirror device (DMD)

Wavefront manipulation can be achieved using two of the most commonly used modulators: liquid crystal-based spatial light modulator (LC-SLM) or an optical microelectromechanical system MEMS-based SLM, e.g. digital micro-mirror device (DMD). SLMs modulate the wavefront via retardation of its phase. DMDs are, on the other hand, pure amplitude binary modulators, but they also can be used effectively for phase modulation using diffraction of light [121]. Both modulator types have their advantages and disadvantages. Here I summarize some important features affecting the quality of the wavefront modulation which determine the quality of the focal spot at the distal end of the MMF.

The DMD is a high-resolution amplitude modulator, typically used in complex photonics in an off-axis regime. The DMD chip consists of hundreds of thousands of micro-mirrors. Each mirror can tilt to a state “on” (1) or “off” (0) and corresponds to a single pixel in the displayed image. The resolution of commercially available DMD climbed up to 2048x1152 pixels [122, 123, 124, 125].

DMDs operate as purely binary amplitude modulators, posing a limit to the precision and efficiency with which each degree of freedom (equal to the number of independently controllable pixels on DMD) can be controlled [126, 127]. The DMD allows only about 8% of the whole optical power to be sent into the MMF [121].

It has been demonstrated that the DMD does not suffer from random light scattering that is present in LC-SLM and contributes to an incontrollable background signal. When modulating the light using DMD and since the DMD has been often used in a regime of phase-only modulation, the intensity in the created focus at the output of the fibre increases and the modulation of light in this focus reaches efficiency of 75% [101,121]. This is higher compared to LC-SLM (60%) [121]. Recently it has been demonstrated that DMD can be used for a complex modulation of the wavefront. The efficiency can be increased up to 96% [128].
The DMDs operate at a several kHz frame rate, up to 22 kHz, which is more than 100x more than the LC-SLMs. This is also one of the main reasons why DMDs are the first choice for biological imaging applications where temporal resolution is essential [129, 130].

Although the LC-SLM are able to diffract light with much higher efficiency, the DMDs have been shown to outperform them in wavefront modulation due to a faster refreshing rate as well as in beam-shaping fidelity. Thus, the overall efficiency of the DMD wavefront modulation is higher compared to LC-SLM modulations [121].

In holographic wavefront modulation, the DMD chip acts as a diffractive grating with each micromirror individually controlled by a computer, thus providing a means for a binary computer-generated hologram (CGH). Such hologram diffracts light into diffraction orders given by the hologram spatial frequency. A light diffraction of the grid of mirrors is resolved as convolution of these mirrors creating grid of sinuses stripes. For calibration, a set of single-frequency diffraction grating in DMD plane is used (Fig. 2.4). A lens placed at a focal distance from the DMD transforms the diffracted light into points in the DMD´s Fourier plane.

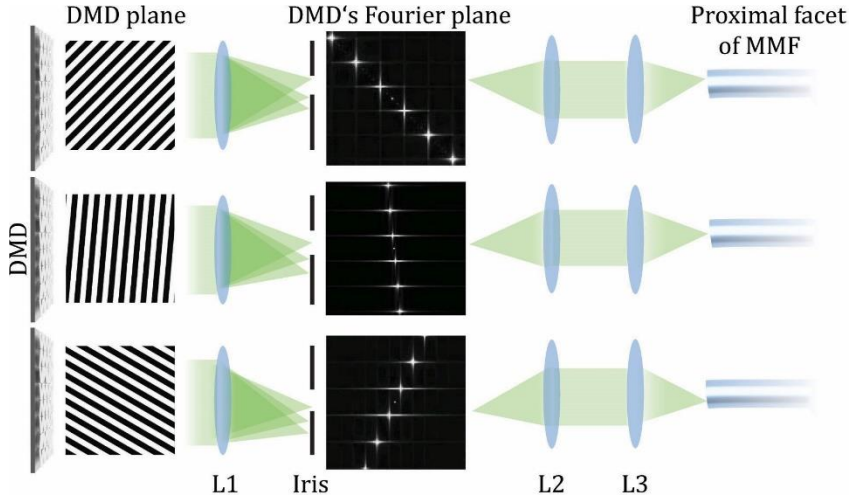

Figure 2.4: A simplified principle of the light diffraction of a single-spatial frequency hologram. The light diffracts on the grating displayed on the DMD into diffraction orders which are imaged by the lens L1 into the DMD´s Fourier plane. The iris diaphragm selected 1st order here. Lenses L2 and L3 image the Fourier plane on the proximal (input) facet of the MMF. Changing the diffraction grating results in the change the position of the focused point at the input facet.

Here the 1st diffraction order is selected by an iris diaphragm and further used to modulate both the phase and potentially also the amplitude of the wavefront [131]. The phase is manipulated by a local lateral shift of the grating and the amplitude via variation of the duty cycle. The Fourier plane is then imaged and demagnified using a 4f system on the fibre input facet creating input points in the calibration process. Scanning these points is realized by change of the carrier spatial frequency of the diffraction grating.
A linear combination of single-frequency linear gratings is used for generating a field of arbitrary phase modulations on the input facet of the MMF.

2.4 Optical setup

The optical setup in Figure 2.5 uses a single-frequency coherent laser emitting light at 532 nm. The laser beam propagates through a Faraday optical isolator suppressing the light reflected backwards from the further optical components and sharping the desired linear polarization of the laser. A set of a half-wave plate (H1) and a polarization beamsplitter (PBS) controls the total power sent into the system. Another half-wave plate H2, together with the polarization plate beamsplitter (PBSW) divides the laser beam into the signal and reference beam. Half-wave plates H3 and H4 are used to align the polarization of the light with respect to the single-mode polarization-maintaining optical fibre (SMF1 and SMF3), into which the light is coupled using aspheric lenses L1 and L2.
The output signal beam from the SMF2 is collimated with a lens L3 so that it overfills the DMD. It illuminates the DMD with an incidence angle of 30° from the DMD chip normal. This angle corresponds to the maximum power deposited into the 1st diffraction order which is used for imaging.
Each micromirror of the DMD in the "on" state (+12°) diffracts the beam into the optical system, while mirrors in the "off" state (-12°) send the light out of the optical path. The lens L4 focuses the diffracted beam into the Fourier plane of the DMD where an iris selects the first diffraction order. A combination of the lenses L5 and L6 demagnify the hologram far-field on the proximal facet of the MMF. The lenses L4 and L5 underfill the aperture of lens L6 and thus reduce its effective numerical aperture to match the NA of the MMF (0.22). The combination of polarisation plate P, half-wave plates H5 and H6 and quarter-wave plate Q1 enable to reach a pure circular polarisation state of light entering the MMF. Circular polarisation is better preserved than linear while propagating through a straight segment of a MMF [102]. Thus, at the MMF output, another quarter-wave plate (Q2) changes the polarization back to the same linear polarisation state. The speckle pattern is magnified by the set of the objective (Obj., Olympus 20x, NA = 0.40) and the lens (L7) on a camera (CMOS, acA640-750um, Basler ace). The reference-beam polarization is aligned with the signal polarization on the camera to maximize the contrast of the interference pattern.
At the beginning of each experiment, or after the replacement of the fibre, it is necessary to calibrate the system, i.e. measure a new TM.

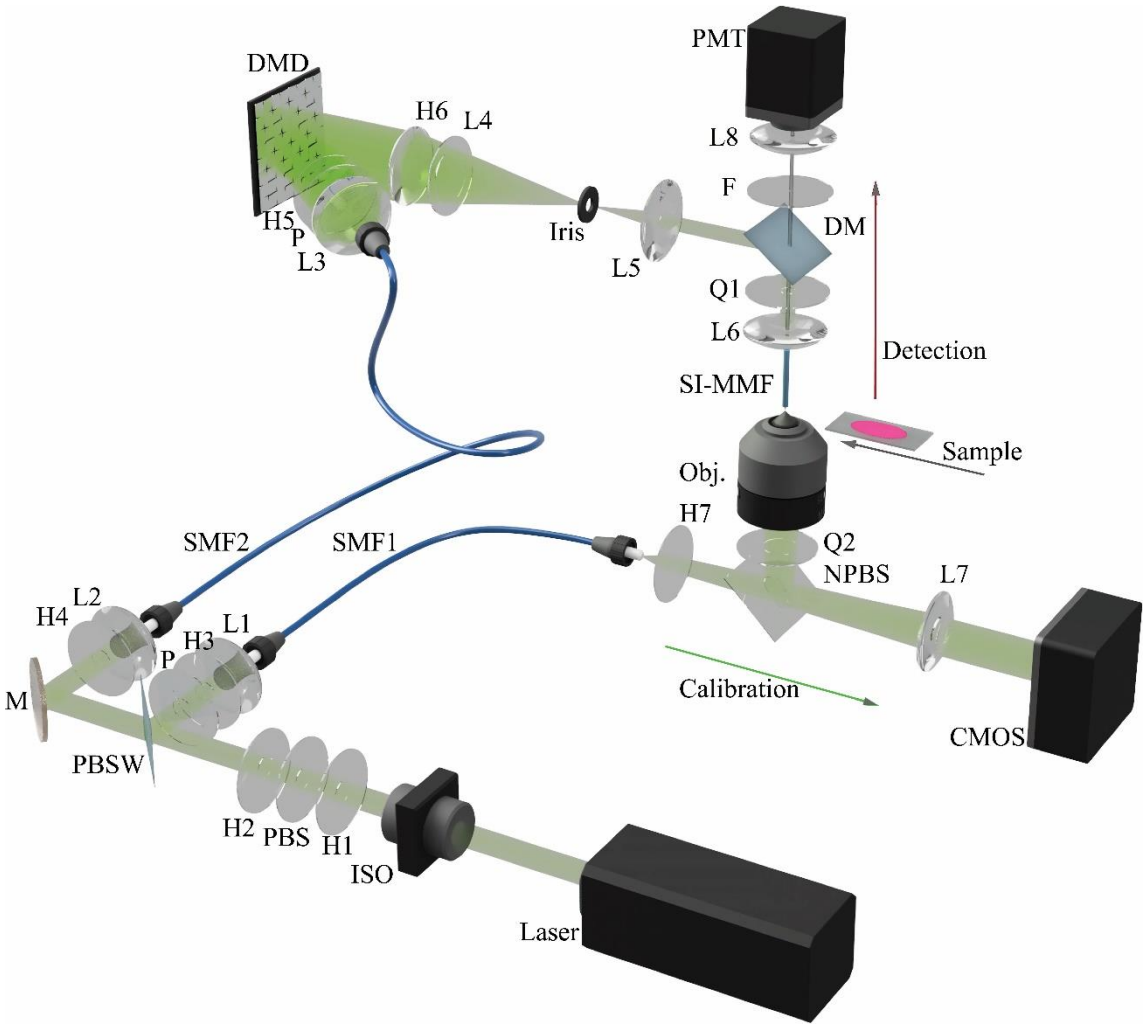

Figure 2.5: Experimental setup with the calibration module and detection path: **Laser:** Coherent Verdi G-Series 532nm; **M:** Mirror BB1-E01, Thorlabs. **L1, 2**: Lens C240TME-A, Thorlabs. **L3, 5, 8**: Achromatic Doublet AC254-075-A-ML, Thorlabs. **L4, 7**: Achromatic Doublet AC254-150-A-ML, Thorlabs. **L5:** Achromatic Doublet AC254-075-A, Thorlabs. **L6**: Achromatic Doublet, AC254-080-A-ML, Thorlabs. **H1-H7**: Multi-Order Half-Wave Plate WPMH10M-532, Thorlabs. **Q1,2*:*** Multi-Order Quarter-Wave Plate, WPMQ10M, Thorlabs. **PBS:** Polarizing Beam Splitter, CCM1-PBS25-532/M, Thorlabs. **PBSW:** Polarizing Plate Beamsplitter PBSW-532, Thorlabs. **P:** Linear polarizer LPVISE 100-A, Thorlabs. **DM:** Dichroic mirror, Chroma, **F:** Filter ET525/50, Semrock. **NPB:** Non-polarizing Beamsplitter Cube BS016, 50:50, Thorlabs. **SMF1:** single-mode optical fiber maintaining polarization, PM SMF, SQS Vláknová Optika, PM460-HP. **SMF2**: Single Mode Fibre P3-488PM-FC-2, Thorlabs. **ISO**: Isolator Tornos Serie 500-1030nm (04-532-00012). **DMD**: Digital micro-mirror device V-7001 (DLP 7000, Texas Instruments), ViALUX. **Iris**: Iris diaphragm SM1D12C, Thorlabs. **SI-MMF**: Step-Index Multimode Fibre FG050LGA, Thorlabs. **Obj.:** Objective, Olympus 20x, NA = 0.22. **CMOS**: Camera Ace acA640-750um, Basler. **PMT**: Photomultiplier Tube PMT2101/M, Thorlabs.

Firstly, the MMF´s distal facet is immersed into a medium with the refractive index matching the refractive index of the sample closely. For the measurement of the TM we need to define the number P of the input modes covering entirely the area of the input fibre

facet. This can be done as follows. For the experiments we use step-index MMF with a cladding diameter of 125 μm, core diameter of 50 μm, and NA equal to 0.22.

For the wavelength $\lambda = 532$ nm, the V parameter for this fibre can be calculated using Eq. (2.1) and is equal to ~130. The number of the modes of the MMF for both polarizations is calculated from Eq. (2.2) and is equal to ~8450. To calculate the number of modes (input points) scanned on the Fourier plane, first, we choose lenses, which demagnify the beam of the DMD onto our MMF. The aspheric lenses L4 and L5, in their combination, underfill the aperture of the aspheric lens L6 and thus reduce its effective numerical aperture, better matching the numerical aperture of the MMF. The calculation of the size of the Fourier window and number of input points is done using the following equations.

The lenses L5 and L6 with the focal lengths f_5 and f_6 (75 mm, 10 mm) image the diffraction pattern from the Fourier plane to the fibre facet. We can calculate the diameter of the fibre facet image at the Fourier plane (where the iris is placed) as

$$D = d\frac{f_5}{f_6} \tag{2.4}$$

where *d* is the diameter of the fibre. Using the MMF of the core with a diameter of 50 μm and the presented lenses, the diameter *D* is 375 μm. The DMD creates the diffraction pattern in the Fourier plane with a pitch (period of the grating) giving the distance of individuals input points, defined as

$$p = \frac{\lambda f_4}{r_{DMD} p_{DMD}}, \tag{2.5}$$

where r_{DMD} is the resolution of the DMD obtained from the chip, where we chose the square of 768x768 mirrors. The p_{DMD} is a pitch size of the DMD equal to 13.7 μm, defining the distance between centres of the two neighbouring mirrors. The f_4 is the focal length (150 mm) of the lens L4 focusing the beam into the Fourier plane and λ is the wavelength of the propagating beam. The pitch *p* of the grating in the Fourier plane is thus equal to 7.6 μm. We want to fill a circle of a diameter *D* into a square grid (with pitch *p*). We calculate the window with an inscribed circle – the fibre image in the Fourier plane of the diameter *D*. The number of pixels of such window is than

$$P = \frac{D}{p} = \frac{375}{7.6} \cong 50 \text{ pxl} \tag{2.6}$$

The Fourier window in the square of 50x50 pixels^2 contains 2500 input points, which can be imaged on the proximal fibre facet.

Use of the inscribed circle, however, results in undersampling the NA of the MMF. For the needs of calibration, we need to fill the NA. Therefore, we need to obtain bigger window (with more input points), resulting in larger region of interest (ROI) on the proximal facet of the MMF. For that case we can define factor *O*, by which we multiple the

size of the calculated Fourier window. It can be defined as the ration between the theoretical number of points and the modes carried by the optical fibre. We can define the theoretical number of input points using equation for next steps

$$N = \frac{1}{4}\pi\left(r_{DMD}p_{DMD}\frac{d}{\lambda}\frac{f_5}{f_4 f_6}\right)^2. \tag{2.7}$$

The combination of the lenses f_4, f_5 and f_6 magnify the NA on the DMD chip as a circle of the diameter defined as

$$r_{DMD}p_{DMD} = 2\frac{\mathrm{NA}f_4 f_6}{f_5} \tag{2.8}$$

However the circle is of small diameter, therefore to fill the DMD chip we need to define lenses f_4, f_5 and f_6 and their ratio, which can be expressed from Eq. 2.8 as

$$\frac{f_5}{f_4 f_6} = 2\frac{\mathrm{NA}}{r_{DMD}p_{DMD}} \tag{2.9}$$

which is than use for expressing the theoretical number of input points filling the circle on the DMD chip, put into Eq. (2.7) resulting as

$$\mathrm{N} = \frac{1}{4}\pi\left(r_{DMD}p_{DMD}\frac{d}{\lambda}\frac{2\mathrm{NA}}{r_{DMD}p_{DMD}}\right)^2 = \pi\left(\frac{d\mathrm{NA}}{\lambda}\right)^2. \tag{2.10}$$

The number of modes (points) carried by our MMF is derived from the Eq. (2.2) as

$$\mathrm{N_m} = \frac{1}{4}\left(\frac{d\mathrm{NA}}{\lambda}\right)^2 \tag{2.11}$$

which is only for one linear polarisation, which we us in our setup. Then we calculate the ratio between the input points (the theoretical one and the real ones which can fibre carry) as

$$\frac{\mathrm{N}}{\mathrm{N_m}} = \frac{4}{\pi} = O. \tag{2.12}$$

By this factor *O* we than multiple the size of the Fourier window from the Eq. (2.6), which give us the size of the window to be created with the number of the input points needed for the oversampling the NA of the MMF. We obtain the size of the window on the fibre facet as a grating of 64×64 pxl^2.

To calculate the precise value of the numerical aperture of the lens L4 we first calculate the size of the beam on the back-side of the aperture of the lens L6

$$B_m = r_{DMD}p_{DMD}f_5/f_4 \tag{2.13}$$

which is used in the final equation for the L6 numerical aperture

$$\mathrm{NA}_{L6} = \sin\left(\operatorname{atan}\left(\frac{B_m}{2f_6}\right)\right). \tag{2.14}$$

Using the lenses with $f_4 = 150$ mm, $f_5 = 75$ mm and $f_6 = 10$ mm, the NA_{L6} is equal to 0.25, which is satisfactory for the use of MMF with NA equal to 0.22.

The output field of the fibre core at its distal end is magnified using the lens L7 ($f_7 = 150$ mm) and imaged on the camera detector (CMOS). The choice of the output points number subjects to the size of the focal spot at the output facet, the number of pixels of the camera and the magnification of the output field onto the camera and the size of the spot on the camera. The size of the output point taken into account for sampling the pixels on the camera is given by the resolution given by our fibre, calculated by Eq. (1.1). Respecting the Rayleigh resolution is thus 1.475 μm (radius of Airy disc). However, the real size of the focal spot at the output fibre facet is given by the full width at half-maximum of the peak

$$\mathrm{FWHM} = \frac{0.51\lambda}{\mathrm{NA}} = 1.233\ \mu\mathrm{m} \tag{2.15}$$

The pixel size of the camera is 4.8×4.8 μm^2. After magnification, the point is imaged on the camera with the size of $s = 1.475 \cdot 15 = 22.125$ μm. The sampling of the point on the camera is thus ~5 pxls/point. The diameter of the focused fibre core imaged on the camera is equal to 750 μm. The sampling frequency is subject to the Nyquist sample criterion; therefore, the output points are sampled within the grid of 224x224 pxls^2.

As a result, we measure the TM between ~4100 input and ~50 200 output points in the calibration process.

2.5 Calibration procedure

In our case, the calibration procedure is performed by interference measurement. First by moving the objective, we determine the focal plane for the calibration – the distance of the MMF facet, which is for our type of MMF typically set to ~30 μm. After propagation, the output field is imaged on the camera. There the measurement of the output points phase modulation proceeds using interference with external reference beam. Using the principle of phase-shifting interferometry, we modulate and measure each phase of every input point and alter mutual shifts of the outcoming light from the fibre and the reference light at the output spot (pixel) on the camera and compensate for them. Thus, we can define how to change phase and amplitude of the input point to reach a maximal constructive interference in a particular output point (pixel) on the camera.

First step is illustrated in Fig. 2.6. We need to define the input field whose input points are coupled into the MMF. Using the DMD, we create an orthogonal base of the input points, which scan the Fourier plane and as described previously the input fibre facet. After propagation, the output intensity is imaged on the camera, and we integrate the total output intensity across all camera pixels. We assign the value into the position of each input point.

This resulting intensity image is then thresholded at 20% of the maximum. This creates a "mask" (Fig. 2.6 red ring) for the input points, which are than efficiently coupled into the fibre core. This input points will be used later for the TM measurement.

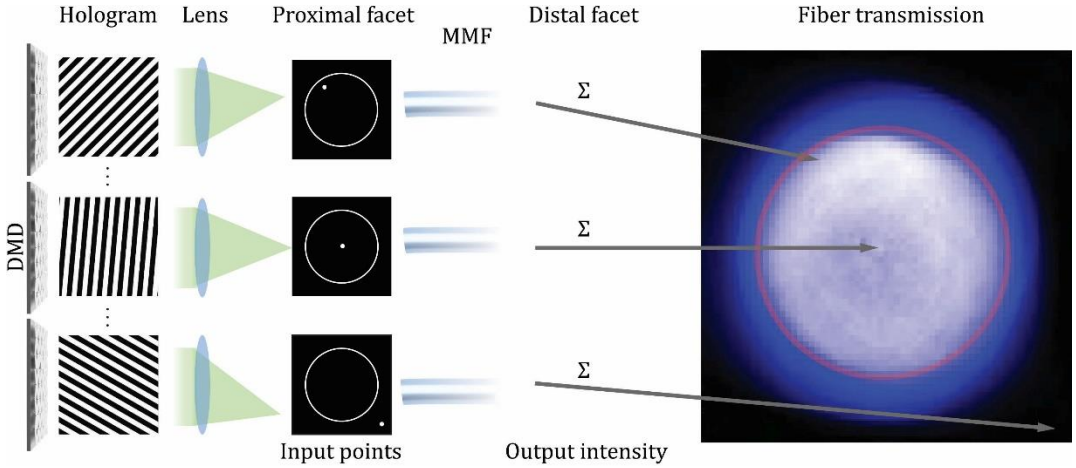

Figure 2.6: Input and output points are selected based on the sum of the total intensity of the light transmitted through the fibre.

The output points are defined in a grid created on the camera. The output field at the distal end of the MMF is magnified imaged and centred on the chip of the camera. The centred area used for the sampling is the grid with inscribed circle (output field) of the size 224×224 pxl². Each pixel in this grid is assigned to each output point/Each output point is assigned to each pixel in this grid.

As a next step, we measure the phase shift of the light in every output point for every single input point. The phase of output modes is measured using phase-shifting interferometry.

The phase of input points is shifted by $\pi/2$ in eight steps ($\alpha = 0, \pi/2\,, \pi, 3\pi/2$) sampling the intensity cycle two times (as illustrated in Fig. 2.7). The intensity I of the output point m is given from Eq. in [115] as

$$I_m^{\alpha} = |E_m^{out}|^2 = \left| S_m + \sum_n e^{i\alpha} t_{mn} E_n^{in} \right|^2, \tag{2.16}$$

where S_m is the complex reference amplitude in the m^{th} output mode and t_{mn} are the complex coefficients of the TM, where n is the n^{th} input point. The input points are measured sequentially, while output modes are measured simultaneously on the camera. Thus, the intensity of the interference I in every output point (image pixel) can be expressed as

$$I = I_{ref} + I_{sig} + \sqrt{2 I_{ref} I_{sig}} \cos\left(\varphi_{ref} - \varphi_{sig}\right). \tag{2.17}$$

We denote $I_{ref} + I_{sig}$ as B, $\sqrt{2 I_{ref} I_{sig}}$ as A and $(\varphi_{ref} - \varphi_{sig})$ as φ. The phase shift φ is calculated from measured intensity I in Eq. (2.17) multiplied with the corresponding phasor for each step and summed over all steps

$$F = \sum_{\alpha}^{N} \{[A\cos(\varphi + \alpha) + B]e^{i\alpha}\}, \tag{2.18}$$

where, α $(0, \pi/2\,, \pi, 3\pi/2)$ is the phase step and N = 4. Further,

$$F = \sum_{\alpha}^{N=4} \left(\frac{A}{2}e^{i(\varphi+\alpha)} + \frac{A}{2}e^{-i(\varphi+\alpha)} + B\right)e^{i\alpha}, \tag{2.19}$$

$$F = \sum_{\alpha}^{N=4} \left(\frac{A}{2}e^{i\varphi}e^{i\alpha} + \frac{A}{2}e^{-i\varphi}e^{-i\alpha} + B\right)e^{i\alpha}, \tag{2.20}$$

$$F = \sum_{\alpha}^{N=4} \left(\frac{A}{2}e^{i\varphi}e^{i2\alpha} + \frac{A}{2}e^{-i\varphi} + Be^{i\alpha}\right). \tag{2.21}$$

The sums $\sum_{\alpha}^{N=4}\frac{A}{2}e^{i2\alpha}$ and $\sum_{\alpha}^{N=4}Be^{i\alpha}$ equal zero. Thus

$$N\frac{A}{2}e^{-i\varphi}. \tag{2.22}$$

The amplitude A is calculated as a measured amplitude from the sinus from the Fig. 2.7. These values of each output point measured and calculated for all single input points are written into each row of the TM. After every phase-stepping cycle for a single input mode, the central input mode is illuminated as a reference in order to correct for an overall slow phase drift between the signal and the reference. This drift may be caused, e.g. by temperature changes and vibrations.

The last step is to create the holograms to be projected on the DMD that will generate output focal points. From the measured TM the corresponding row for particular output point is selected, inverted and resized into the shape of the input points. Then the inverse Fourier transform is applied to calculate the field on the DMD.
Since we modulate only the phase of the light beam, we calculate the Lee hologram given by [128, 131] as

$$O(x,y) = \frac{1}{2} + \frac{1}{2}\mathrm{sgn}\left\{\cos[\Phi(x,y)] - \sqrt{[1 - A^2(x,z)]}\right\}, \tag{2.23}$$

where (x, y) are Cartesian coordinates in the plane of the DMD chip, $\mathrm{sgn}(x)$ is the signum function and Φ is the phase at the DMD calculated as an angle of the complex value from the Fourier transformation of the TM. A is a thresholded amplitude, which value is in the case of the phase-only modulation equal to 1 [128]. The calculated hologram is then binarized.

The binary hologram pattern is displayed on the DMD. The selection of different rows of the TM will yield focal points in different locations in the image plane. Sequential formation of focal points in a square grid mimics scanning of a classical scanning microscope.

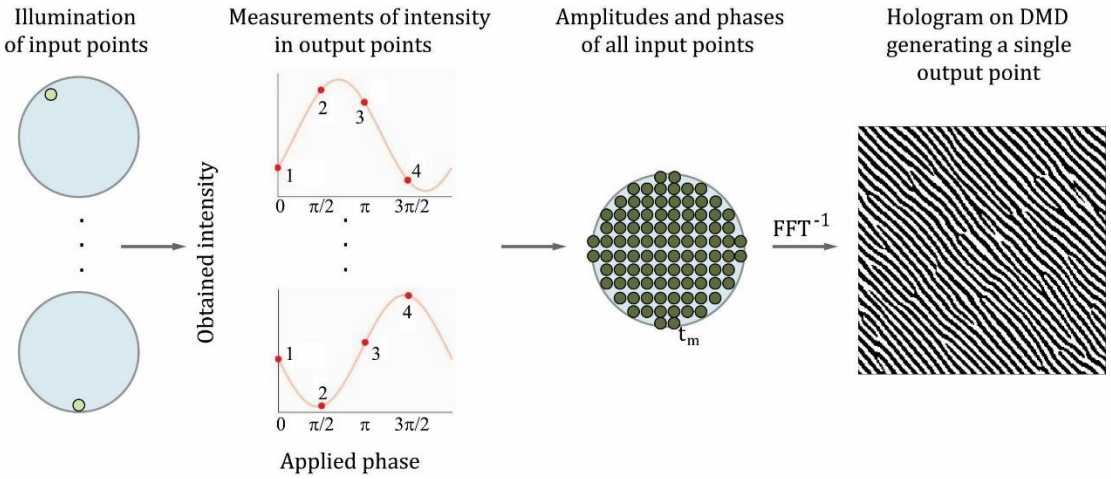

Figure 2.7: Generation of a focal spot at the output of the fibre. For every input point, amplitude and phase shift in the corresponding output point is measured. This input field of complex amplitudes t is inverse Fourier transformed and binarized to obtain the hologram, which is then displayed on the DMD. The wavefront modulated by this hologram forms a focal spot at plane at chosen distance from the output facet.

Using a spatial light modulator combined with the measurement of TM has been successfully used in the scanning configuration in fluorescence imaging [93, 94, 132] and micro-manipulation [93, 132].

Imaging plane and variation of its distances from the fibre facet

The TM measurement can be performed at various distances from the fibre facet. As a result, the focal spot is created at a defined working distance from the output fibre facet. The field of view (FOV) at the distal fibre facet is given by the size of the core. With increasing the working distance, the FOV also increases, however, it is at the cost of the resolution determined by the numerical aperture (NA).

The intensity in the graph of Fig. 2.8 reflects the variation in the NA (in the scale from 0 to 0.22) with the distance from the fibre facet. When imaging further from the facet, the distance in which the resolution is still limited by diffraction depends on the NA in the given location. The maximal NA can be reached only in a cone with a base corresponding to the fibre core and the distance H given as

$$H = \frac{d_{core}}{2\mathrm{NA}}, \tag{2.24}$$

where d_{core} is the diameter of the fiber core [93]. The distance H for the fibre used in our experiments (diameter of 50 μm, NA 0.22) was approximately equal to 114 μm. We typically set the working distance to ∼30 μm which ensured diffraction-limited resolution across most of the FOV. The green lines indicate NA profiles in different transversal planes, while the yellow one shows the maximum NA.

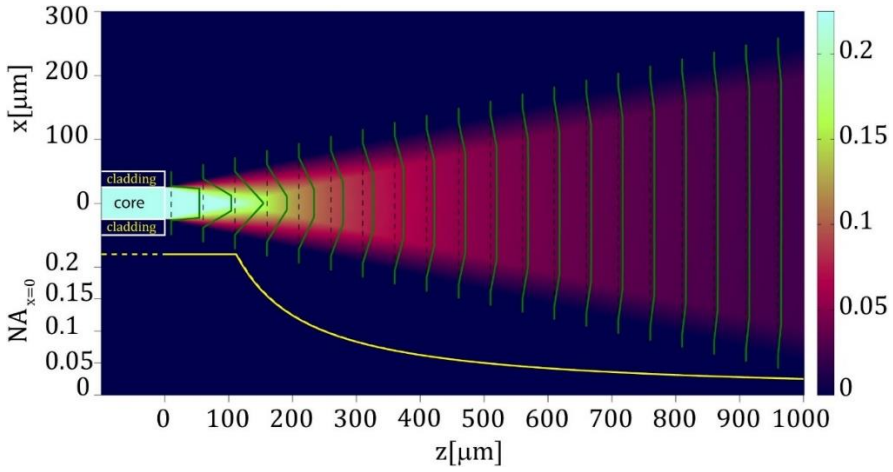

Figure 2.8: Evolution of the numerical aperture at different distances from the fibre facet [93]. The green lines indicate the NA profile in transversal planes and the yellow line show the maximum NA along the optical axis *z*.

2.6 Imaging through the MMF with calibrated foci

After the binary-amplitude holograms are calculated for all output modes, they are projected sequentially, yielding a scanning focal spot in the working distance of the distal fibre facet. The maximum scanning speed is determined by the refresh rate of the DMD, which is 22 kHz. For fibre used in the experiments presented here, this corresponds to 3.5 fps for the full field of view – 50 μm in diameter (see Fig. 2.9).

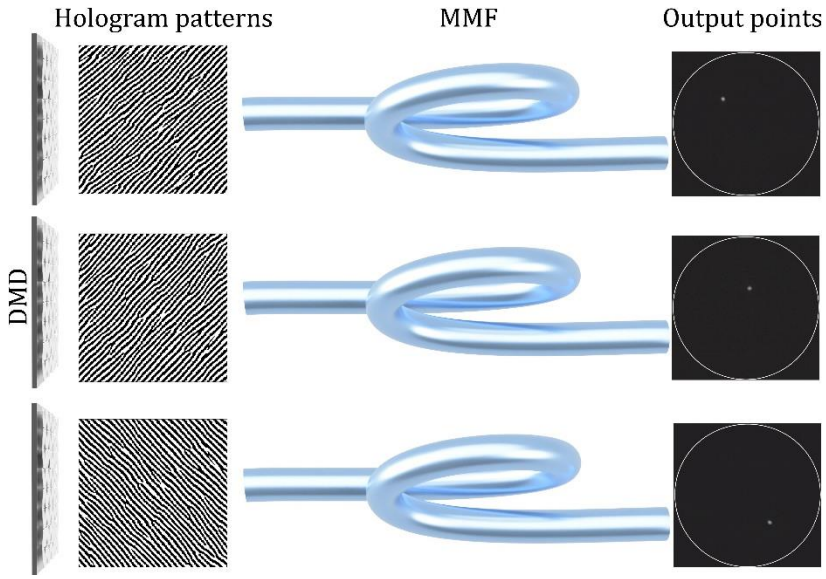

Figure 2.9: Patterns projected on the DMD and the corresponding output focal spots.

In fluorescent imaging, the scanned focal spot excites the fluorescence signal from the sample. Some of the emitted signal couples back into the same MMF, propagates to the proximal end where it is spectrally separated with a filter (F, Fig. 2.5). Since the emitted signal is not very strong, typically a sensitive detector such as photomultiplier tube (PMT) is used. Its acquisition frequency is synchronized with the scanning rate of the DMD.

3. Results

In this chapter I first present the conditions that need to be met for high quality imaging using the holographic endoscope (Section 3.1) and demonstrate imaging of a two-dimensional and three-dimensional fluorescent phantom sample (Sections 3.2 and 3.3). Next, I present a method that allows to enhance the image quality via post-processing (Section 3.4). In Section 3.5 I summarize procedures that we used for the acquisition of brain samples from live mice expressing a suitable fluorescent protein. In Section 3.6. I demonstrate the principle and verification of the effect of confocal endo-microscopy.

3.1 Quality of the scanning spot

The quality of the fluorescence image in holographic micro-endoscopy is strongly affected by the quality of the scanning spot. After calibration using phase-only modulation, the scanning spot carries only a fraction of the optical power compared to the full power delivered by the MMF (Fig. 3.1a). It has the shape of a high-intensity peak surrounded by a series of concentric rings (Fig. 3.1b bottom). The remaining fraction of light is dispersed as a random background pattern (Fig. 3.1a, bottom). This is typically quantified by the "power ratio" (PR) given by the ratio between the power in the spot and the total output power [103]. $PR = 1$ describes an ideal focal spot without any background while $PR = 0$ is essentially random speckles. One of the reasons for PR drop is that the MMF can randomize the polarisation of the propagated light. This implies that both polarizations should be modulated separately. Short segments of MMFs have been shown however to maintain circular polarization quite well [102] which can be exploited in single-polarization control geometries [103]. Another significant drop of PR is caused by modulation of phase rather than the complex modulation of light. DMDs could be theoretically used in the regime of complex modulation but at a cost of significant power losses [128] which for the case of imaging *in vivo* with the laser available to us was not desirable. Therefore, we used the phase-only modulation of light in the off-axis regime as detailed in [121] and the maximum PR achievable was 79% [101].

During fluorescent imaging, the background also excites the sample and therefore falsely contributes to the signal collected by the PMT. This causes a decrease of the contrast and resolution of the image.

The power in the focal spot was calculated as the volume under the peak fitted with the Airy function delimited by the first minimum. Firstly, the output point is imaged with 4 different exposition times and a single image with increased dynamical range is created. This image is created by taking the pixel value from the longest exposure time without the detector saturation and scaling it according to the relative exposure time for every pixel in the image. This image is then fitted for the amplitude, orientation, width in both axes and the centre using an Airy function *z*.

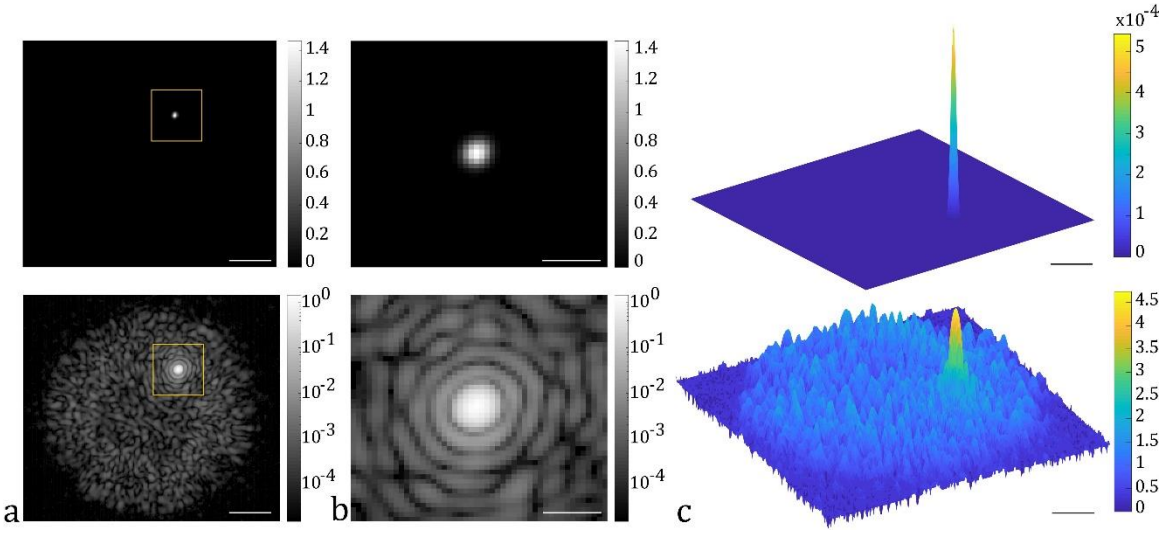

Figure 3.1: Calibrated focal spot. a) Example intensity image of a focal spot generated through the MMF with PR = 75 %. The speckled background is visible from the log-scale image (bottom). Scale bar is 10 μm. b) Zoomed-in images of the focal spot. Scale bar is 2.5 μm. c) 3D visualisation of the focal spot. Scale bar is 10 μm.

The resulting Airy disc is defined by parameters par in *xy={x,y}* coordinates.

```
function z = FitAiry(par, xy)
    %  1 Airy amplitude
    %  2 Airy angle
    %  3 Airy width x
    %  4 Airy width y
    %  5 Airy center x
    %  6 Airy center y

    % Axes for Airy
    xA = xy{1};
    yA = xy{2};
    % Offset
    xAo = xA - par(5);
    yAo = yA - par(6);
    % Rotate
    xAor =  xAo * cosd(par(2)) - yAo * sind(par(2));
    yAor =  xAo * sind(par(2)) + yAo * cosd(par(2));
    % Scale
    xAors = xAor ./ par(3);
    yAors = yAor ./ par(4);
    % Radial coordinate
    rA = sqrt(xAors.^2 + yAors.^2);
    % Empty array with ones
    zA = ones(size(rA));
    % Select points that are not too close to zero
    rAn = abs(rA) >= 0.05;
    % Airy function
    zA(rAn) = sqrt(par(1)) .* (2 * besselj(1, rA(rAn)) ./ rA(rAn));
    % Intensity
    zA = abs(zA).^2;

    % Result
    z = zA;
end .
```

For high imaging quality, we strive to achieve high PR with good stability in the range of hours. The stability of PR is affected by the stability of the setup and the environment in the laboratory. The main factors are the changes in the temperature. The unstable environment temperature cause mainly changes of light polarization within single-mode fibres (SMF). It is necessary, therefore, to filter and stabilise the polarization using a polarizer plate located at the output of the SMF, before the light beam reaches the surface of the DMD and reflects into the MMF. Another component highly dependent on temperature is the DMD chip. During the calibration, the DMD chip is heating by high-frequency switching of the mirrors. In its inactive state the DMD starts to cool down. During the imaging, the fast scanning and the fast display frame rate continue to cause the increase of temperature of the DMD. This heating causes the deformation of the DMD chip (its micro-mirrors) leading to wavefront deviations. This results in a change of the input points phases of the modulated wavefront, which are different from the originally measured phase-shifts [133]. This results in a visible degradation of the PR during time causing decrease of the contrast and resolution of the scanned images. In order to stabilize the PR, we mounted a thermoelectric cooler (TEC) with a Peltier and a heat sink at the back of the DMD module. The temperature of the TEC is set to 32°C, which is in between the scanning and the resting regime of the DMD. The TEC cools the DMD while scanning and heats it slightly when at rest stabilizing the temperature in the range of $\pm$0.2°C [133]. After these modifications, satisfactory long-term stability of the PR has been achieved. During the 50-hours measurement, the PR dropped only by 5% (Fig. 3.2), which is satisfactory for *in vivo* imaging.

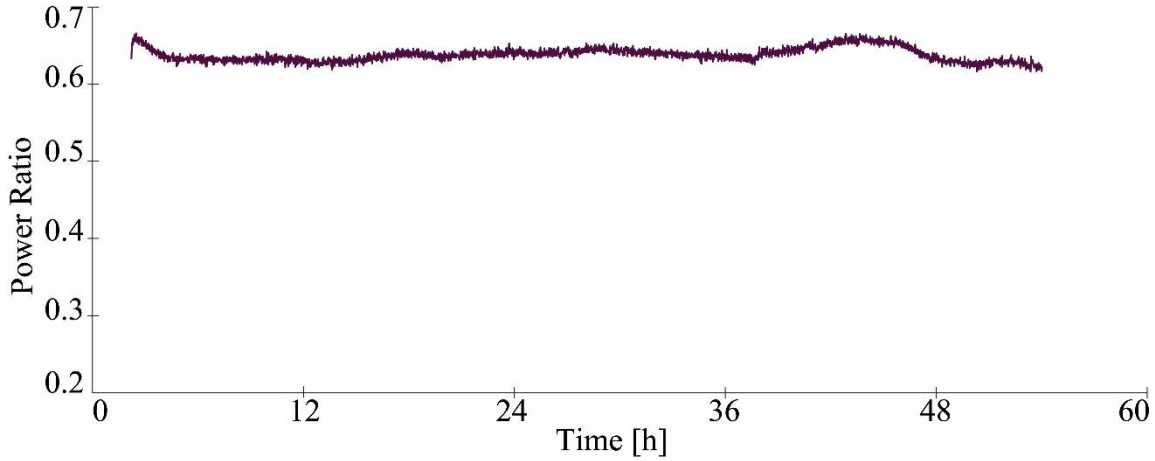

Figure 3.2: Performance of the stabilised setup. The PR dropped only by ~5% in 50 hours.

3.2 Fluorescence imaging of a two-dimensional phantom sample

We tested the imaging performance with fluorescent microspheres with a diameter of 2 μm (FluoSpheres™ Carboxylate-Modified Microspheres, 2.0 μm, Nile Red fluorescent (535/575), 2% solids, ThermoFisher Scientific) dispersed in distilled water in a ratio of 1:1000. The microspheres suspension was applied on a 0.17 mm thick cover glass and left to dry. The optical fibre was calibrated at a working distance of ~25-35 μm. The focal

spots were scanned across the whole field of view (dia ~50 μm) with a speed of 3.5 fps (Fig. 3.3).

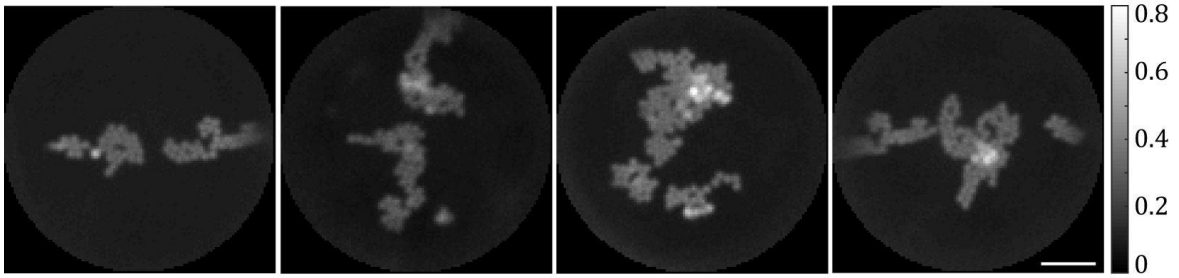

Figure 3.3: Example FOV of fluorescent microspheres on a cover glass. Scale bar is 10 μm.

3.3 Fluorescence imaging of a volume phantom sample

The ability of refocusing within a sample is crucial for any type of biological imaging. Using the MMF-based endoscope, the refocusing can be done by moving the probe inside the tissue. However, it is not convenient for short-distance refocusing in which the moving probe deforms the tissue [138]. As described previously it is possible to calibrate the scanning spot at various distances from the fibre facet, although the further we calibrate, the smaller the area in the FOV within which the resolution is still diffraction-limited (see Fig. 2.8 in Section 2.5). We calibrated 4 planes in the range of 30 μm, 10 μm apart from each other. The calibration for different working distances was done sequentially for each plane by measuring the corresponding TM and calculating the set of holograms.

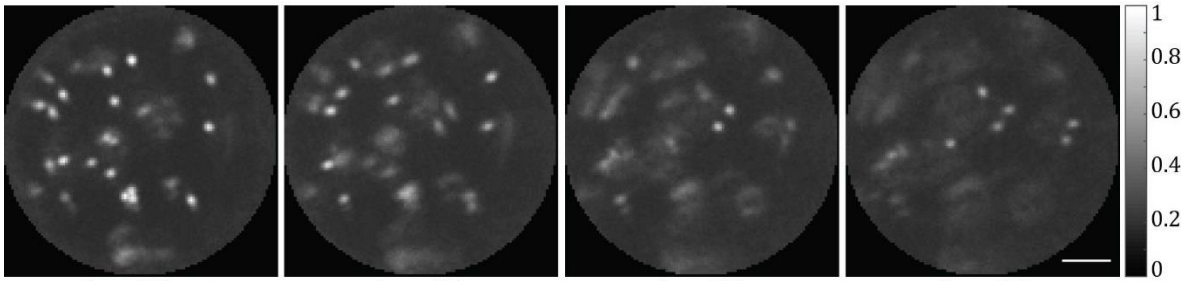

Figure 3.4: Imaging of a 3D phantom sample of fluorescent microspheres dispersed in an agarose gel. The sample was refocused by 10 μm in 3 steps. Calibration was performed at working distances (wd) 35, 45, 55 and 65 μm from the fibre facet. Scale bar is 10 μm.

A 3D fluorescent sample was prepared by dispersion of fluorescent microspheres (FluoSpheres™ Carboxylate-Modified Microspheres, 2.0 μm, Nile Red fluorescent (535/575), 2% solids, ThermoFisher Scientific) in 0.5% agarose gel. A 3 mm-thick layer was applied to a cover glass. After calibration, the MMF was inserted into the sample, and refocusing to different depths was done by loading the appropriate set of holograms (Fig. 3.4).

Refocusing without physical movement of the probe can be used with advantage in imaging *in vivo*, where the minimization of tissue displacement and damage is of high importance.

3.4 Computational Image Enhancement - harnessing the *muddy modes*

As discussed in Section 3.1, the maximum PR for phase-only modulation is 79%. The speckled background falsely contributes to the signal and decreases the dynamic range of the images. This effect is very significant in brain tissue where thin neuronal processes surround very bright cell bodies.

The focal spot, including the speckled background can be thought of as an impulse response function of the endoscope, similarly to the point spread function of a classical microscope. Knowing the shape of the PSF, the images can be reconstructed with higher resolution and contrast using deconvolution. In the case of endoscopic imaging, the PSF has a shape of the focal spot with speckled background which is unique for every position of the focus. We call these structures the *muddy modes*. Provided a good stability of the setup, the muddy modes are reproducible. Therefore, we proposed a similar approach to the deconvolution using records of all muddy modes used for imaging.

A single intensity measurement r_i in the *i*-th pixel recorded by the PMT can be expressed as the sum of the illumination intensity across all pixels (one muddy mode) weighted by the density of fluorophores in the sample **s**. The illumination patterns including the focal spot and background measured with the camera, are stored in a muddy-mode matrix **M**, where each row contains one muddy mode flattened into a vector. The sample **s** is arranged into a column vector hence **r** can be written in the form of a forward problem as a linear transformation

$$\mathbf{r} = \mathbf{M}\mathbf{s}. \tag{3.1}$$

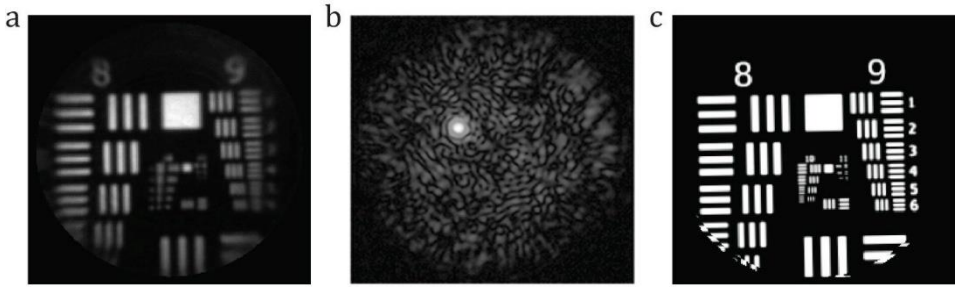

Figure 3.5: The detected image r (a), captured image of the n^{th} muddy mode M_n (b) and the sample **s** - fluorescent USAF target.

If we measure both **r** and **M** in Eq. (3.1), we can calculate the sample **s**. One could find the solution for **s** using a direct matrix inversion. However, due to the presence of noise in both **r** and **M**, the resulting image would be of poor quality. Therefore, we proposed two approaches for retrieving the sample taking into account the noise. One approach is based on a regularised iterative inversion algorithm, respecting the Poisson noise distribution (PN) in the measured signal. The second exploits a simple regularised direct pseudo-inversion algorithm originally designed for an intensity invariant noise (INN). The algorithms manipulate the contrast of different spatial frequencies and can therefore be used to optimize the contrast and resolution of the image.

Reconstruction algorithm for images with a Poisson noise (PN)

An eligible reconstruction algorithm can be the one operating with the statistical distribution of the noise. In the case of imaging through the MMF a Poisson noise distribution in the recorded signal **r** can be expected due to the nature of a photon-detection process [135]. We confirmed this by measuring the variance of the recorded signal (Fig. 3.6).

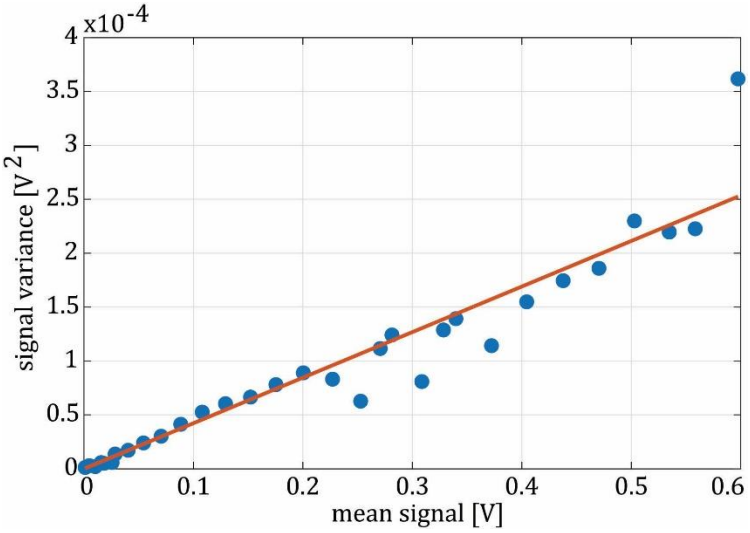

Figure 3.6: Variance of the recorded voltage from the PMT as a function of its mean (blue dots) and the linear interpolation (red).

The distribution of the real sample **s** (the most probable values of **s** solving Eq. (3.1)) can be found using the maximum likelihood estimation. To find the inverse solution of Eq. (3.1), one can use an iterative scheme [see Eq. (21) in 135] (assuming zero background)

$$\mathbf{s}^{(\mathrm{i}+1)} = \frac{\mathbf{s}^{(\mathrm{i})}}{1 + \lambda \nabla \mathcal{R}(\mathbf{s}^{(\mathrm{i})})} \left[\mathbf{M}^T \frac{\mathbf{r}}{\mathbf{M}\mathbf{s}^{(\mathrm{i})}} \right], \tag{3.2}$$

where $s^{(i)}$ and $s^{(i+1)}$ are the sought solutions in the i^{th} and $(i+1)^{\text{th}}$ iteration steps, respectively. $\lambda \nabla \mathcal{R}(\mathrm{s}^{(\mathrm{i})})$ is a regularisation term, $\mathcal{R}(\mathrm{s})$ is a regularisation function, $\lambda \geq 0$ is a regularisation factor determining the strength of the applied regularisation and ∇ is the operator of function gradient. One of the simplest regularisation functions is known as an L_2-norm giving a preference to solutions with smaller norms defined as

$$\mathcal{R}(\mathrm{s}) = \frac{1}{2} \|\mathrm{s}\|_2^2. \tag{3.3}$$

The solution of inverse problems with this type of regularisation is often referred to as the Tikhonov, or ridge regularisation [136] and we can simply express the gradient of the regulariser taking part in Eq. (3.3), i.e. $\nabla \mathcal{R}(\mathrm{s}) = \mathrm{s}$. For the initial guess $s^{(0)}$ assuming it is non-negative, the solution of Eq. (3.2) will be non-negative as well [135] and the solution **s** will meet physical reality.

Reconstruction algorithm for images with an intensity independent noise (IIN)

In the second approach we use the algorithm which presumes an intensity independent noise distribution in the recorded signal **r**. This assumption is not correct in general for an imaging process; however, it allows to search for the solution of Eq. (3.1) by minimization of a least-squares problem

$$\Psi = \sum_{i=1\ldots n_{\mathrm{r}}} [(\mathbf{M}\mathbf{s})_i - r_i]^2 + \lambda \mathcal{R}(\mathbf{s}) \tag{3.4}$$

where $\lambda\mathcal{R}(\mathbf{s})$ represents the regularisation term and λ is a regularisation factor. In an absence of any regularisation, Eq. (3.4) could be solved using pseudo-invers of **M**. This can be computed with a singular value decomposition (SVD) and **M** can be thus written as:

$$\mathbf{M} = \mathbf{U}\Sigma\mathbf{V}^T, \tag{3.5}$$

where **U** and **V** are orthogonal matrices and Σ is a rectangular matrix of singular values σ_i in diagonal. The pseudo-inverse matrix $\mathbf{M}^+$ can be expressed as

$$\mathbf{M}^+ = \mathbf{V}\Sigma^+\mathbf{U}^T \tag{3.6}$$

The matrix Σ^+ is the pseudo-inverse of Σ, where each diagonal element is replaced by its reciprocal value. With the regularisation term present in Eq. (3.4), its minimum can also be found using the SVD. The solution can be found by adjusting the diagonal values of Σ^+ in a sense

$$\Sigma_{ii}^{+\prime} = \frac{\sigma_i}{\sigma_i^2 + \lambda^2}. \tag{3.7}$$

All non-diagonal values remain zero. The regularised pseudo-inverse can then be expressed as

$$\mathbf{M}^{+\prime} = \mathbf{V}\Sigma^{+\prime}\mathbf{U}^T \tag{3.8}$$

and an efficient estimate of the sample can be obtained from

$$\mathbf{s} = \mathbf{M}^{+\prime}\mathbf{r}. \tag{3.9}$$

The pseudo-inversion for a single regularisation strength λ has to be performed only once and the solution of the inverse problem constitutes a simple and fast matrix-vector multiplication. The sample estimate **s** is on the other hand no longer guaranteed to be non-negative. A significant part of the sample estimate may yield negative values, depending on the strength of the regulariser. This does not correspond to an ideal photon detection process. In reality, some negative values may still occur in the image as a result of e.g. the detector dark noise (Fig. 3.7). A solution with a small fraction of negative values may be acceptable.

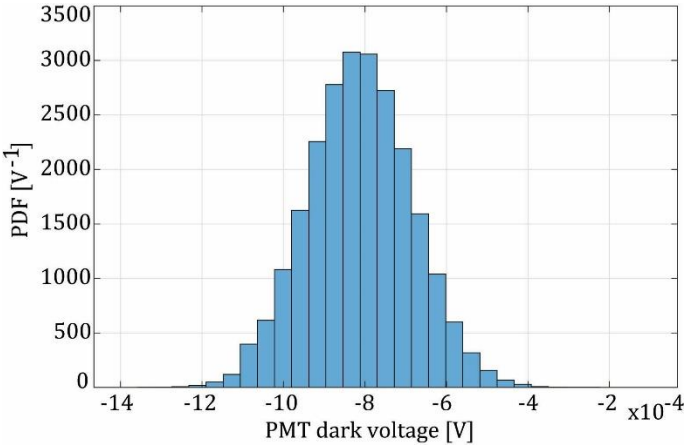

Figure 3.7: The probability density function (PDF) of PMT dark noise.

Experimental setup and sample preparation

For the experimental measurement, we have used our optical setup (Fig. 2.5) whose simplified geometry is presented in Fig. 3.8 outlining all steps of the procedure. The calibration part was done as described previously (Section 2.5). The calculated holograms are displayed on the DMD, and the muddy modes are raster-scanned across the imaging plane at the working distance from the fibre output facet.

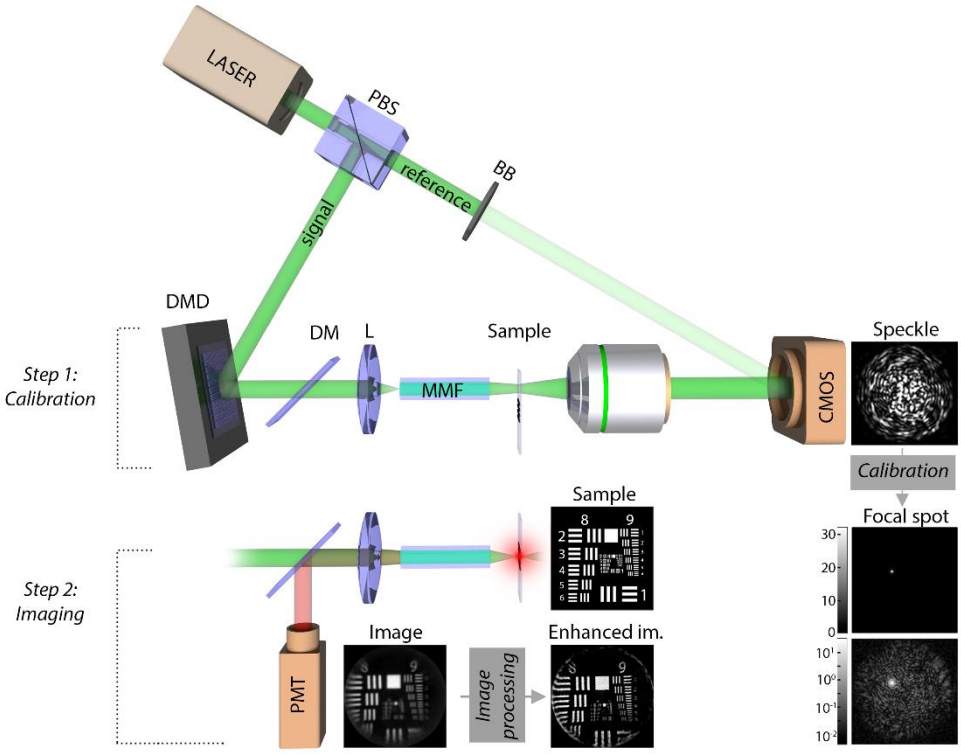

Figure 3.8: Simplified endoscope setup and the flow of calibration, imaging, and image enhancement procedures. After calibration, the intensity of the focal spot with background signal - muddy mode, is measured. A fluorescent signal from the sample (USAF target) is detected on a PMT and the resulting image is post-processed by the reconstruction algorithms. The result is an enhanced image with higher contrast and resolution.

The intensity distribution of every muddy mode is recorded on the camera and saved for the purpose of computational image enhancement.

Due to the insufficient dynamic range of the CMOS camera, we needed to implement an image capturing technique of a high-dynamic range (HDR) via multiple camera exposures. Every muddy mode was recorded with three different camera exposure times - 10, 100 and 1000 μs. The resulting image of a muddy mode was formed by taking the pixel value from the longest exposure time without the detector saturation and scaling it according to the relative exposure time for every pixel in the image. For the experiment, we measured 34 894 muddy modes with foci organized across a rectangular grid with a period of 225 nm. For the image acquisition, the fluorescent sample was inserted under the MMF into its focal plane and scanned across the whole FOV corresponding to ~50 μm with a refresh rate of the DMD of ~0.5 full scans fps.

Our sample was a fluorescent USAF target (Fig. 3.9a) which allowed us to directly measure contrast of distinct spatial frequencies directly related to image resolution. The sample (Fig. 3.9b) was prepared from a fluorescent layer of Rhodamine B with spacers of 5 μm in diameter in between a cover glass and an in-house made USAF target deposited on a cover glass.

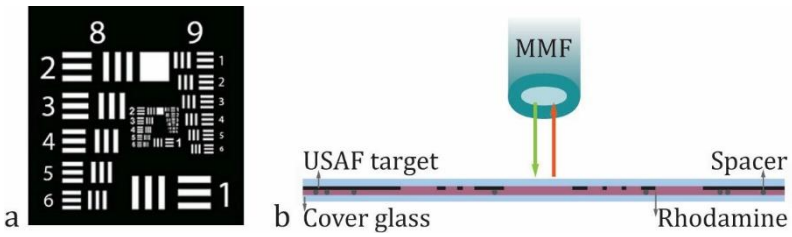

Figure 3.9: A fluorescent USAF target sample. a) An USAF target with groups 8 and 9 selected for deposition to serve as the fluorescent sample. b) The structure of the fluorescent USAF target deposited on a cover glass with a layer of Rhodamine and spherical spacers enclosed by a second cover glass.

The dependence of image contrast on spatial frequencies can be described by a contrast transfer function (CTF). We directly measured the contrast from regions of interest indicated in Fig. 3.10a. The selected elements 2-4 from group 8 and elements 1-6 from group 9 have theoretical spatial frequencies $f_{8,2} = 287.4\,mm^{-1}$, $f_{8,3} = 322.5\,mm^{-1}$, $f_{8,4} = 362.0\ mm^{-1}$ and $f_{9,1} = 512.0\,mm^{-1}$, $f_{9,2} = 574.7\,mm^{-1}$, $f_{9,3} = 645.1\,mm^{-1}$, $f_{9,4} = 724.1\,mm^{-1}$, $f_{9,5} = 812.7\,mm^{-1}$and $f_{9,6} = 912.3\,mm^{-1}$, respectively. Figure 3.10b shows the CTF measured from the image (red points) and a theoretical CTF corresponding to an aberration-free imaging system with a circular aperture and numerical aperture NA = 0.22, i.e. NA of the MMF fibre used for imaging (blue).

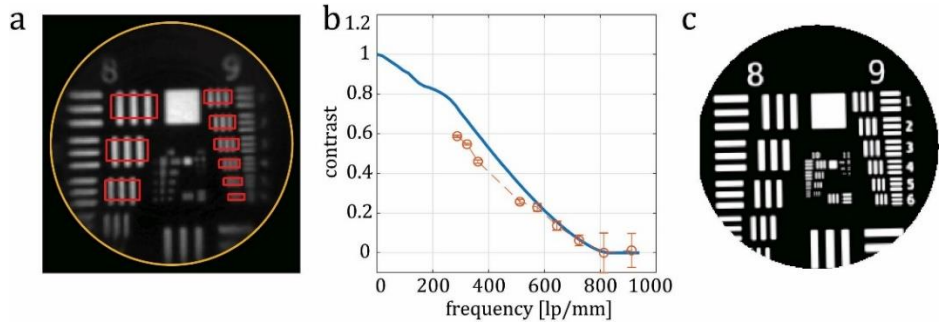

Figure 3.10: USAF target imaged by point scanning. a) Experimentally obtained image of the USAF target with regions of interest used for computation of the contrast (red) and with an area corresponding to the FOV of the MMF (yellow). b) CTF calculated from the indicated regions in (a) (red) and a theoretical CTF (blue), error bars represent the 95% confidence intervals. c) "ground truth" image.

Criteria for evaluation of image quality

To determine the quality of the reconstructed image, we compare it to a "ground truth" image of the USAF target (Fig. 3.10c) obtained by scanning electron microscopy, binarized, scaled down to the desired pixel resolution and registered to the reconstructed image.

One of the common measures is the peak signal-to-noise ratio (PSNR) [137] defined as

$$\mathrm{PSNR} = 10\log_{10}\left[\frac{1}{\mathrm{MSE}}\right], \tag{3.10}$$

where

$$\mathrm{MSE} = \frac{1}{n_s}\sum_{i=1\ldots n_s}[\beta\mathbf{s}_i - \mathbf{t}_i]^2. \tag{3.11}$$

MSE represents the mean squared error, n_s is number of pixels forming the reconstructed sample **s**, $\boldsymbol{s_i}$ and $\boldsymbol{t}_i$ represent the intensity of *i*-th pixel of the recorded or reconstructed image and "ground truth", respectively. The dynamic range of the reconstructed image however may change because the intensity scale corresponding to the photon count is not conserved in the regularised reconstruction process. Thus, we introduce a scaling factor β, which allows to maximize the PSNR for each regularised strength and thus compare the corresponding PSNR values.

Another approach taking into account the human perception is the Structural Similarity Index (SSIM) [138]. The method assesses the visual impact of luminance, contrast and structure of the image and can be described as

$$\mathrm{SSIM} = \frac{(2\mu_s\mu_t + c_1)(2\sigma_{st} + c_2)}{(\mu_s^2 + \mu_t^2 + c_1)(\sigma_s^2\sigma_t^2 + c_2)}, \tag{3.12}$$

where μ_s and μ_t are the means, σ_s and σ_t are the standard deviations, σ_{st} is the cross-covariance for images **s** and **t**, respectively, and c_1 and c_2 are small constants used to prevent zero division. The SSIM demonstrates how the human eye perceives

a difference between 2 images in a range of 0-1, where 0 is for images with no similarity and 1 is for identical images.

Image enhancement with Poisson noise (PN)

Firstly, the enhanced images from experimentally obtained data are calculated for various values of the regularisation factor λ using Eq. (3.2). The initial guess of solution $s^{(0)}$ is selected as uniform over the field with intensity corresponding to mean value of the original image, although other choices of $s^{(0)}$ may in principle guarantee faster convergence. The number of iterations is limited by a relative change of intensity between consequent iterations of maximum 1% or a total of 50 iterations.

The set of reconstructed images for selected λ and the original image are presented in Fig. 3.11a. The corresponding CTFs are plotted in Fig. 3.11b, where a maximum contrast of 1 is delineated by dashed black line in graphs.

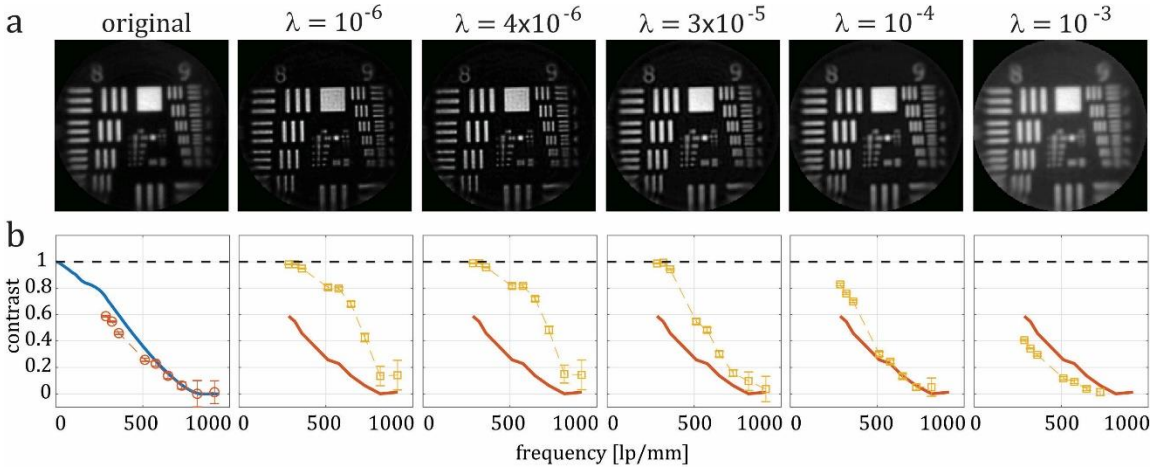

Figure 3.11: The effect of λ on reconstructed images using the PN-based inversion. a) Image of the USAF target obtained by scanning the fluorescent sample via the MMF (original) and image reconstructions for different values of λ. b) Corresponding CTFs: theoretical (blue), CTF calculated from the original image (red) and from the reconstructed images (yellow), respectively. Error bars represent the 95% confidence intervals.

For the original image the blue curve represents the theoretical CTF and the red curve has been calculated from the acquired image. It is displayed in all graphs for the comparison to the CTFs calculated from the reconstructed images (yellow). The image can be therefore enhanced within the region outlined by the dashed line and the red curve.

The graphs show the increase of contrast for the evaluated spatial frequencies. The contrast of all analysed spatial frequencies in our sample can be enhanced and it can be determined, which value of λ is the most effective. The evolution of contrast of different spatial frequencies with λ is presented in Fig. 3.12. The values of the contrast calculated from the original image are dash-dotted in the same colour code. For frequencies ≤ 323 lp/mm (line pairs per millimetre), the contrast can be enhanced up to ~ 0.99 for $\lambda < 5 \times 10^{-5}$. The grey area highlights a common range of $\lambda < 6 \times 10^{-5}$ for which the contrast has been enhanced for all spatial frequencies. The contrast curves plateau for λ in the range of

$1.5 \times 10^{-6} \leq \lambda \leq 5 \times 10^{-6}$, which corresponds to enhancement by 68% (for the lowest frequency) and more.

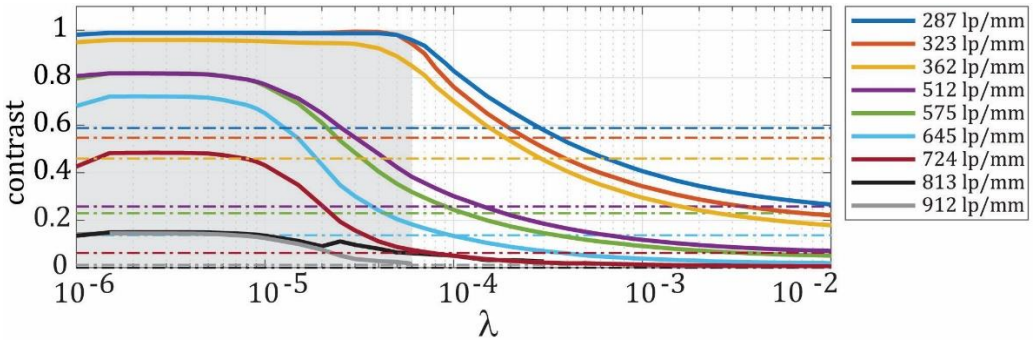

Figure 3.12: Mean contrast across resolved USAF target elements as a function of λ. Each colour represents a different spatial frequency, the dash-dotted horizontal lines show the contrast of the corresponding spatial frequency in the original image. The grey area indicates the region in which the contrast has been enhanced for all evaluated spatial frequencies.

Figure 3.13 depicts peak signal to noise ratio - PSNR (blue) and structural similarity index - SSIM (red) as a function of λ. The corresponding values from original image are represented by dashed lines with values of 11.36 dB and 0.31, respectively. According to PSNR metric, the reconstructed images are enhanced for $\lambda < 5 \times 10^{-4}$ reaching maximum of 12.91 dB. This corresponds to an enhancement by ~14%. According to the SSIM metric the images are enhanced in the same interval of λ with maximum reaching 0.4, which corresponds to an enhancement of 29%. Both metrics reach their maximal values close to $\lambda \sim 3 \times 10^{-5}$.

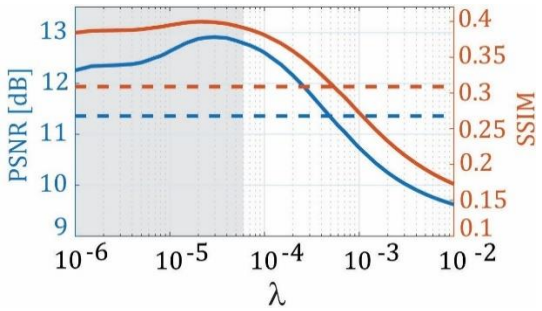

Figure 3.13: PSNR and SSIM of the reconstructed images as a function of λ. Dashed lines represent the PSNR and SSIM of the original image, 11.36 dB and 0.31, respectively. The grey region highlights the range of λ with enhanced contrast for all spatial frequencies.

These results imply that the optimal choice of the regularisation factor is a value in the range $5 \times 10^{-6} \leq \lambda \leq 3 \times 10^{-5}$, leading to enhancement of all three metrics. A single value used from this range will fine-tune the enhancement towards either contrast or PSNR and SSIM, respectively.

Image enhancement with the IIN

The image reconstructions for the case of intensity-independent-noise (IIN) - based inverse modelling, were calculated using Eqs. 3.8 and 3.9. Figure 3.14a shows the original image and sample reconstructions for different values of λ. Small values of λ result in an

increased level of noise (for $\lambda = 0.01$). This can be expected when considering the limiting case of $\lambda = 0$, for which the transformation is basically not regularized. The inversion mapping of **r** to **s** operates in a non-regularized problem essentially as a high-pass filter, which amplifies the smaller singular vectors of **M**, i.e. the noise.

The values of $\lambda < 0.22$ give reconstructions with negative values which fraction strongly increases with decreasing of λ. The threshold for negative pixels was set to 1% of the total pixel count, which is fulfilled for $\lambda \geq 0.16$. For the high values of λ the transformation operates as a low-pass filter slightly decreasing the contrast of low frequencies and suppressing the contrast of high ones. As a result, we receive a smoothed image with the resolution lower than the original, which can be seen in Fig. 3.14 for $\lambda = 5$.

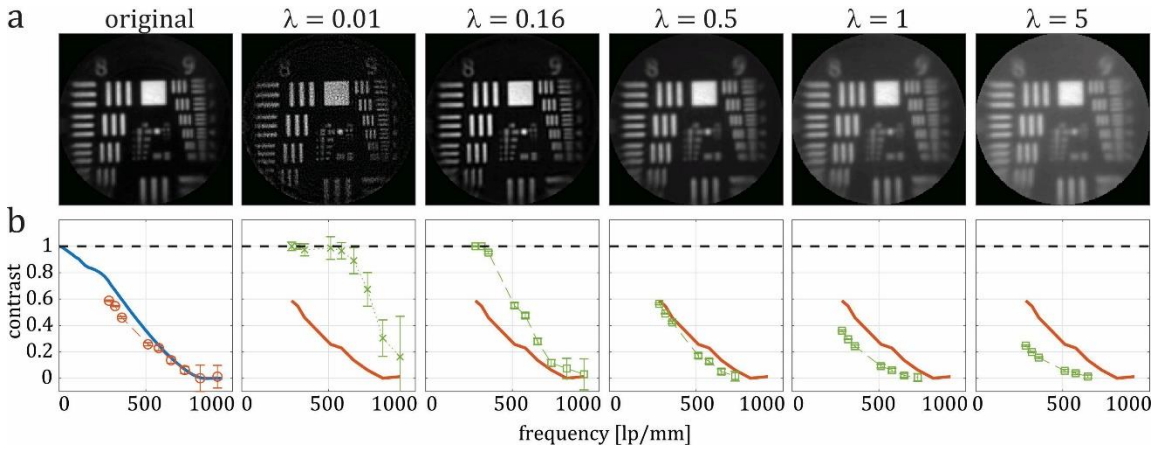

Figure 3.14: The effect of λ on reconstructed images using the inversion with IIN. a) Image of the USAF target obtained by scanning the fluorescent sample via the MMF (original) and image reconstructions for different values of λ. b) Corresponding CTFs: theoretical (blue), CTF calculated from the original image (red) and from the reconstructed images (green), respectively. Error bars represent the 95% confidence intervals.

The CTFs corresponding to the images in panel (a) are plotted in Fig. 3.14b. The maximum contrast of 1 is represented as a dashed line. Negative values in reconstructions with $\lambda < 0.16$ were replaced by zeros, therefore the calculated contrast is not artificially increased.

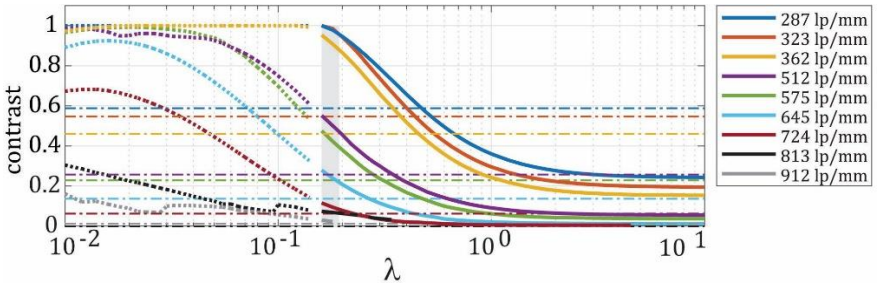

Figure 3.15: Mean contrast across the resolved USAF target elements as a function of λ. The grey area indicates the interval of acceptable solutions for which the contrast of all evaluated spatial frequencies has been enhanced. The dotted segments indicate unacceptable solutions.

The quality of enhancement is evaluated by the average contrast enhancement for each resolved spatial frequency as a function of λ shown in graph in Fig. 3.15. Again,

the reference values calculated from the original image are plotted as dash-dotted lines in the same colour code.

For frequencies $\leq 323\ \mathrm{lp/mm}$ the contrast can be enhanced up to 1 using regularisation factor $\lambda = 0.16$. The gray area highlights a range of $0.16 \leq \lambda \leq 0.18$, for which the contrast has been enhanced for all spatial frequencies. In this case, the range of λ is very narrow. Selecting higher λ (up to 0.47) will result in an increase of contrast of the lower spatial frequencies but decrease of the higher ones. The contrast curves peak for $\lambda \leq 0.016$, which is among the unacceptable solutions plotted in dotted curves. The maximum acceptable contrast enhancement is therefore for $\lambda = 0.16$, which corresponds to enhancement by 69% (for the lowest frequency) and more (for higher frequencies).

The graph in Fig. 3.16 shows the PSNR (blue curve) and SSIM (red curve) comparison of the enhanced images and their values from original images in dashed lines. The original values are 11.36 dB for PSNR and 0.31 for SSIM. The PSNR metric is enhanced in a range of $0.16 \leq \lambda \leq 0.55$, where the maximum of 12.55 dB is for $\lambda = 0.16$. This corresponds to enhancement by 10 %. The SSIM metric is enhanced over a range of $0.16 \leq \lambda_R \leq 0.6$ with maximal value of 0.39 for $\lambda = 0.16$ as well. This corresponds to an increase of ~26 % compared to original value.

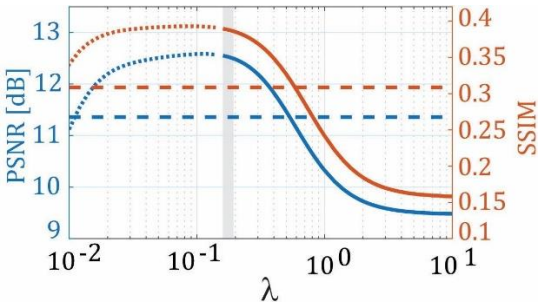

Figure 3.16: PSNR and SSIM of the reconstructed images as a function of λ. The dotted part of the curves indicates unacceptable solutions. The grey region indicates the interval of λ with enhanced contrast for all spatial frequencies as in Figure 3.15.

In order to test and confirm the concept in conditions similar to the biologically relevant imaging we have imaged fluorescent micro-particles on a cover glass. The sample was prepared by dispersing the fluorescent microspheres (FluoSpheres™ Carboxylate-Modified Microspheres, 2.0 μm, Nile Red fluorescent (535/575), 2% solids, ThermoFisher Scientific) in a distilled water (1:1000) and let to dry on a cover glass. The mean value of PR during measurement across the FOV was 0.37 (standard deviation 0.07). Compared to imaging of the USAF target this value was significantly lower. It resulted in lower contrast and resolution of the original image (Fig. 3.17a). Nevertheless, both algorithms succeed to enhance the contrast, reduce the background and increase the resolution, even with sub-optimal conditions. Figure 3.17b compares the intensity profiles along fluorescent microspheres in the original image (red lines 1 and 2) and the reconstructed images using the PN-based algorithm with selected value of $\lambda = 5 \times 10^{-6}$ and the IIN-based

reconstruction with $\lambda = 0.16$. Both methods yield an increased contrast, the PN-based algorithm slightly outperforming the IIN-based one.

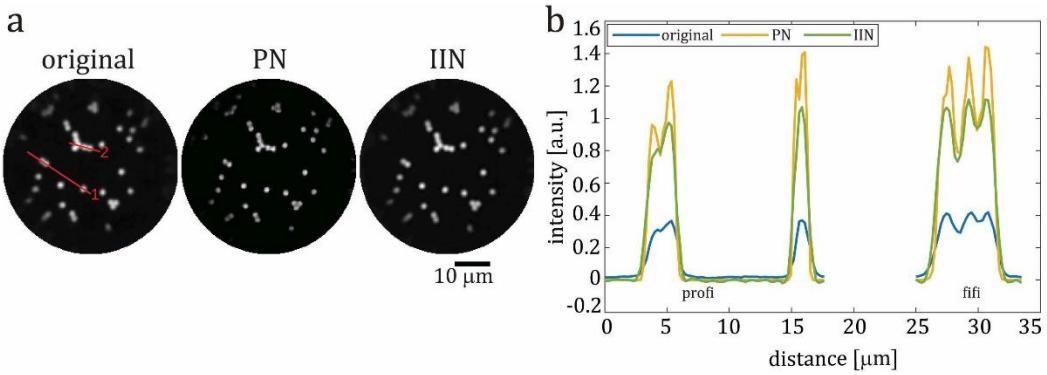

Figure 3.17: Image enhancement of fluorescent micro-particles. a) normalized images of scanned fluorescent microspheres (original) and its reconstruction based on the PN and IIN method. b) Comparison of intensities in profile 1 and 2 (red, original image).

The same optimal value of regularisation factor λ derived from a single image can be used for image enhancement of a series of images of a changing FOV from the sample (PN and IIN in Fig. 3.18 and PN and IIN in Visualization1).

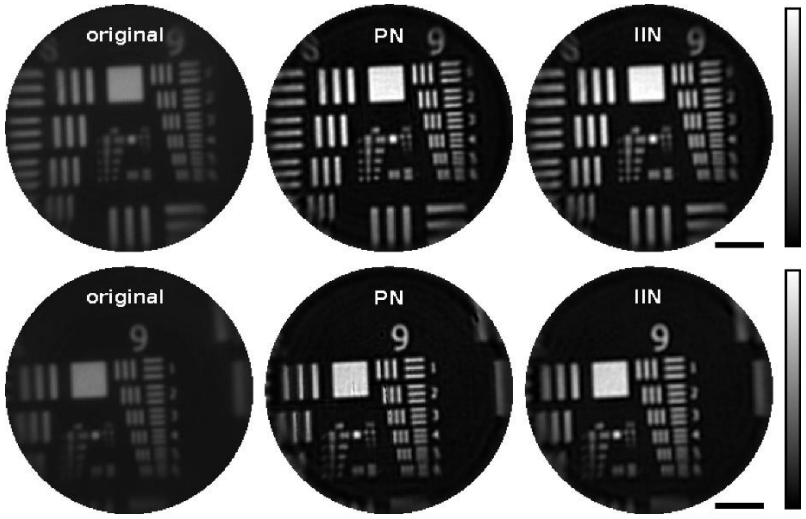

Figure 3.18: Example of 2 field of views from fluorescent imaging of USAF target. For the image enhancement the same optimal values of λ were selected as in Fig. 3.17. Scale bar is 10 µm.

3.5 Imaging of mouse brain tissue

In order to advance the application of MMF-based endoscope to *in vitro* and *in vivo* imaging, it was important to identify a suitable mouse model and master the technique for preparation of the animal brain for the experiment.

3.5.1 Mouse model with sparse fluorescence expression

When imaging through MMF, the sample is illuminated with a PSF, its speckled background and also a conical shape along the *z*-axis. During volumetric imaging this leads to excitation of the fluorescent signal from the selected object but also from the surrounding tissue. For the sample with high density of fluorescent sources yields images with poor contrast and sub-optimal resolution. Decreasing of density of the fluorescent sources alleviates partially these issues. Therefore, it is important to be able modulate sparsity of fluorescent object and create a suitable sample. This is essential especially when imaging thin neuronal structures neuronal processes. The modulation of the density can be done by injection of adeno-associated viral vectors engineering to express a fluorescent protein. The labelling with viral vectors enables to target individual specific cell types in a region of interest. The injection can be tailored by adjusting the injected volume, rate of injection, age of the animal and the location.

Another way for sparsity modulation is genetic engineering. By cross-breeding of the genetically modified mouse lines the required cell types can express the fluorescein protein and also their amount can be controlled in some lines. For our experiments, we have used this cross-breeding method to obtain an animal with the desired sparsity of fluorescence expression in a specific cell type.

Selection of mouse models for cross-breeding

For the *in vitro* and potentially *in vivo* imaging of neuronal networks we identified a genetically modified mouse model with a red fluorescent protein tdTomato conditionally expressed in excitatory neurons under the CAG promotor. This mouse line was obtained by breeding a transgenic line B6.Cg-*Gt(ROSA)26Sor*$^{tm14(CAG-tdTomato)Hze}$/J (007914, Jackson Laboratory, USA) crossed with a Cre-recombinase- expressing mouse line B6;129S6-Tg(Camk2a-cre/ERT2)1Aibs/J (012362, Jackson Laboratory, USA). The excitatory neurons are mostly present in cerebral cortex and also in hippocampus [139, 140, 141].
Figure 3.19 shows schematically the breeding process. The first mouse line has a fluorescent protein tdTomato coded behind a promotor of the gene (R26) which is ubiquitously expressed in every cell in the mouse body. In front of this fluorescent protein is a STOP sequence. The second mouse line has a Cre-recombinase coded behind the promotor which is specific for a selected population of cells (Camk2a for excitatory neurons). The Cre-recombinase cuts out the stop sequence in cells defined by the specific promoter which leads to expression of the fluorescence protein in these cells. The selected Cre line additionally has a Hitshot protein 90 (HSP90) bound to an estrogen receptor ERT (Fig. 3.19c). This protein inhibits the Cre-recombinase Tamoxifen is a nonsteroid anti-estrogen that binds to cytosolic or nuclear estrogen receptor at the same place as

the HSP90. After injection of Tamoxifen, in the cytoplasm it cuts out the HSP90 and bounds to the ERT. The Cre-recombinase is activated, penetrates into the nucleus of the cell and cuts out the stop sequence (Fig. 3.19d).

Depending on the volume and number of doses of injected Tamoxifen, it is possible to regulate the density of the fluorescence protein expression. By injecting higher amount of the Tamoxifen, more excitation neurons will express the tdTomato protein. It is important to titrate the volume of Tamoxifen leading to a suitable density of the fluorescent protein for a particular application.

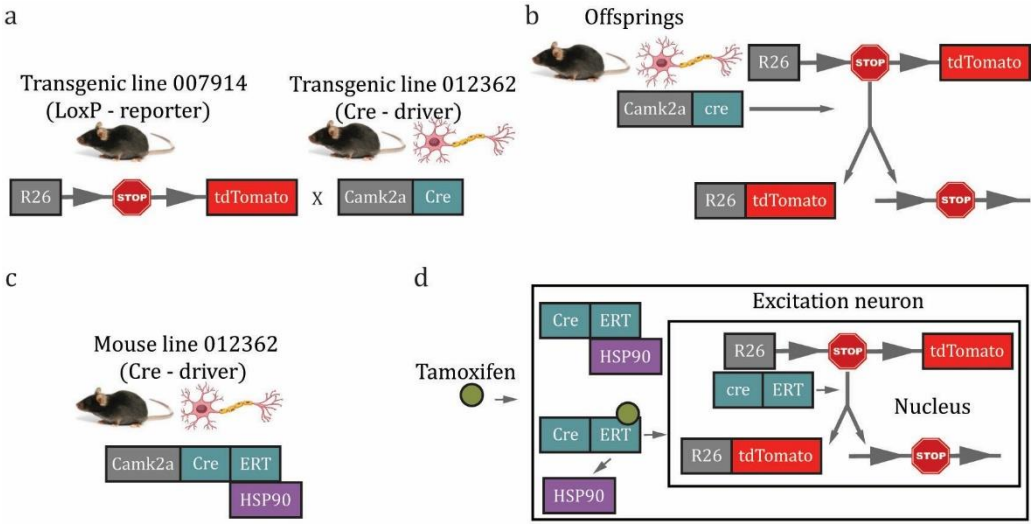

Figure 3.19: Scheme for breading of the genetically modified mouse carrying the fluorescent protein expressed in excitatory cells. a) Mouse line carrying the fluorescent protein cross bread with a mouse line carrying the Cre-recombinase. b) The Cre-recombinase cuts out the STOP enabling the tdTomato to be expressed in excitatory neurons. c) The Hitshot protein 90 inhibiting the activity of the Cre-recombinase. d) Effect of tamoxifen on activation of the Cre-recombinase leading to the expression of the R26tdTomato sequence.

Genotypization

When the offsprings are born, it is necessary to confirm the presence of the desired fluorescent protein. This was done by DNA extraction from a small part of the mice´s tissue (2-10 mg) used for genotypization. The reporter mice are homozygous, and the driver mice are heterozygous. Therefore, we can test the offsprings only for the presence of the heterozygous gene.

For the DNA release we used the REDExtract-N-Amp^{TM} Tissue PCR Kit (Sigma-Aldrich) containing the Extraction Solution, the Tissue Preparation Solution and the Neutralization Solution. The tissue sample is immersed for 10 minutes in the mix of the Extraction and Tissue solutions (25 and 6.25 μl respectively). After that the solution with the sample is vortexed for 1 min, incubated at 90° for next 3 minutes and vortexed again for 1 additional minute. After that the Neutralization solution is added (25 μl), the whole solution is vortexed and stored at 4°C until used for PCR reaction. The precise used volumes for 1 sample are listed in Table 3.1.

In the next step we prepare the solution for a polymerase chain reaction (PCR). The used volumes of the substances for a total volume of 5 μl (the smallest volume sufficient for amplification procedure) are written in Table 3.2. Firstly, the 2.5 μl of the REDExtract-N-Amp PCR Reaction Mix solution is used. It is a reaction mixture containing buffer, salts, dNTPs, and Taq polymerase. We add 1.5 μl of a mix of two primers – two short oligonucleotides of the DNA, specific for the forward and the reverse end of the fluorescent protein sequence. It is used to start the DNA replication at the specific start sequence with the enzyme Taq polymerase. The forward primer starts from the 3´to 5´end, whereas the reverse from 5´to 3´end respectively. Primers for mouse cross-breaded offsprings are forward oIMR9105 and reverse oIMR9103 for tdTomato, and forward 46549 and reverse oIMR9074 for Cre genes. As a last ingredient we add 1 μl of the neutralized DNA extract from mouse tissue sample. For the confirmation of the presence of the required fluorescent protein in tissue sample from cross-bread animals we also prepare a mixture of a control sample. It contains the tissue sample in which the presence of the testing gene has been already confirmed. We place the mixed solutions into the PCR Thermal Cycler (BioTech) and the amplification of DNA sequences than proceeds following the protocol from Table 3.3.

After amplification we visualize the results using Electrophoresis of nucleic acids. Firstly, we prepare 350 ml of the 1xTBE buffer for one agarose gel and for electrophoresis from 10x TBE Rotiphorese diluted in distilled water (Tab. 3.4). For the gel (Tab. 3.5) we first weighted 0.56 g of the agarose powder (Sigma-Aldrich), on the analytical scale. Next, we add 28 ml of 1xTBE buffer and 2.8 μl of SYBER for gel staining. The agarose in this solution is then dissolved in a microwave. We pour out the gel into the prepared electrophoresis chamber with the ladder to create small pits and let it dry. As a next step we add into the PCR sample 1 μl of a blue dye buffer ROTI Load to visualize the results. The gel is submerged under the TBE buffer in the electrophoresis box and after addition of the sample we set the constant current to 140A and let it run for ~30 min. The resulting bands in the gel are imaged using a UV lamp and a filter. The presence of the gene confirms an animal with positive expression of the tdTomato protein.

Protocols for genotypization:

The chemical substance	**Volume [μl]**
Extraction Solution	25
Tissue Preparation Solution	6.25
Neutralization Solution	25

Table 3.1: DNA Extraction protocol.

The chemical substance	**Volume [μl]**
REDExtract-N-Amp PCR Reaction Mix	2.5
Primer mixture	1.5
Tissue extract	1

Table 3.2: Protocol for sample preparation for PCR.

Step	Temperature [°C]	Time [min]	Cycles
Initial Denaturation	94	3	1
Denaturation	94	1	10
Annealing	65 (-0.5 per cycle)	1	
Extension	72	2	
Denaturation	94	1	28
Annealing	60	1	
Extension	72	2	
Final Extension	72	10	1
Final Hold	4	10 ≤ ∞	

Table 3.3: PCR protocol for DNA amplification.

TBE [ml]	TBE 10x [ml]	Water [ml]
350	35	315

Table 3.4: Protocol for buffer preparation for 1 electrophoresis and 1 agarose gel

Thickness of gel [cm]	Density [%]	TBE [ml]	Syber [μl]	Agarose [g]
0.5	2	28	2.8	0.56

Table 3.5: Protocol for preparation of 1 agarose gel for the electrophoresis chamber of the size of 10x10 cm.

Name	Composition	Supplier
REDExtract-N-Amp PCR Reaction Mix	buffer, salts, dNTPs, Taq polymerase	Sigma-Aldrich
REDExtract-N-Amp™ Tissue PCR Kit	Extraction Solution, Tissue Preparation Solution, Neutralization Solution	Sigma-Aldrich
Primer F - oIMR9105	oligonucleotides	Generi Biotech
Primer R - oIMR9103	oligonucleotides	Generi Biotech
Primer F - 46549	oligonucleotides	Generi Biotech
Primer R - oIMR9074	oligonucleotides	Generi Biotech
10xTBE	1.0M TRIS-borat, pH 8.3, 20mM EDTA	P-Lab
SYBER	SYBER™ Safe nucleic acid del stain red	Thermo Fisher Scientific
ROTI® Load DNA	Tris, Na-acetate, EDTA, bromophenol blue, xylene cyanol, glycerol	Carl Roth
Isoflurane	Isofluranum 1000mg/g	Vetpharam animal health, s.l.
Ketamine	Narkamon 50 mg/ml	bioveta
Xylazine - Xylazine Ecuphar	Xylazinum 20 mg/ml	Alverta werfft, Ecuphar N.V.

PBS	Dulbecco´s Phosphate Buffered Saline, without Ca and Mg, 20 ml	Lonza, 17-512Q
PFA	Paraformaldehyde	Sigma-Aldrich

Table 3.6: List of chemical solutions used during preparation of fixed brain slices.

3.5.2 Preparation of fixed mouse brain slices

For the case of *in vitro* imaging the tissue sample is obtained according to a following protocol. The mouse positive for the tdTomato protein is weighed and put into an anaesthesia using 5% isoflurane in 0.8-1 l/min oxygen. For a stronger anaesthesia, ketamine (0.05 μl) and xylazine (0.015 μl) are injected intraperitoneally. When the mouse is in a deep unconsciousness and there is no reactions to the pinch reflex, the heart is exposed by uncovering the thorax and the mouse is perfused with 4% paraformaldehyde - PFA, injected into the left ventricle. The brain is extracted and fixed in 4% PFA for ~30-72 hours at 4℃. After fixation, the brain is washed and stored in Phosphate Buffered Saline – PBS at 4℃. Brain sections are prepared on VT1200 vibratome (Leica) slicing the brain into 50-200 μm thick coronal sections which are further stored in the PBS or used directly for imaging. All chemical solutions including brands are listed in Table 3.6.

All animal procedures were conducted in accordance with protocols approved by the Branch Commission for Animal Welfare of the Ministry of Agriculture of the Czech Republic (permission No 47/2020). The surgical procedures and manipulation with the animal in the operating room and during experiment have been conducted by Tereza Tučková with a certificate number CZ 03422 of the licence approving her for experimental manipulation with laboratory animals.

3.5.3 Imaging of mouse brain slices

Before imaging, the system is calibrated following the procedure described in Section 2.5 with MMF immersed in the PBS. After calibration, the brain slice fixed on a Petri dish is inserted under the MMF. The imaging is done with the probe outside the tissue which after fixation becomes stiff and not suitable for fibre insertion. The results are shown in a set of images in Fig. 3.20. In the images we can see the fluorescent signal from excitatory neurons. However, to distinguish finer structures, such as dendrites or axons, the contrast is too low, and the background fluorescence is quite high.

These images demonstrate the samples, in which we have reached the maximum sparsity of fluorescent cells. Despite that, the density of fluorescent neurons is rather abundant yielding low contrast of images. It is reduced to such an extent that the sub-cellular structures are seldom distinguishable.

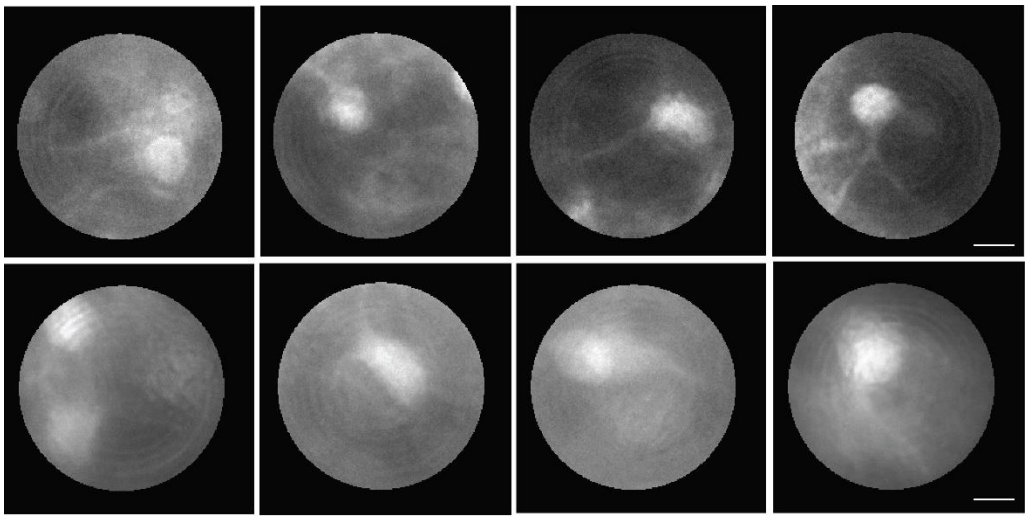

Figure 3.20: Examples from single-photon imaging through the MMF endoscope of excitatory neuronal networks expressing tdTomato in coronal section of the brain slices. The slices are thick 50 μm (top row) and 100 μm (bottom row). Scale bare is 10 μm.

As a reference, we acquired 2-photon excitation fluorescence microscopy images of the same sample and same region of interest (cortex) (Fig. 3.21).

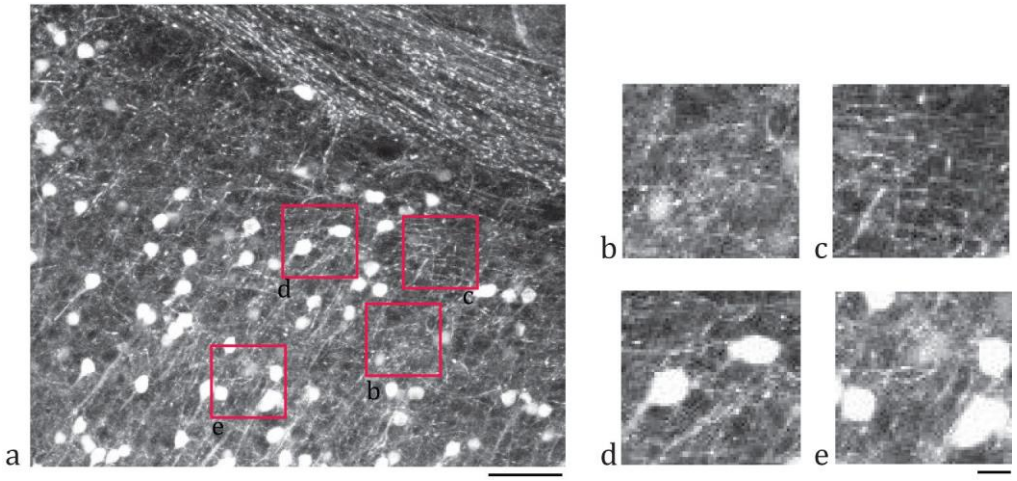

Figure 3.21: 2-photon microscopy images of brain slices of mouse-line expressing tdTomato in excitatory neurons. a) Maximum intensity projection of a z-stack containing 40 images 2 μm apart. The scale bar is 50 μm. b) – c) Zoomed-in regions of interest showing dendrites and spines. d) – e) Zoomed-in regions of interest of cells bodies. The scale bar for b) – e) is 10 μm and the size of FOVs is similar to the one acquired through the MMF.

These observations have clearly identified the need for out-of-focus light attenuation. Therefore, we proposed a new concept of confocal endo-microscopy using a custom-designed fibre probe.

3.6 Confocal imaging via MMF-based holographic endoscopy

The attempts to attenuate the out-of-focus light in MMF-based imaging has been attempted with two-photon microscopy in, for example, imaging of *ex vivo* neurons. It was achieved with an axially extended focus induced by chromatic dispersion of the used SI-MMF [142] or Cochlear hair cells using a GRIN MMF [143]. Other approaches exploited the principle of a digital [144] and physical [54] confocal pinhole. However, both confocal approaches work in practice only for the case of reflective imaging, in which the bandwidth of the back-propagated light is very small [145]. Therefore, none of the approaches so far published work as required for high-resolution fluorescent *in vivo* imaging.

This chapter presents a technique for out-of-focus light attenuation based on a new concept of MMF-based confocal holographic endoscopy. It can be practically utilized for imaging of fluorescent biological samples. Using fluorescent microspheres and fixed brain slices we demonstrate the principle and the proof of concept.

3.6.1 Multi-mode probe for confocal imaging

The central component of the confocal holographic endoscope is a custom-developed probe. It consists of a graded-index (GRIN) multi-mode fibre spliced at the tip of a step-index (SI) multi-mode fibre (GRIN-SI-MMF) (Fig. 3.22). A short segment of a GRIN fibre of pitch length (*P*) images an object placed at the entrance surface to the exit surface similar to a GRIN lens. A segment of length *P/4* images the object into infinity and thus can be used for beam collimation. We use a commercially available GRIN fibre (GIF625, Thorlabs, diameter of 125 μm with core diameter of 62.5 μm and 0.275 NA) with $P = 1.056$ mm, shortened to $L = 220$ μm.

Figure 3.22 shows the principle of the spliced probe. A point source placed in the working distance d (30 μm for our case) from the fibre distal end is collimated by this GRIN segment. It transforms its Cartesian coordinates into an angular spectrum of plane waves at the proximal end of GRIN fibre. These plane waves enter the SI fibre (FG050LGA, Thorlabs, diameter of 125 μm with core diameter of 50 mm and 0.22 NA) and propagate to its proximal side conserving the axial component of their *k* vectors [53, 93]. When the plane waves leave the proximal facet, they are imaged by a lens forming annular rings in the Fourier plane of the fibre. The combination of these two types of optical fibres enables a focal point at the imaging plane of the GRIN-SI-MMF to form a ring in the far-field of the spliced probe. When we change the focal point position radially from the fibre axis (from red point to the blue point in Fig. 3.22b), it results only in the change of the ring diameter [53].

As a result, light coming from outside of the focus in the focal plane will be imaged outside of the corresponding ring and can be filtered out using e.g. a DMD (DMD2 in an experimental setup in Fig. 3.24). The light coming from outside of the focal plane will yield a defocused ring in the far-field and therefore will be attenuated in the filtration process in the same way as in a classical confocal microscope.

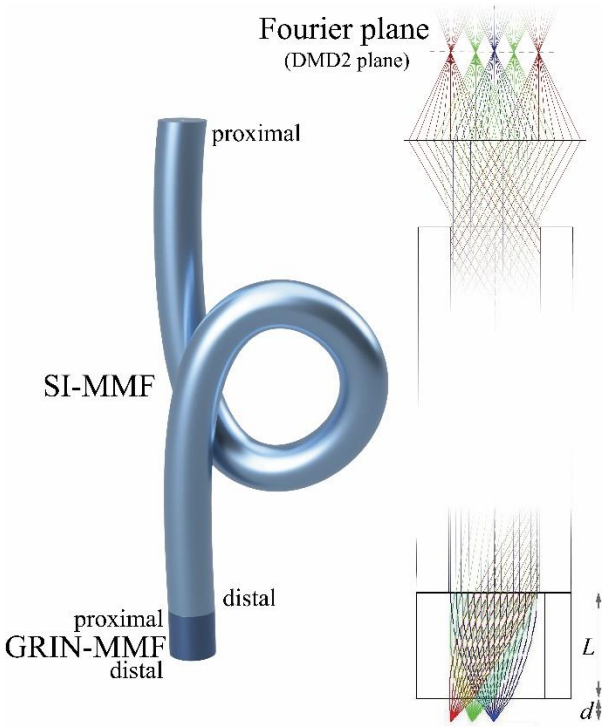

Figure 3.22: A confocal probe. a) The SI-MMF and the GRIN-MMF spliced together by their proximal and distal ends thus creating confocal probe. b) Illustration of the principle of light propagation through the SI-GRIN-MMF. The light from the point source at the imaging plane at distance *d* from the distal fibre facet propagates through the GRIN-MMF of length *L* and enters the SI-MMF in the form of plane waves. Thus, plane waves come out from the proximal side of the fibre and they form an annular ring in the Fourier plane of the fibre. The radial position of the light point source changes only the diameter of the formed ring.

3.6.2 Experimental setup

The core of the endoscope setup and its calibration is similar to the one described previously (Sections 2.4 and 2.5). The linearly-polarized light (532 nm) is collimated and diffracted by the DMD1. The lens L4 performs the Fourier transform of the DMD1 plane into the iris plane where the 1st diffracted order is selected. The combination of the lenses L5 and L6 demagnify the pattern in the iris plane. The beam is reflected by a dichroic mirror, collimated by the lens L7 and enters the proximal facet of the MMF in the form of a plane wave. This is required due to the phase-only modulation of the light for SI-GRIN-MMF probe imaging in the far field [146]. After passing the GRIN-SI-MMF, the light is combined with the reference beam, and during calibration process their interference is recorded on the CMOS camera (Fig. 3.23 Cal.1). For the measurement of the TM, we use the bases of input plane waves and output points. After calibration, the DMD hologram creates a ring-shaped field in the far field of the proximal end of the fibre, yielding a nice focal point with high PR at the output of the SI-GRIN-MMF probe.

The second part of the setup (Cal.2, Fig. 3.24) is used for the measurement and calibration of annular rings corresponding to scanning focal points within the imaging plane. These

rings are then used during imaging as confocal masks separating the signal originating from the scanning focal points from the signal excited in the out-of-focal planes.

The upper part is also used during imaging of the fluorescent sample to detects all the emitted signal or to upload the confocal masks on the DMD2 and detect a signal with the use of confocal filtration.

The calibration module 2 uses a red laser pointer (RLP) for generation of a red-trans-illumination point at the calibrated focal plane. The red light propagates through a non-polarising beamsplitter cube (NPBS) and is aligned into the SMF3. The outcoming light is focused into the focal plane of the MMF by an objective (Obj.). The appropriate location of each red focal spot is determined from an image of the corresponding green calibrated focal spot, which is coupled into the SMF3 and detected on the photodiode. The different positions are then generated by scanning the field of view by a SMF3 fixed to an *x*-*y* stage.

The generated red spot mimics the fluorescent signal emitted purely from the focal spot. It propagates backward through the GRIN-SI-MMF, passes a dichroic mirror (DM), and forms a ring on DMD2. The mirrors on DMD2 reflect the signal from within the ring to the detector - photomultiplier tube (PMT1). During the sample imaging for every output scanning point, the calculated confocal masks are simultaneously displayed on DMD2, thus reflecting the light only off the micro-mirrors from the confocal ring. It contains the signal only from the scanning points, which is detected on the PMT1. The rest of the signal is reflected outside onto the PMT2. For comparison of the effect of the confocal filtration, the non-confocal image is obtained, and it can be done in two ways: the first way is that after acquisition of one image with confocal filtration, all mirrors on the DMD2 switch into the ON position thus reflecting all light onto PMT1 acquiring the non-confocal image. The second way is to display the confocal masks on DMD2 reflecting the signal from the confocal ring onto PMT1, while the rest of the signal is reflected onto the PMT2. The sum of the signals from both PMTs thus yield a non-confocal image containing the signal from the scanning points as well as from outside of the focus.

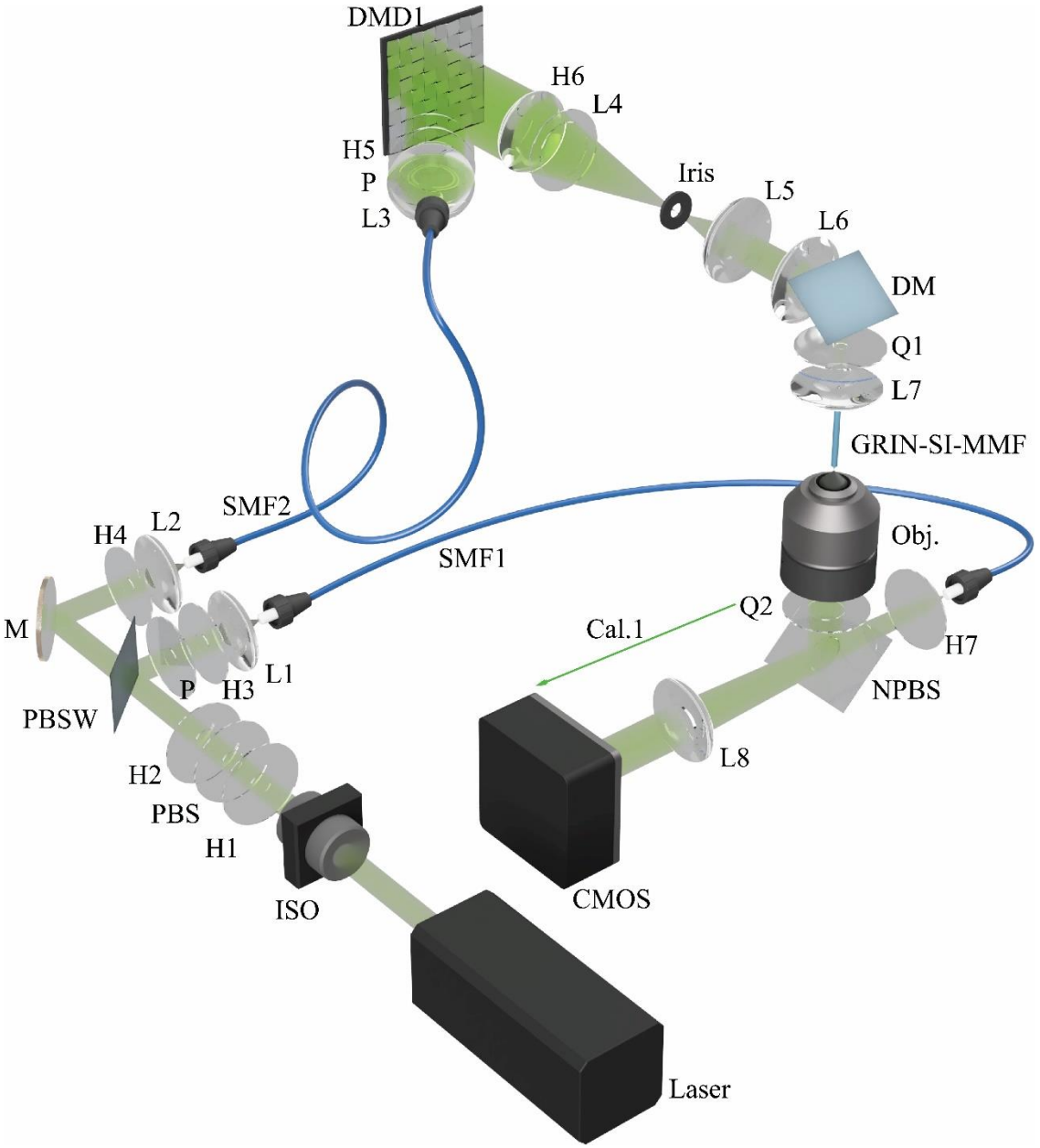

Figure 3.23: A part of the experimental setup intended for calibration of the scanning focal points. **M**: Mirror BB1-E01, Thorlabs, **PBS**: Polarizing Beam Splitter, CCM1-PBS25-532/M, Thorlabs, **H1-7**: Multi-Order Half-Wave Plate WPMH10M-532, Thorlabs, **PBSW**: Polarizing Plate Beamsplitter PBSW-532, Thorlabs, **L1, 2**: Lens C240TME-A, Thorlabs, **SMF1,2**: Single Mode Fibre P3-488PM-FC-2, Thorlabs, **P**: Linear polarizer LPVISE 100-A, Thorlabs, **L3**: Achromatic Doublet AC254-075-A-ML, Thorlabs, **L4**: Achromatic Doublet AC254-200-A-ML, Thorlabs, **L5, 7**: Achromatic Doublet AC080-010-A-ML, Thorlabs, **L6**: Achromatic Doublet, AC254-080-A-ML, Thorlabs, **DM**: Dichroic Mirror, 540 nm longpass, custom made, **Q1, 2**: Multi-Order Quarter-Wave Plate, WPMQ10M, Thorlabs, **GRIN-MMF**: Graded-Index Multimode Fibre GIF625, Thorlabs, **SI-MMF**: Step-Index Multimode Fibre FG050LGA, Thorlabs, **Obj.**: Objective Olympus Plan N, 20x, 0.40NA, **NPBS**: Non-polarizing Beamsplitter Cube BS016, 50:50, Thorlabs, **L8**: Achromatic Doublet, AC254-150-A-ML, **DMD1, 2**: Digital micro-mirror device V-7001 (DLP 7000, Texas Instruments), ViALUX, **Iris**: Iris diaphragm SM1D12C, Thorlabs, **CMOS**: Camera Ace acA640-750um, Basler.

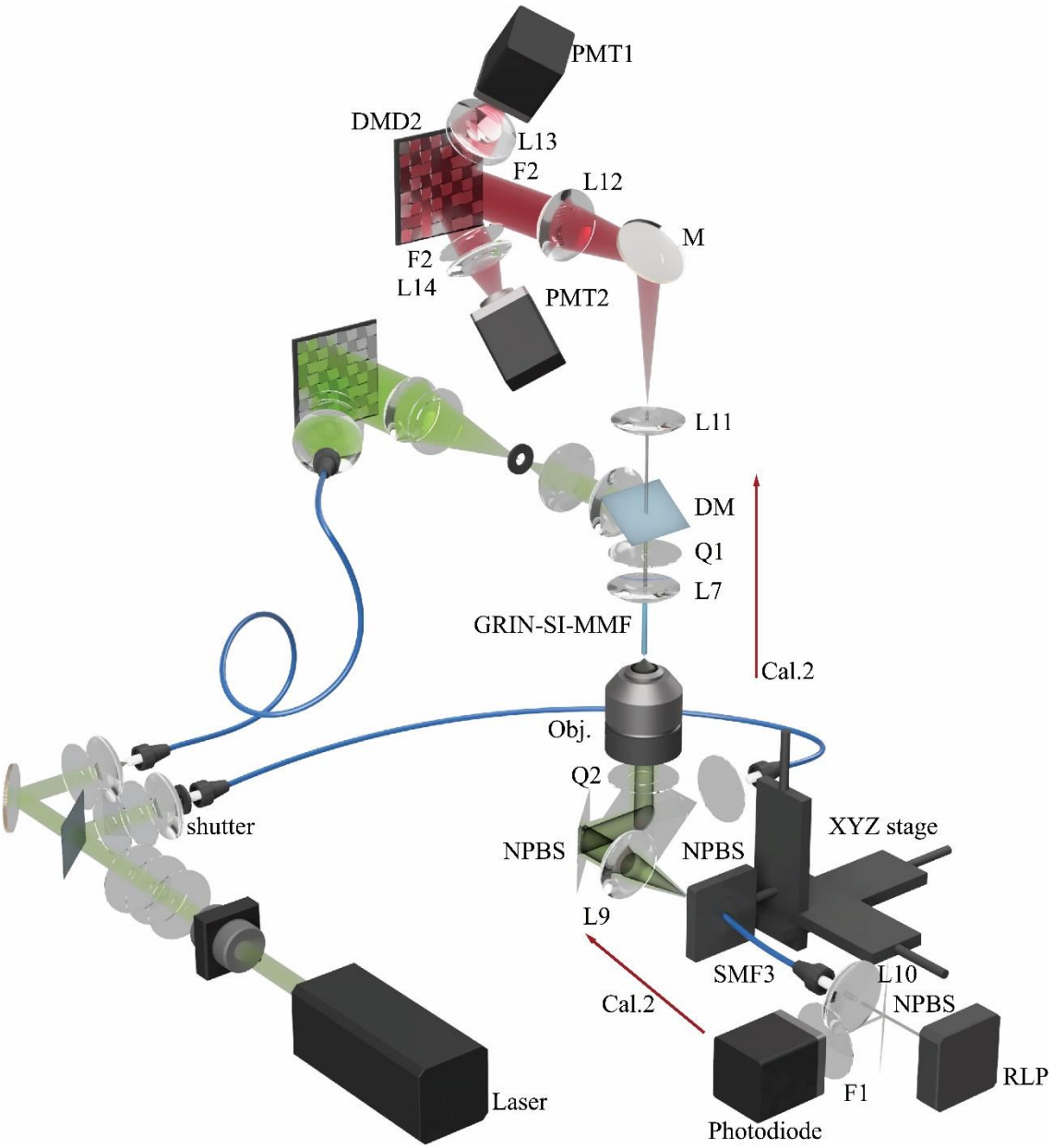

Figure 3.24: A part of the experimental setup intended for the calibration of the annular rings. **L7**: Achromatic Doublet AC080-010-A-ML, Thorlabs, **DM**: Dichroic Mirror, 540 nm longpass, custom made, **Q1, 2**: Multi-Order Quarter-Wave Plate, WPMQ10M, Thorlabs, **GRIN-MMF**: Graded-Index Multimode Fibre GIF625, Thorlabs, **SI-MMF**: Step-Index Multimode Fibre FG050LGA, Thorlabs, **Obj.**: Objective Olympus Plan N, 20x, 0.40NA, **NPBS**: Non-polarizing Beamsplitter Cube BS016, 50:50, Thorlabs, **L9**: Achromatic Doublet AC254-060-A-ML, Thorlabs, **SMF3**: Single Mode Fibre P3-488PM-FC-2, Thorlabs, **F1**: Filter ET525/50, Semrock, **L12**: Achromatic Doublet, AC254-150-A-ML, **L11, 13**: Achromatic Doublet AC254-075-A-ML, Thorlabs, **L14**: Achromatic Doublet, AC254-080-A-ML, Thorlabs, **F2**: Filter FELH0550, Thorlabs, **Laser**: Laser Verdi, G-Series (G5), Coherent, **ISO**: Isolator Tornos Serie 500-1030nm (04-532-00012), **shutter**: Diaphragm shutter with controller, SHB1T, Thorlabs, **DMD2**: Digital micro-mirror device V-7001 (DLP 7000, Texas Instruments), ViALUX, **Iris**: Iris diaphragm SM1D12C, Thorlabs, **RLP**: Red laser pointer 650 nm, **Photodiode**: Photodiode PBW34, Vishay Semiconductors, **PMT**: Photomultiplier Tube PMT2101/M, Thorlabs.

3.6.3 Calibration procedures of scanning points and confocal masks

In the first calibration step (Fig. 3.23), the transmission matrix (TM) of the system is measured as described in Section 2.5. Sequential projection of the calculated holograms on DMD1 results in a focal point scanning across the whole field of view in the focal plane similar to a scanning microscope.

In the second calibration step using the second calibration module (Fig. 3.24), red light from the focal points is back-propagated through the GRIN-SI-MMF and the annular rings formed in the far field of the proximal probe facet are imaged. Subsequently, the confocal masks are calculated. The calibration is typically carried out for a set of ~110 points distributed in a star-shaped grid across the whole field of view (Fig. 3.25b). For every tested green epi-illumination focal point, a red trans-illumination point is generated by a sub-stage red laser pointer (RLP) at the same location in the imaging plane. The appropriate location in the imaging plane of each red focal spot is determined from an image of the corresponding green focus which is generated by scanning the field of view by the SMF3 fixed to an *x-y* stage. The x and y stage coordinates at the intensity peak determine the position of the SMF3 for the generation of the corresponding red spot. Red light from this focal point propagates through the GRIN-SI-MMF in the backward direction, passes through the dichroic mirror, and forms an annular ring in the far-field of the proximal probe facet, where another DMD is placed (DMD2). The annular ring formed on DMD2 is scanned by domains of 8x8 micro-mirrors bins reflecting the signal from the mirrors in the ON position onto the PMT1.

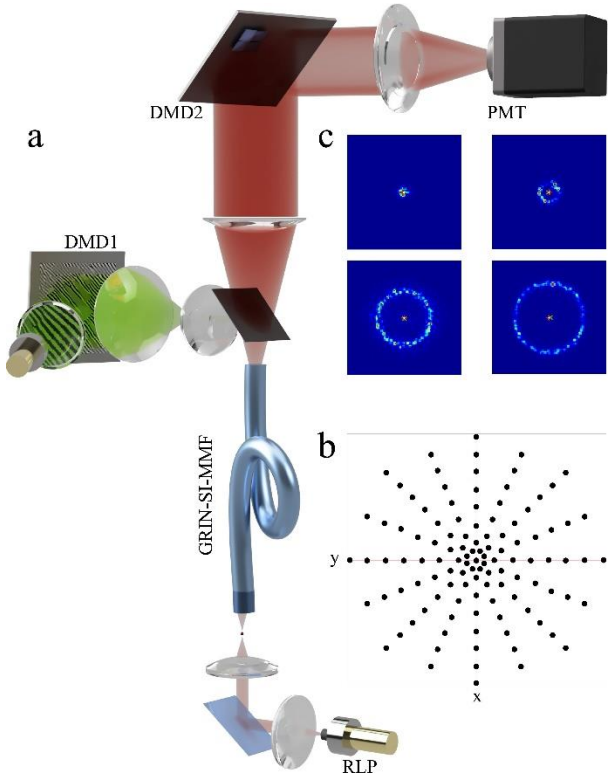

Figure 3.25: A scheme of the calibration procedure. a) Principle of scanning foci in the image plane. b) Organization of the red foci used for calibration of rings on DMD2. c) Detected annular rings on PMT particular to red foci position.

The detected images (Fig.3.25c, "Original data" in Fig. 3.26) serve for estimation and subsequent calculation of confocal masks. In the first step a grid with coordinates for fits is defined in which, by eliminating the thresholded values of the background and maximal intensity, the data for initial estimation of parameters are defined. This creates an estimated map for every measured ring (Fig. 3.26b). We estimate the parameters of the detected ring. When the DMD2 is perpendicular towards beam incoming from the fibre, the reflected signal detected on PMT1 is of the ring shape. However, the perpendicularity is not guaranteed. In that case the detected signal would have an elliptic shape. Therefore, to eliminate the possibility of ellipticity and to obtain masks corresponding to the real shape, as a next step the images for all tested points are fitted with ellipse with the intensity profile I respecting a Gaussian function according to equation

$$I(r) = A \cdot exp\left[-\frac{(r-r_0)^2}{2\sigma^2}\right] + B, \tag{3.13}$$

where A represents the amplitude of the fit, B is the offset, σ controls the width of the fit and r_0 determines the central radius of the ring. An example of such fit is demonstrated in Fig. 3.26c. We also fit for the centre of the ring corresponding to the optical axis of the probe (Fig. 3.26f, g). From measured axes ratio (Fig. 3.26d) we can however see that the measured data in this case are more of a ring shape. Thus the Eq. (3.13) is relevant in its form. The measured data from Fig. 3.26 serve for calculation of the final thickness, axes ratio and *x*-*y* centre of the rings.

Next, the fitted amplitude A is set to 1 and the offset B to 0. The confocal masks for the ON mirrors are then calculated as

$$exp\left[-\frac{\left(r-r_{0,M}\right)^2}{2{\sigma_M}^2}\right] \geq CF. \tag{3.14}$$

The values of σ_M and ring *x*-*y* centre are calculated as averages of fitted values across all recorded rings (Fig. 3.26e, f, g). The averages are also used for calculation of masks of all scanning points which were not tested. The radii $r_{0,M}$ of masks are linearly increasing with increasing radial distance of the tested focal point from the probe centre r_F. When the centre *x* and centre *y* are defined, at the centre where $r_F = 0$, the $r_{0,M}$ is equal to 0, all calculated radii $r_{0,M}$ are fitted with a linear function r and the radii of all masks can be determined from this fit (Fig. 3.26h). Next, the measured ring is interpolated to full DMD2 coordinates. The interpolated data then serve for calculation of the accepted and rejected light resulting in masks for accepted and rejected pixels (Fig. 3.26i, j). Finally, from fitted and calculated data we obtain a final ellipse with DMD2 resolution (Fig. 3.26k), prepared for creation of confocal masks for all output point.

The threshold to filter the normalized Gaussian mask is set by a *confocal factor* (CF) which is defined in an interval $<0,1>$ and yields annular rings with different thicknesses. In this sense, $\mathrm{CF} = 1$ corresponds to maximum signal filtration, $\mathrm{CF} = 0$ corresponds to no filtration of the detected light and $\mathrm{CF} = 0.5$ yield the mask thickness of full width at half maximum (FWHM). The masks are then binarized and used to control DMD2 (Fig. 3.26l):

0 drives the micro-mirrors in the OFF position and 1 in the ON position (an example can be seen in Fig. 3.27l “Hologram for DMD”). Maximum filtration at CF =1 yields a mask thickness of a single DMD´s micro-mirror in the ON position and minimum filtration CF = 0 a mask with all mirrors ON.

Scanning points with a decreasing radial distance in the focal plane correspond to annular ring masks with a decreasing radius. Decreasing the mask radius more than the theoretical resolution limit will lead to a decrease of detected intensity of the corresponding central points. In practice, the intensity decrease artefact appears even for mask of bigger diameter. Therefore, we measured the minimum mask diameter experimentally aiming for zero intensity drop in the centre of an image of a 2D homogeneous sample.

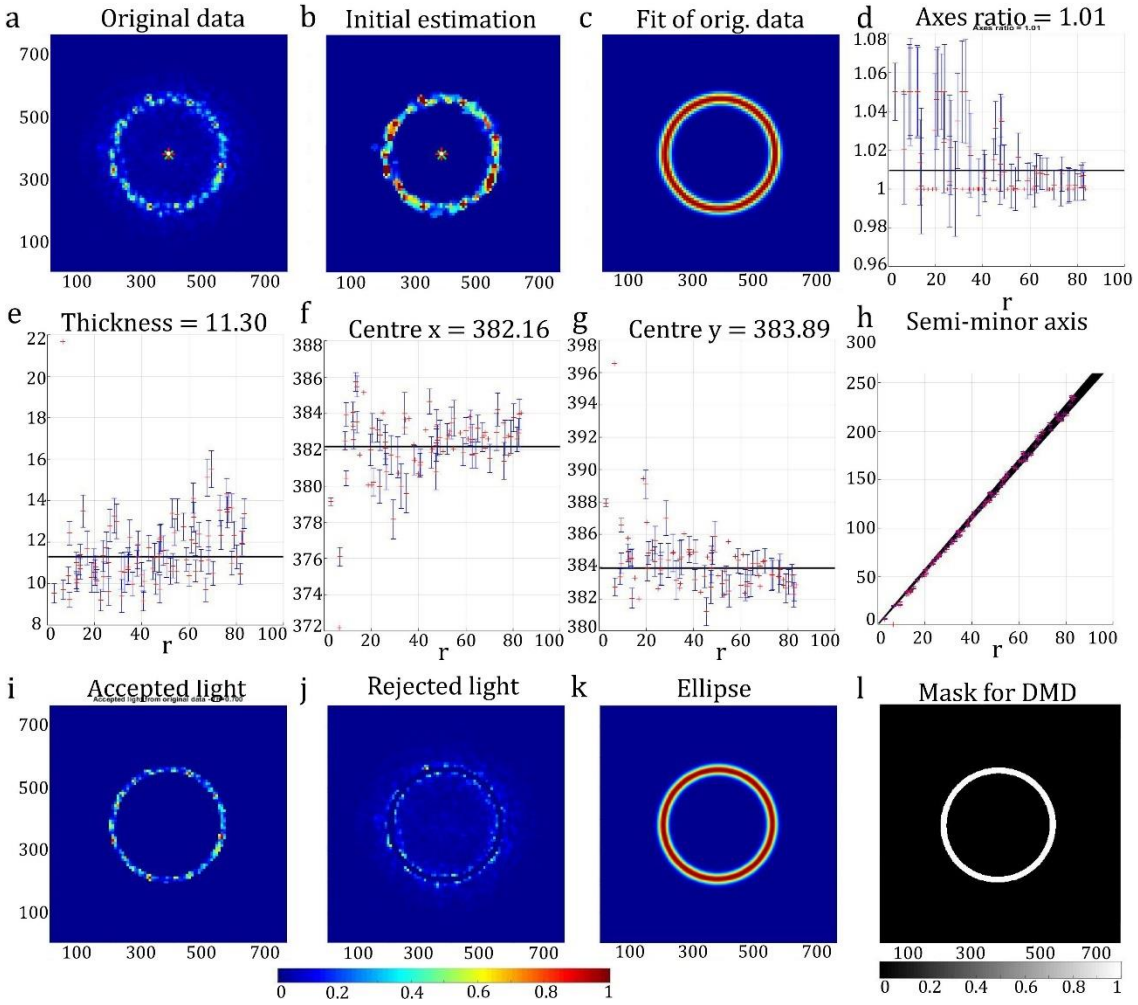

Figure 3.26: Steps of the fitting procedure. a) The original data detected on the PMT with measured centre x and y. b) Data for initial parameters estimate. c) The fit of the original data. d) Ratio of both axes from the ellipse fit across the whole radius of the FOV. e) Thickness of all detected rings with different radii. f)-g) The position of the centres in the x and y axis for all measured rings. h) Linear fit of all calculated radii $r_{0,M}$. i) The area of the intensity, which will be accepted for following calculation. j) The area of the intensity, which is rejected and will no longer play a role in the calculation. k) The ellipse from averaged values interpolated to full DMD2 coordinates serving for hologram generation. l) shows such mask corresponding to a focal scanning point at particular position in the FOV.

3.6.4 Probe and sample preparation

GRIN-SI-MMF probe

In the first step a piece of a SI-MMF of a length ∼2-3 cm is right-angle cleaved using a fibre cleaver Fujikura CT101. Further, a segment of a GRIN-MMF of length ∼2 cm is spliced at the distal facet of the SI-MMF (FG050LGA, Thorlabs, diameter of 125 μm with core diameter of 50 μm and 0.22 NA) using the 3SAE Large Diameter Splicing System – LDS 2.5, 3sae Technologies, Inc. Then, the spliced GRIN fibre (GIF625, Thorlabs, diameter of 125 μm with core diameter of 62.5 μm and 0.275 NA) is right-angle cleaved to length L ∼220 μm respecting a $P/4$ imaging length in order to achieve a working distance of d ∼30 μm.

Sample preparation - microspheres

For characterization of the confocal performance of the endoscope a 2D phantom sample was prepared consisting of fluorescent microspheres (diameter of 0.82 μm, Polymer Microsphere, R820, Duke Scientific) dispersed in water (1:1000) and dried on a cover glass (0.7 mm thick).

A 3D phantom sample was prepared by dispersing fluorescent microspheres (FluoSpheres Carboxylate-Modified Microspheres, diameter 2.0 μm, Nile Red, F8825, Thermo Fisher Scientific) in 0.5% agarose gel (Sigma-Aldrich).

3.6.5 Imaging performance of the confocal holographic endoscope

Before the TM measurement, the precise working distance d of the GRIN-SI MMF has to be measured. This distance determines the focal plane of the probe for imaging. The proximal fibre facet is illuminated with a plane wave under an arbitrary angle that couples into the fibre core. An annular ring is generated at the distal end of the probe and imaged on the CMOS camera. The working distance is measured by subsequently focusing the annular ring at its waste and the distal facet of the probe with the objective on a motorized XYZ stage.

If the working distance d has been determined correctly, the focal plane for different confocal factors should be identical. We confirmed this by imaging of fluorescent microspheres on a cover slip in a z-stack using 5 different CFs (Fig. 3.27).

We have measured the working distance in the case of non-confocal imaging and for four different confocal factors (CF = 0.002, 0.602, 0.834 and 0.98) by refocusing fluorescent microspheres. First, all measured images of the microspheres have been filtered using a simple convolution yielding spatial bandpass filtering (see an example in Fig. 3.27a). The filtration procedure implements a real-space bandpass filter that suppresses pixel noise and long-wavelength image variations while retaining information of a characteristic size. In a next step we have find local maxima in an image to pixel level accuracy, which provided a rough guess of microspheres. Then we calculated their centres to sub-pixel accuracy.

Figure 3.27b shows the average intensity across all fluorescent microspheres marked with red cross at different working distances. The intensity profiles have been normalized for all confocal factors. The peak of the intensity determines the position with the sharpest focus – the appropriate working distance. The intensity profiles for CFs 0-0.834 peak at d = ~24 μm from the distal facet. The intensity peak for CF 0.98 is slightly shifted which can be caused by high sensitivity of the high confocal factors for small micrometre shifts in the z-axis. After calibration, the CF = 0.98 has thickness of ~5 pxl, therefore shifting the ring even by 1 pxl on the DMD2 has a strong effect on the resulting filtration. Using such a high CF will yield very strong filtration and is not suitable for imaging of small structures with weak fluorescence signal. Therefore, it has not been used in further experiments. In the case when intensity maxima for different CFs peak at different working distances, the TM should be measured for a new working distance. Therefore, the direction in which the peak is shifted with an increasing CF identifies the direction and the offset distance of the new focal plane.

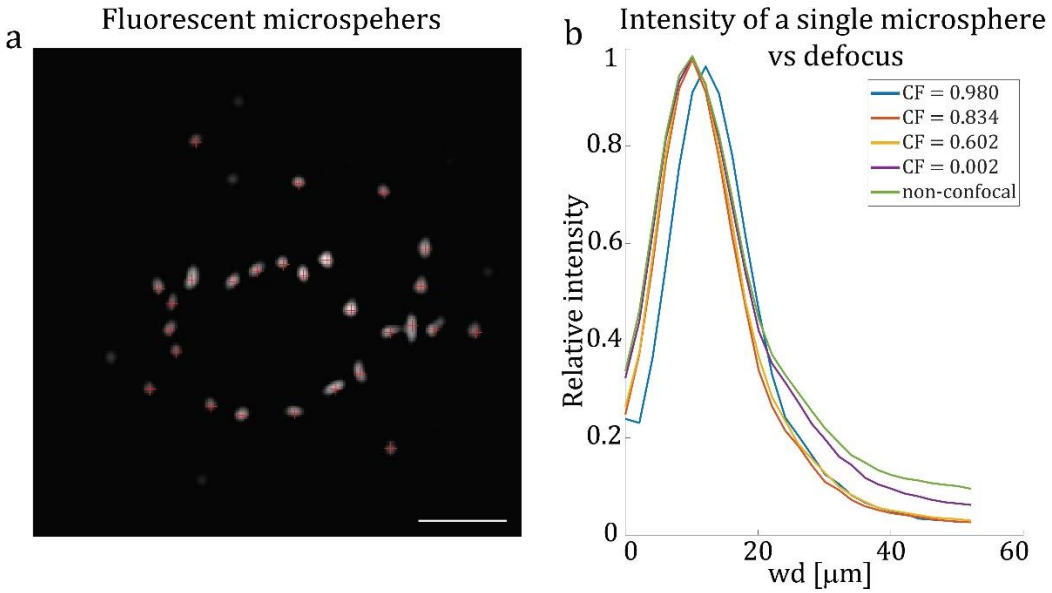

Figure 3.27: Verification of the calibrated working distance. a) Fluorescent microspheres (dia 0.82 μm) on a coverslip imaged at a working distance (wd) of 24 μm. Each image was filtered, and individual microspheres were detected by PMT. Scale bar is 10 μm. b) Normalized intensity at different working distances separated by 2-μm. The intensity was calculated as an average across all microspheres detected by PMT and distinguished as a single object.

Single-photon PSF characterization for the confocal endo-microscopy

To determine the quality of the imaging, we first characterized the 3D point spread function (PSF) of the confocal endo-microscopy imaging process and compared it to the corresponding non-confocal PSF (Fig. 3.28).

We illuminated a sub-resolution sized fluorescent microsphere (0.82 μm in diameter) with a single focal spot and scanned the microsphere in 3D while three different CFs were applied. Figure 3.28 shows the x-y scans of 3 different focal points positioned in the middle (a), at $0.8r$ (b) and 0.4r (c) from the centre, where r is the radius of the FOV (~25 μm).

The intensity was detected without confocal filtering (CF = 0) and with 3 different confocal factors CF = 0.002, 0.127 and 0.834 corresponding to rings with a thickness of 56, 32 and 9 micro-mirrors, respectively. From the results, two confocal effects can be clearly seen. Firstly, increasing the CF leads to a significant attenuation of background in the focal plane which is reflected in the increase of the effective enhancement factor (EEF) and effective power ratio (EPR).

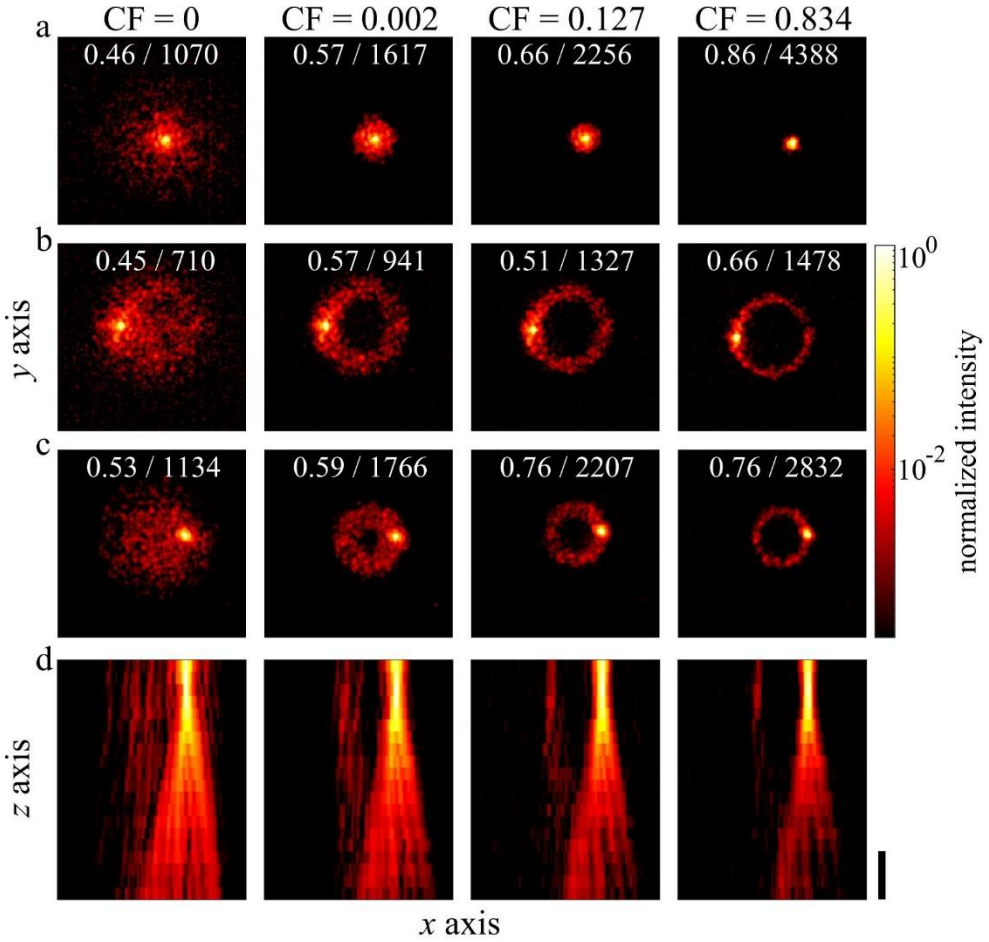

Figure 3.28: 3D PSF of the holographic endoscope with different extent of light filtration. a)-c) Lateral point spread functions (PSF) measured using a sub-resolution fluorescent microsphere (dia 0.82 μm) for three different focal points in the regime of non-confocal imaging CF = 0 and using three different confocal factors (CF = 0.002, 0.127, 0.834). Each image features values of the effective power ratio (EPR) and effective enhancement factor (EEF). Increasing the CF clearly attenuates the speckled background. d) An axial PSF for the focal point in (c) as a sum of intensities across *x*-*y* plane. The higher CF the stronger out-of-focus light attenuation which is visible also along the optical axis z. Scale bar is 20 μm.

The EEF is defined as the ratio of peak intensity at the focal point to the average level of speckled background and the EPR represents the power deposited in the focal spot relative to the total power in the focal plane [130]. Since the PSF changes across the field of view, the EEF and EPR enhancements were measured for three radially different positions of the focal spot. The EEF for the selected foci increase by 310 (Fig. 3.28a), 108 (Fig. 3.28b) and 150 % (Fig. 3.28c), respectively when CF = 0.834 is used. Using the same CF, the EPR values increase by 80 (Fig. 3.28a), 46 (Fig. 3.28b) and 43 % (Fig. 3.28c),

respectively. Exceptions from a monotonic increase of the EPR with CF (Fig. 3.28b) reflects a sub-optimal fit of the PSF data with a narrower Gaussian function. The Gaussian fit better corresponds to the course of the measured data compared to the fit with Airy function.

Secondly another "confocal" effect is a significant attenuation of light from the out-of-focus planes which can be seen from the *x*-*z* projections Fig. 3.28d, where the points in *x* are a sum of intensities along the *y* axis, for each *x*-*y* plane. Figure 3.29 demonstrates further the attenuation in the axial intensity averaged across the azimuth.

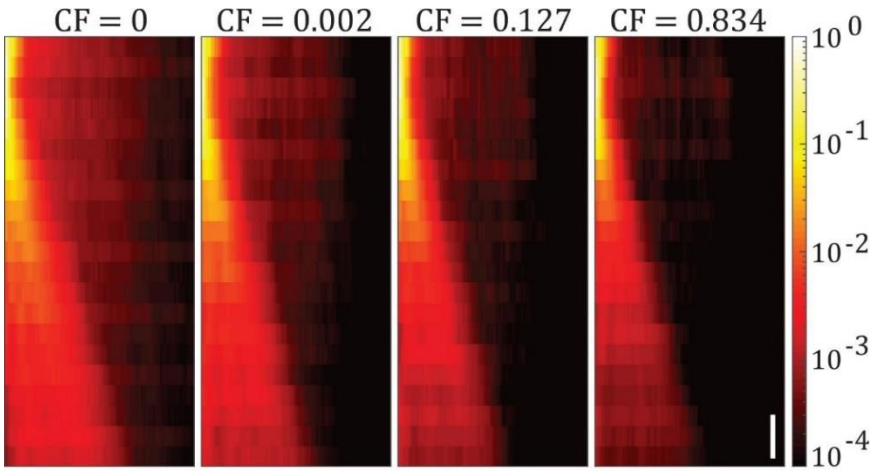

Figure 3.29: Azimuthally-averaged intensity profiles of the PSF in the axial plane. Scale bar is 10 μm.

The suppression of the out-of-focus light is also demonstrated in Figure 3.30. The graph shows total intensity in each axial plane without confocaling and for tested CFs. The measured data are fitted by a Laplace function. Positive values of *z* are towards the fibre facet and negative values are in direction away from it.

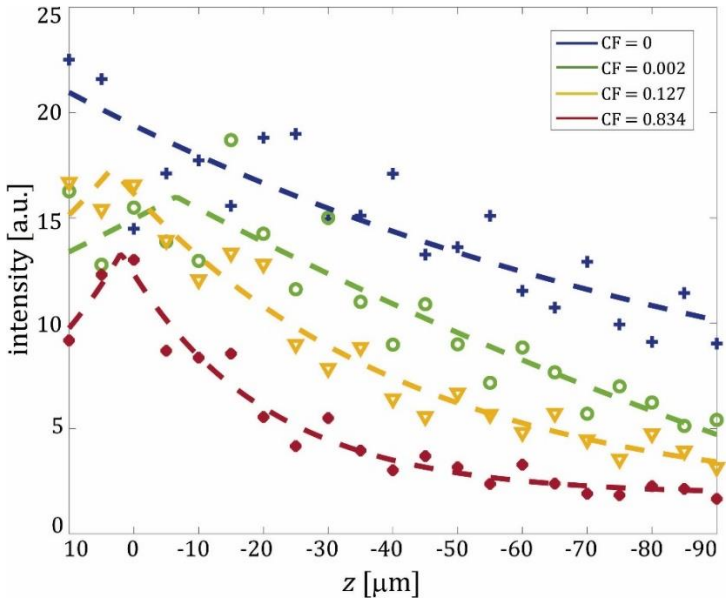

Figure 3.30: Total intensity in different planes along the optical axis z. The measured values are fitted by Laplace function and the fit is rendered as dashed lines.

Volumetric imaging of a phantom sample

To verify the results of previous measurement, we tested the imaging performance in a 3D model sample of fluorescent microspheres (0.82 μm in diameter) dispersed in an agarose gel 1:1000.

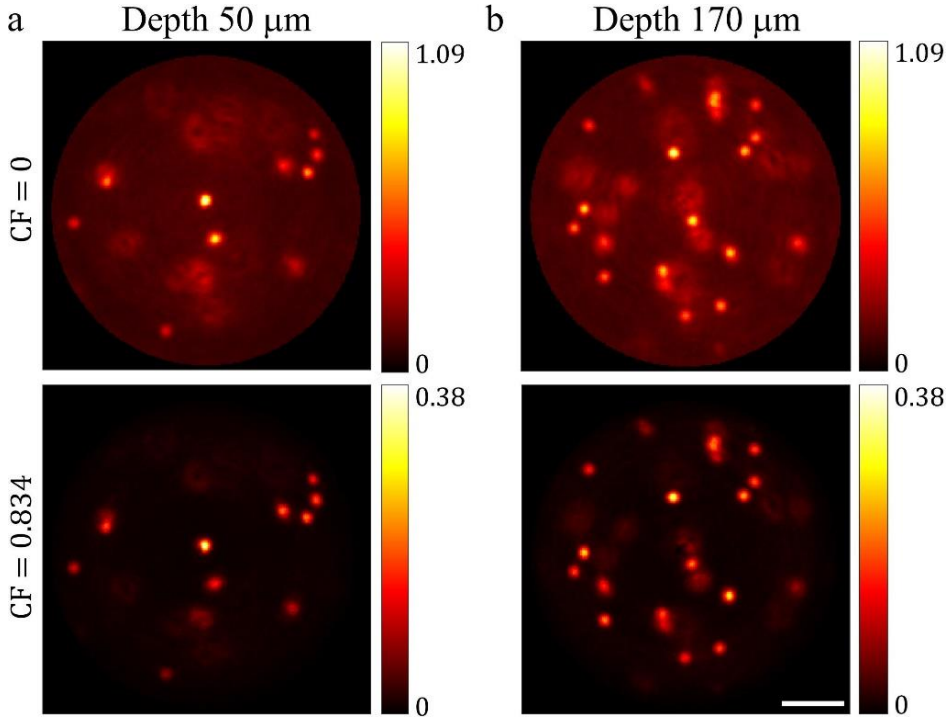

Figure 3.31: Imaging of a 3D model sample of fluorescent microspheres (dia 0.82 μm) dispersed in agar at depth 50 μm (a) and 170 μm (b). Confocal filtration leads to attenuation of the out-of-focus light. Scale bar is 10 μm.

Figure 3.31 shows two example FOVs imaged at depth of 50 μm and 170 μm, respectively. Also in this 3D model sample, the out-of-focus light is clearly attenuated after confocal filtration leading to decrease of the background intensity and increase of image contrast.

Preparation of the tissue sample for testing the confocal imaging

Moving towards real experimental conditions, we tested holographic confocal micro-endoscopy in imaging of fixed mouse brain slices.

A transgenic mouse line with a tdTomato expressed in excitatory neurons was generated as described in Section 3.5.1. The brains were extracted and fixed as described in Section 3.5.2.

Confocal endo-microscopy of fixed brain slices

We calibrated the confocal masks for CF = 0.834. Figure 3.32 shows the comparison of non-confocal (CF=0, top row) and confocal images (CF=0.834, bottom row) of excitatory neurons expressing tdTomato. The non-confocal signal was determined

by adding the confocal signal detected by PMT1 and signal detected by PMT2 (reflected from the OFF mirrors).

The out-of-focus fluorescence signal is clearly attenuated in the confocal images. As a result, we can distinguish somas of the neurons which are in the focal plane, while the signal from the somas outside of the plane is suppressed (Fig. 3.32b). The background of the images is nicely reduced, which increases the contrast of the images, i.e. yields higher signal to background ratio. This enables detection of thin neuronal processes not resolved in the non-confocal images (Fig. 3.32a, c image). The effect of the confocal filtration is quantitatively demonstrated in histograms with distributed intensities from corresponding images above. For the non-confocal imaging (CF=0) in cases Fig. 3.32a and b, the contrast is low and the neuronal somas are not distinguishable. This can also be expected from the corresponding histogram – its width signalizes a low image contrast and a high amount of background signal and out-of-focus signal. However, after applying confocal filtration using CF = 0.834 the histogram is visibly narrower. This corresponds to higher contrast in images obtained with confocal filtration due to the attenuation of the background noise and out-of-plane signal and therefore well-resolved and visible features in the obtained images.

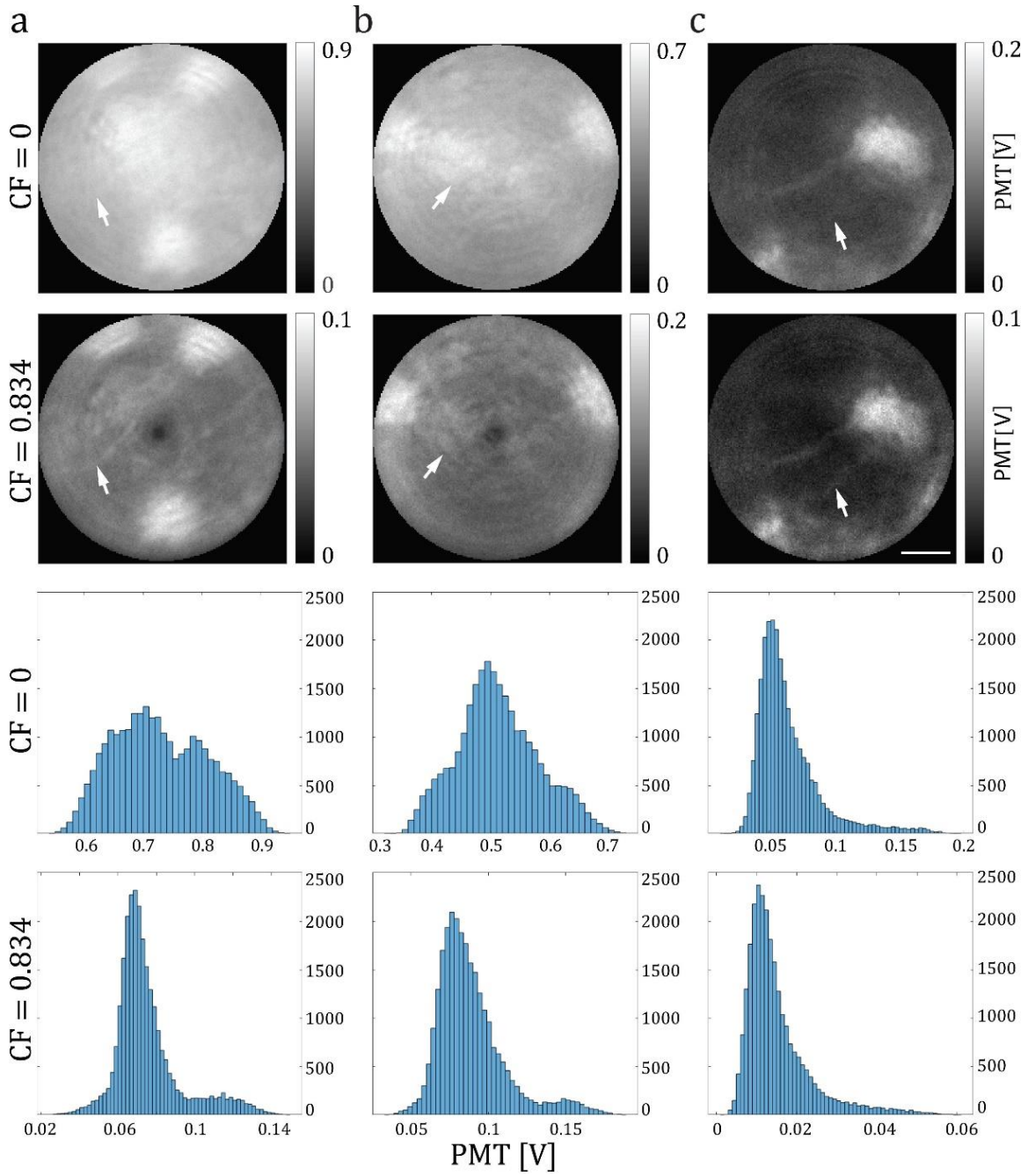

Figure 3.32: Imaging of neurons expressing tdTomato in fixed brain slices. Three different fields of view (a, b, c) imaged with CF = 0 (top) and CF = 0.834 (bottom) and corresponding histograms of their intensities. a), c) A neuronal process emerged after confocal attenuation of the background. b) A putative soma disappeared after attenuation of light from out-of-focus planes. Scale bar is 10 μm.

3.6.6 Imaging performance of the confocal holographic endoscope using a side-view probe

When imaging with the MMF probe through the brain tissue the fibre facet affects the tissue with all its surface, the imaging is performed *en face*. A moving probe results in mechanical tear of the tissue which damages especially the cells of interest. A significant advantage offers a side-view probe developed in our group and applied for *ex-vivo* and *in-vivo* imaging [147, 148]. Its distal end is polished under an angle of 45° and coated with a reflective layer. The focal plane is formed off-axis along the longitudinal axis of the fibre (Fig. 3.33).

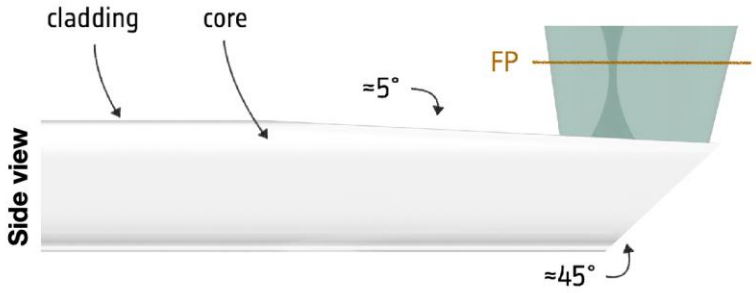

Figure 3.33: Schematic illustration of the novel side-view MMF imaging probe, with indication of the angles of the polished surfaces and focal plane (FP). For a side-view imaging, the light propagates along the fibre core and at the end is internally reflected on a 45°-polished surface with a reflective coating, leaving the fibre through the flat 5°-polished output facet and is focused on FP at the distance set during a calibration procedure. Reprinted from [151].

This decreases significantly the displacement of the tissue when moving the probe [151]. Therefore, it is highly desirable to implement the confocal modality also through the side-view probes.

The GRIN-SI-MMF side-view probes were prepared using a 3SAE Large Diameter Splicing System – LDS 2.5, 3sae Technologies, Inc. The fibre facet has been polished in a three-step process to the 45° using fibre polishing sheets (LF6D, LF1D and LFCF, Thorlabs) attached to a fast-spinning disk, which is fixed on a custom-designed grinder machine. Polished side was than coated with aluminium using vacuum evaporator JEE-42O, JEOL.

Single-photon PSF characterization for the confocal endo-microscopy using a side-view GRIN-SI-MMF probe

First, we have measure the PSF of the side-view probe without confocal filtration ($CF = 0$) and using confocal factor $CF = 0.867$ corresponding to a mask thickness of 8 micro-mirrors in a similar manner to the straight-view mode presented in Section 3.6.5. We illuminated a sub-resolution-sized fluorescent microsphere (0.82 μm in diameter) with a single focal spot and scanned the microsphere in 3D, while different CFs were applied. Figure 3.34 show *x-y* scans of three different focal points at $0.8r$ (a), $0.4r$ (b) and in the middle (c) of the FOV, where *r* is the radius of the FOV ($\sim$25 μm).

Similarly to the straight-view mode, from the results, two confocal effects can be clearly seen. Firstly, confocal filtration leads to a significant attenuation of background in the focal plane which is reflected in the increase of the effective enhancement factor (EEF) and effective power ratio (EPR). The EEF for the selected foci shown in Fig. 3.34 increase from the left by 315, 78 and 114%, respectively when CF= 0.867 is used.

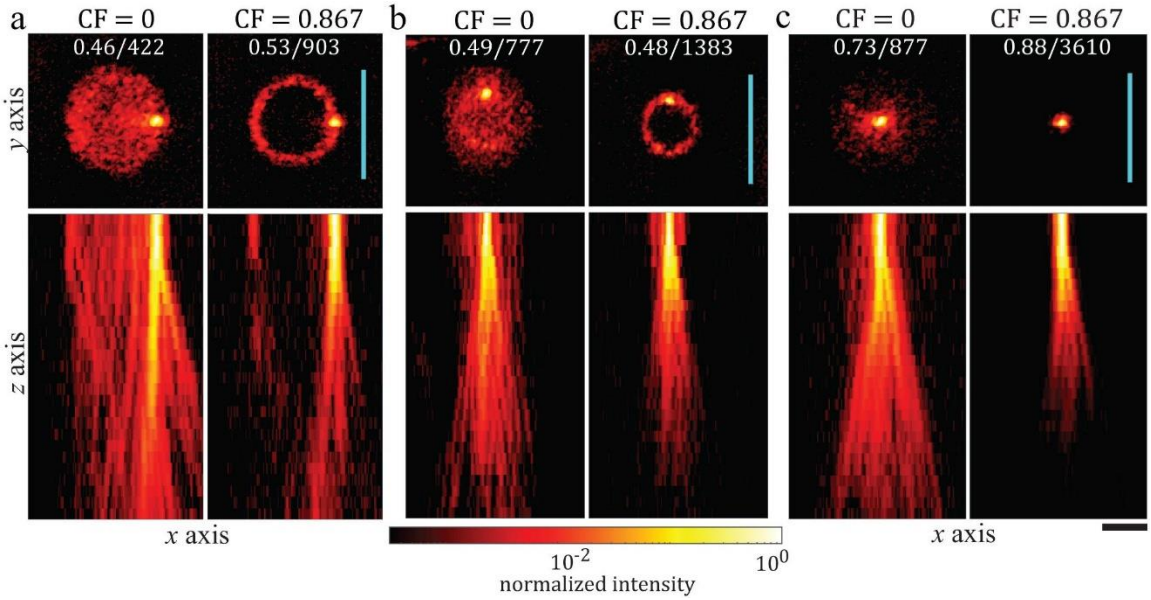

Figure 3.34: 3D PSF of the holographic endoscope with different extent of light filtration in the side-view mode. a-c, Lateral point spread functions (PSF) measured using a sub-resolution fluorescent microsphere (dia 0.82 μm) for three different focal points (top) and axial PSF for each focal point (bottom). Each point is imaged without confocal filtering and with a CF = 0.867. The values of EPR/EEF are given for each focal point. The blue lines mark the edge of the FOV of the MMF´s distal end. Scale bar is 20 μm.

For the same CF the EPR values increase by 20 and 15 % for a focal point in $0.8r$ and in the middle of the FOV, respectively, while for the $0.4r$ there has been decrease by 2%. Although the EPR is smaller, the light attenuation outside the focus is still fully apparent. Since the shape of the focal point can affect the resulting EPR, the smaller or uneven focal point can thus cause decrease of the EPR. Therefore, the Gaussian fit can give inaccurate measurement.

Also a significant attenuation of light from the out-of-focus planes, which can be clearly seen from the *x*-*z* projections in bottom panels of Fig. 3.34, where the points in *x* are a sum of intensities along the *y* axis, for each *x*-*y* plane and the azimuthal averages shown in Fig. 3.35. The confocal effect of suppression of the out-of-focus light is also demonstrated in Figure 3.36.

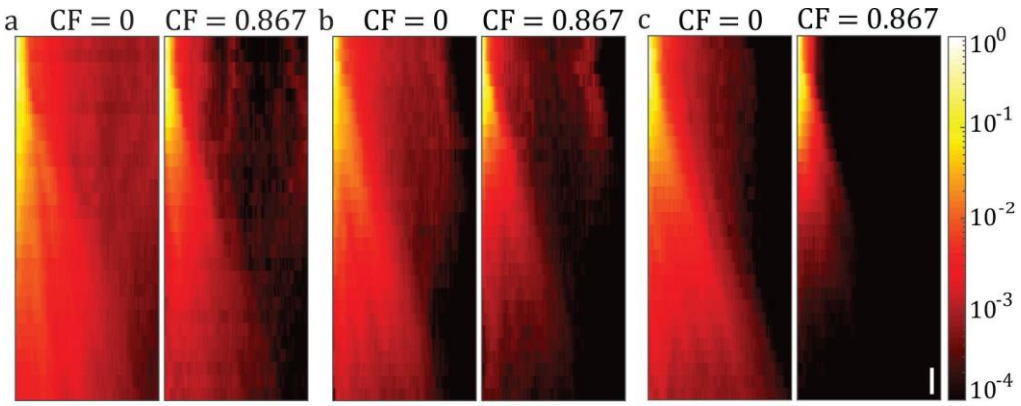

Figure 3.35: Azimuthally-averaged intensity profiles of the PSFs in the axial plane for focal points at three different positions in the FOV (a-c). Scale bar is 10 μm.

The graph shows total intensity in each axial plane without confocal filtration and for the tested CF. The measured data are fitted again by a Laplace function. In both cases, non-confocal detection and tested CF, the increased intensity at the beginning indicates that the microsphere is in the focus of the illumination focal point. The subsequent progress shows that with increasing distance of the microspere of the fibre, the intensity decreases. Even though the total intensity for the case of the confocal filtration is lower, the attenuation of the out-of-focus light and the speckled background at each plane can be observed. The strongest suppression of the out-of-focus signal and the speckled background can be observed for the focal point in the middle of the FOV (Fig. 3.36c), where the intensity dropped very fast, already 30 μm from the focused point. The closer the focal point is radially from the edge to the centre of the FOV, the stronger the confocal effect can be observed. Positive values of *x* are towards the fibre facet and negative values refers in direction away from it.

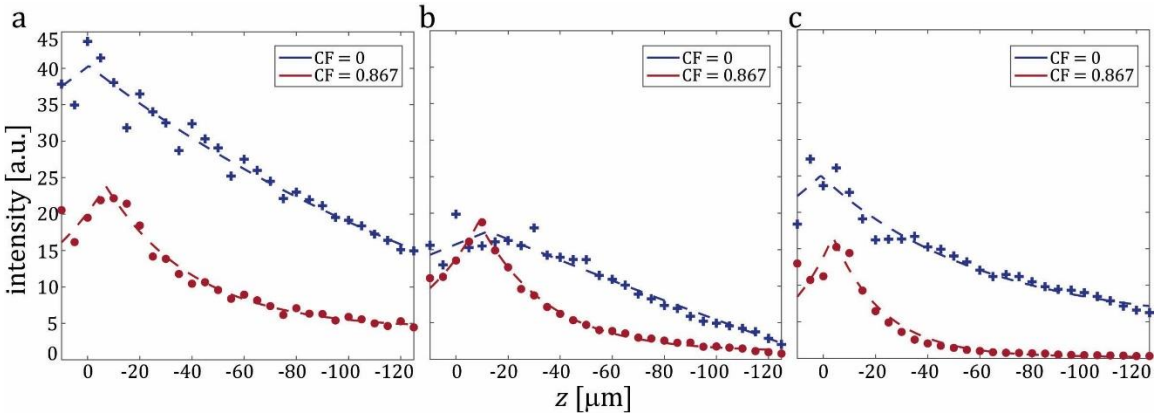

Figure 3.36: Total intensity in different planes along the optical axis z. The measured values of focal points at three different positions: 0.8*r* (a), 0.4*r* (b) and in the middle (c) are fitted by Laplace function and the fits are rendered as dashed lines.

Confocal imaging of a phantom sample in the side-view mode

To verify the effect of attenuation of the out-of-focus light and of the background signal demonstrated in previous measurement, we tested the imaging performance in a 3D model sample of fluorescent microspheres (0.82 μm in diameter) dispersed in an agarose gel in a volumetric ratio of 1:1000. Figure 3.37 shows two example FOVs imaged at depth of 70 μm and 370 μm, respectively. Also in this 3D model sample, the out-of-focus light is clearly attenuated after confocal filtration.

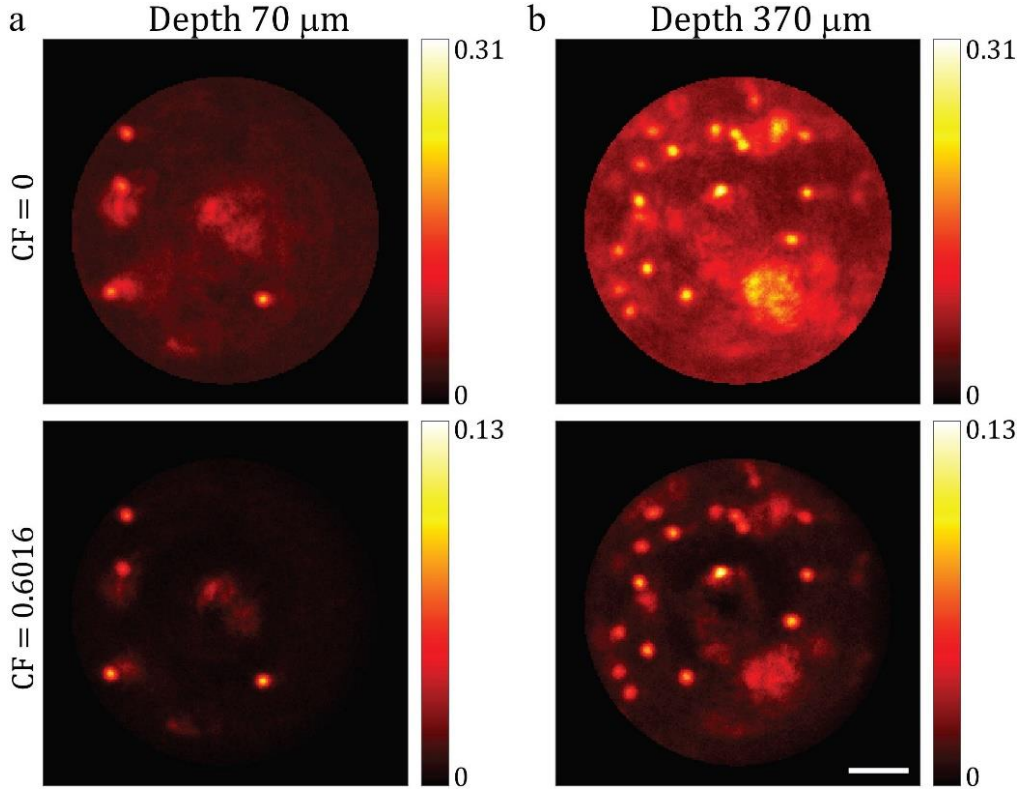

Figure 3.37: Side-view imaging of a 3D model sample of fluorescent microspheres (dia 0.82 μm) dispersed in agar at depth 70 μm (a) and 370 μm (b). Confocal filtration leads to attenuation of the out-of-focus light. Scale bar is 10 μm.

4. Discussion and conclusions

Our first goal was building a holographic endoscope setup following previous work of [103] and bring it to routine high-resolution imaging of biological tissue. Our first main challenge was the stability of the imaging, which can be defined by the quality of the scanning focal point determined by the percentage representation of the total power in such calibrated spot. The major aspect affecting stability turned out to be temperature changes which have a strong impact on the DMD chip. During scanning the DMD chip is warming up and gets deformed. This results in deforming the modulated wavefront, which leads to a different layout of the output light due to the changed phase shifts of the ones measured in TM. This problem was solved by adding a thermoelectric cooler (TEC) with a Peltier chip and a heat sink at the back of the DMD. It works as a thermoregulator with feedback. The temperature changes also strongly affect the polarisation in single mode fibre. It was stabilized by adding a polariser plate at the output of the SMF2 before the beam reaches the DMD chip. This enabled to fully control the polarisation of the coherent beam. With these modifications we reached a stability of the focal spot for 50 hours with only minor changes of the power ratio.

The stability of the system was tested on imaging of fluorescent microspheres both in 2D and 3D. In order to refocus in the sample, the user can either move the probe with respect to the tissue or refocus the scanning spot. We implemented here refocusing by acquisition of the TM at different working distances from the distal fibre facet. This allowed us volumetric imaging and focusing closer to the objects of interest. This is important particularly for *in vivo* imaging, where moving of the probe disrupts the tissue and displaces the cells of interest.

In order to enhance the capacity of the endoscope for high-resolution imaging, we proposed two computational algorithms for image post-processing that enhance it's contrast and thus the resolution. In this approach, the sample is reconstructed using measurement of the spatial intensity profiles of all focal points with their speckled background - the "muddy modes" and records of the sample image. One of the presented algorithms implements a regularised iterative inversion and the second algorithm employs a direct pseudo-inversion calculated by a singular value decomposition (SVD). The iterative algorithm called here the PN-based method represents a "more correct" model since it respects the Poisson noise distribution in the image, and it relies on an iterative calculation of a set of equations for every single image. The pseudo-inversion, called here the IIN-based method, on the other hand does not respect Poisson distribution of noise in images. However, it allows to use a simple last-square minimization assuming the Gaussian type of noise with constant variance. Thus, the solution can be calculated using the SVD which constitutes a simple vector-matrix multiplication for every image. Both methods were regularised using the Tikhonov regularisation with the regulariser strength λ. Enhancement of different spatial frequencies depend directly on λ. Both methods yield images with increased contrast for all spatial frequencies present in the image, evaluated using an USAF target sample.

Using the PN-based method, the contrast of all analysed spatial frequencies in our sample can be enhanced by up to $> 68\%$. Moreover, all spatial frequencies reach the maximum contrast within the same interval $1.5 \times 10^{-6} \leq \lambda \leq 5 \times 10^{-6}$. The PSNR and SSIM metrics reporting image quality in the fidelity of the reconstructed image to the "ground truth" and the visual impact of luminance, contrast and structure can be enhanced up to 14% and 29% respectively. Importantly, the regularised PN-based inversion yields a wide interval of $\lambda < 6 \times 10^{-5}$, for which all three image quality criteria are enhanced. Selecting a λ from this range allows fine-tuning of the image quality towards maximum contrast enhancement or PSNR and SSIM, respectively. The reconstruction of a single frame with this method takes ~ 21 seconds using a computational server equipped with 4 Intel Xeon Gold 6126 CPUs.

In the IIN-based inversion, the enhancement of image quality is given also by λ but its range is additionally limited by the presence of negative values in the reconstructions. We set a limit on λ accepting a maximum 1% of image pixels being negative. Therefore, the transformation yields enhanced image quality in a narrow interval $0.16 \leq \lambda \leq 0.18$. The contrast of all frequencies can be enhanced up to at least 69%, which is comparable to the PN-based inversion. Both PSNR as well as SSIM are enhanced in the same interval of λ by maximum of 10% and 26%, respectively as compared to 14% and 29% in the case of the PN-based inversion. Although the IIN-based method does not use the correct model for noise, it can be calculated as a pseudo-inverse using SVD which constitutes a simple vector-matrix multiplication for every image. The initial computation of matrix $\mathbf{M}+'$ in the regularized SVD procedure takes 15 minutes using the same computational power. The reconstruction of every additional frame however takes only ~ 0.2 seconds which can be highly advantageous in reconstructions of videos with fast feedback.

We also demonstrated that λ derived from one image can be successfully applied to the reconstruction of a series of images of a changing FOV from the same as well as different sample. (PN and IIN in Fig. 3.18 and in Visualization1).

The performance of PN and IIN-based reconstruction algorithms is dependent on the level of detected photons. Therefore, the methods and their comparison cannot be considered universal. The presented results were obtained with a photon count typically in a range 2000 in a single muddy mode. With decreasing signal to noise, the iterative algorithm is likely to become more advantageous yielding better results while the direct inversion will tend to amplify the noise in the SVD process.

Finally, the presented methods have been meant to be applied for image enhancement of biological specimens, however the presented form in this work is limited only to planar (2D) samples. Nevertheless, the concepts can be extended to the third dimension paving the way to reconstructions of volume samples such as tissue *in vivo*.

Considering the limitations of 1-photon fluorescence imaging I was looking for a suitable animal model for brain imaging (Section 3.5.1). This presumes bright fluorescent indicators and sparse labeling of cells in the dense brain tissue. Limited by the regulations of our animal facility we opted for crossbreeding of mouse lines in the Cre-lox breeding system which enable to express the selected fluorescent protein in a specific cell type. By cross-breading of a transgenic mouse line B6.Cg-*Gt(ROSA)26Sor*$^{tm14(CAG\text{-}tdTomato)Hze}$/J

and Cre-recombinase-expressing mouse line B6;129S6-Tg(Camk2a-cre/ERT2)1Aibs/J we obtained offsprings with tdTomato expressed in excitatory neurons. Additionally, we limited the fluorescence expression by injection of tamoxifen (Section 3.5.1.). Endoscopic imaging of fixed brain slices of this tissue showed however that the density is still quite high, and the contrast of images is not satisfactory (Section 3.5.3.).
This has led the motivation to upgrade the technology in order to limit the out-of-focus signal.

The proposed method relies confocal filtration of light using a novel probe of a GRIN-MMF spliced on a SI-MMF. This probe images light coming from a focal point into a defined annular ring in the far field of the proximal fibre facet [53]. Light coming from radially different positions appear outside of this ring and can therefore be separated. Light coming from axially different positions will appear defocused in the far field and its contribution to the detected signal can therefore be minimized. We used a second DMD and applied confocal ring masks in order to filter the light. The thickness of the ring-mask displayed on DMD2 determines the extent of signal filtration and we call it here the "confocal factor (CF)". A higher CF corresponds to a thinner ring-mask facilitating stronger light filtration, similarly to a confocal pinhole in classical far-field laser scanning confocal microscopy (CLSM).

As a proof of concept, we have imaged sub-resolution fluorescence microspheres and demonstrated that the presented confocal filtering of signal leads to a significant attenuation of the out-of-focus light both in the focal plane and also axially. This was quantified by the effective enhancement factor (EEF) and effective power ratio (EPR) reaching up to 310% and 80% (Fig. 3.28). The actual EEF and EPR values for the wide-field PSF are somewhat lower than was previously reported [**103**]. The lower values can be attributed to the fact, that it was measured using fluorescent microspheres rather than the focal point illumination directly.

The confocal effects were also demonstrated in imaging of a 3D sample of fluorescent microspheres dispersed in agar. The background signal and signal from outside the focal plane is successfully attenuated (Fig. 3.31). Importantly the confocal effect has been demonstrated by *ex vivo* imaging of brain slices expressing tdTomato in a population of excitatory neurons (Fig. 3.32). Also here, the background signal is clearly attenuated, which leads to an increase of image contrast and thus resolution manifested by the emergence of thin neuronal processes (Fig. 3.32a and c). The attenuation of the out-of-focus signal shows e.g. as the vanishing of a putative cell body (Fig. 3.32b).

Comparing with classical confocal microscopy which de-scans the pinhole for every *x*, *y* position, our filtration works only in a single dimension in polar coordinates. This means that light coming from azimuthally different positions but the same radius from the centre will share the same ring-mask. As a consequence, the detected signal from a single focal point at a radial distance *r* will be contaminated by the background signal coming from a ring with the same radius (Fig. 3.28b and c).

The parameters of masks are optimised for signal detection from the focal plane. Annular rings of the same thickness given by the CF, decrease the central diameter for focal points with decreasing radial distance in the focal plane down to an experimentally measured minimum radius. The signal intensity coming from axially different planes however is modulated by the area of the masks which is decreasing towards the middle. Scanning points with a decreasing radial distance in the focal plane correspond to annular ring masks with a decreasing radius. Decreasing the mask radius more than the theoretical resolution limit will lead to a decrease in the detected intensity of the corresponding central points. In practice, the intensity-decrease artifact appears even for a mask of a bigger diameter. Therefore, we measured the minimum mask diameter experimentally aiming for zero intensity drop in the centre of an image of a 2D homogeneous sample. This is why we can sometimes see an intensity dip in the middle of confocal images of 3D samples (Fig. 3.32a, b).

Similarly, to classical CLSM, the amount of detected photons in the confocal endo-microscopy is decreased due to the filtration process. Using the maximal CF, we can lose approximately more than 50% of the total light compared to non-confocal imaging (Fig. 3.30) It is typically compensated for by increasing illumination intensity, paying attention not to cause photobleaching.

As the next goal we aimed at implementing this confocal principle through the side-view probes which are to be used in imaging in vivo. We tested again the suppression of signal by scanning a sub-resolution fluorescence microsphere which revealed a significant increase of the effective enhancement factor (EEF) and effective power ratio (EPR) by up to 314% and 20%, respectively (Fig. 3.34) within the focal plane. Also the light from out-of-focus planes is clearly attenuated (Figures 3.34b, 3.35 and 3.36). These effects were also demonstrated in imaging of a 3D sample of fluorescent microspheres dispersed in agar (Fig. 3.37).

All the confocal experiments were carried out with step index and graded-index MMFs with a low NA of 0.22 and 0.275 and core diameters of 50 μm and 62.5 μm, respectively. Although the effects of confocal filtration are already undisputable, they are expected to be much more pronounced using fibres with higher NA and bigger core. As in the classical CLSM, confocal holographic endo-microscopy will open the door for imaging samples with a denser expression of fluorescent indicators. Thus, it increases the number of imaged cells per unit of time. In functional imaging, such as intracellular calcium, it will facilitate easier detection of spikes from individual cells due to decreased crosstalk from neuropil and other cells. Therefore, the next step, as a continuation of this work, is to apply this novel probe in vivo for imaging deep in the brain tissue. A small form factor of the probe promises funnelling confocal fluorescence imaging to unprecedented depth in a minimally invasive manner. This work has brought a strong base and new knowledge for a further shift towards *in-vivo* imaging of brain tissue in a living animal.

To conclude my work, we are equipped now with an ultra-thin endoscope setup which is capable of stable imaging of fluorescent samples in the range of hours featuring

the possibility to refocus within the sample without moving the probe. The acquired imaging can be further enhanced via computational post-processing. Moreover, this setup has been enriched by a confocal module which allows to significantly attenuate the out-of-focus light and is therefore much more suitable for imaging in the dense brain tissue.

List of abbreviations

CF	Confocal factor
CGH	Computer-generated hologram
CLSM	Confocal laser scanning microscopy
CT	Computation tomography
CTF	Contrast transfer function
DMD	Digital micro-mirror device
DNA	Deoxyribonucleic acid
EEF	Effective enhancement factor
EPR	Effective power ratio
fMRI	Functional magnetic resonance imaging
FOV	Field of view
GRIN	Gradient index
IIN	Intensity independent noise
LC-SLM	Liquid crystal-based spatial light modulator
MEMS	Microelectromechanical system
MMF	Multi-mode fibre
NA	Numerical aperture
NIR	Near-Infra red
NMR	Nuclear magnetic resonance
OPO	Optical parametric oscillator
PBS	Phosphate Buffered Saline
PCR	Polymerase chain reaction
PET	Positron emission tomography
PFA	Paraformaldehyde
PIM	Propagation-invariant mode
PMT	Photomultiplier tube
PN	Poisson noise
PR	Power ratio
PSNR	Peak signal-to noise ratio
SI	Step-index
SLM	Spatial light modulator
SMF	Single-mode fibre
SSIM	Structural Similarity Index
TEC	Thermoelectric cooler
TM	Transmission matrix

References

[1] Waterson, R.H., Lindblad-Toh, K., Birney, E., Rogers, J., Abril, J.F., Agarwal, P. et al. Initial sequencing and comparative analysis of the mouse genome. Nature, 420(6915): 520-62, 2002. https://doi.org/10.1038/nature01262.

[2] Čižmár, T. Exploiting multimode waveguides for in vivo imaging, SPIE, 2015.asas

[3] Suzuki, T., Matsuzaki, T., Hagiwara, H., Aoki, T. and Takata, K. Recent Advances in Fluorescent Labeling Techniques for Fluorescence Microscopy. *Acta Histochem Cytochem*, 40(5), 2007. https://doi.org/10.1267/ahc.07023.

[4] Leuner, B. and Gould, E. Structural Plasticity and Hippocampal Function. *Annual Review of Psychology*, 61, 2010. https://doi.org/ 10.1146/annurev.psych.093008.100359.

[5] Krezymon, A., Richetin, K., Halley, H., Roybon, L., Lassalle, J.-M., Francès, B., Verret, L., and Rampon, C. Modifications of Hippocampal Circuits and Early Disruption of Adult Neurogenesis in the Tg2576 Mouse Model of Alzheimer's Disease. *PLoS One*, 8 (9) 2013. https://doi.org/10.1371/journal.pone.0076497.

[6] Yang, W., Yuste, R. In vivo imaging of neural aktivity, *Nature Methods*, 14, 2017. https://doi.org/ 10.1038/nmeth.4230.

[7] Kerr, J.N.D., Greenberg, D.S., Helmchen, F. Imaging input and output of neocortical networks in vivo. *Proc Natl Acad Sci USA*, 102, 2005. https://doi.org/ 10.1073/pnas.0506029102.

[8] Greenberg, D.S., Houweling, A.R. and Kerr, J.N.D. Population imaging of ongoing neuronal activity in the visual cortex of awake rats. *Nature Neuroscience*, 11, 2008. https://doi.org/ 10.1038/nn.2140.

[9] Iadecola, C. The Neurovascular Unit Coming of Age: A journey through Neurovascular Coupling in Health and Disease. *Neuron Review*, 96, 2017. https://doi.org/10.1016/j.neuron.2017.07.030.

[10] Devor, A., Dunn, A.K., Andermann, M.L., Ulbert, I., Boas, D.A., Dale, A.M. Coupling of Total Hemoglobin Concentration, Oxygenation, and Neural Activity in Rat Somatosensory Cortex. *Neuron*, 39, 2003. https://doi.org/10.1016/s0896-6273(03)00403-3.

[11] Takano, T., Tian, G.F., Peng, W., Lou, N., Libionka, W., Han, X. and Nedergaard, M. Asctrocyte-mediated control of cerebral blood flow. *Nature Neuroscience*, 9(2), 2006. https://doi.org/ 10.1038/nn1623.

[12] Devor, A., Sakadžić, S., Saisan, P.A., Yaseen, M.A., Roussakis, E., Sirnivasan, V.J., Vinogradov, S.A., Rosen, B.R., Buxton, R.B., Dale, A.M. and Boas, D.A. „Overshoot"of O_2 Is Required to Maintain Baseline Tissue Oxygenation at Locations Distal to Blood Vessels. *The Journal Of Neuroscience*, 31(38), 2011. https://doi.org/10.1523/JNEUROSCI.1968-11.2011.

[13] Bolay, H., Reuter, U., Dunn, A.K., Huang, Z., Boas, D.A. and Moskowitz, M.A. Intrinsic brain activity triggers trigeminal meningeal afferents in a migraine model. *Nature Medicine*, 8, 2002. http://doi.org/10.1038/nm0202-136

[14] Latychevskaia T., Lateral and axial resolution criteria in incoherent and coheren optics and holography, near- and far-field regimes. *Applied Optics*, 58(13), 2019. http://doi.org/ 10.1364/AO.58.003597

[15] Kodach, V.M. Wavelength-dependent NIR light penetration depth. In *Development of functional near-infrared optical coherence tomography*. Disertation thesis. University Of Amsterdam. 114, 2012. https://hdl.handle.net/11245/1.385859.

[16] Helmchen, F. Denk, W. Deep tissue two-photon microscopy. *Nature Methods*, 2: 932-940, 2005. http://doi.org/ 10.1038/NMETH818.

[17] Van Staveren, H.J., Moes, C.J.M., Van Marie, J., Prahl, S.A. and Van Gemert, M.J.C. Light scattering in Intralipid-10% in the wavelength range of 400-1100 nm. *Applied Optics*, 30, 1991. http://doi.org/10.1364/AO.30.004507.

[18] Mourant, J.R., Fuselier, T., Boyer, J., Johnson, T.M. and Bigio, I.J. Predictions and measurements of scattering and absorption over broad wavelength ranges in tissue phantoms. *Applied Optics*, 36 (4), 1997. http://doi.org/10.1364/ao.36.000949.

[19] Pogue, B.W. and Patterson, M.S. Review of tissue simulating phantoms for optical spectroscopy, imaging and dosimetry. *Journal of Biomedical Optics*, 11(4), 2006. http://doi.org/ 10.1117/1.2335429.

[20] Schmitt, J.M., Xiang, S.H. and Yung, K.M. Differential absorption imaging with optical coherence tomography. *Journal of the Optical Society of America A-Optics Image Science and Vision*, 15, 1998. http://doi.org/10.1364/JOSAA.15.002288.

[21] Cox, A.J., DeWeerd, A.J. and Linden, J. An experiment to measure Mie and Rayleigh total scattering cross sections. American Journal of Physics, 70, 620, 2002. https://doi.org/10.1119/1.1466815.

[22] Yaroslavsky, A.N., Schulze, P.C., Yaroslavsky, I.V., Schober, R., Ulrich, F. and Schwarzmaier, H.-J. Optical properties of selected native and coagulated human brain tissues *in vitro* in the visible and near infrared spectral range. *Physics in Medicine & Biology* 47(12), 2002. http://doi.org/10.1088/0031-9155/47/12/305.

[23] Kleinfeld, D., Mitra, P.P., Helmchen, F. and Denk, W. Fluctuations and stimulus-induced changes in blood flow observed in individual capillaries in layers 2 through 4 of rat neocortex. *Proceedings of the National Academy of Sciences*, 95(26), 1998. https://doi.org/10.1073/pnas.95.26.15741.

[24] Oheim, M., Beaurepaire, E., Chaigneau, E., Mertz, J., Charpak, S. Two-photon microscopy in brain tissue: parameters influencing the imaging depth. *Journal of Neuroscience Methods*, 111(1), 2001. https://doi.org/10.1016/s0165-0270(01)00438-1.

[25] Booth, M.J. and Wilson T. Refractive-index-mismatch induced aberrations in single-photon and two-photon microscopy and the use of aberration correction. *Journal of Biomedical Optics*, 6(3), 2001. https://doi.org/10.1117/1.1382808.

[26] Brakenhoff, G.J., Van der Voort, H.T., Van Sprosen, E.A., Linnemans, W.A. and Nanninga, N. Three-dimensional chromatin distribution in neuroblastoma nuclei shown by confocal scanning laser microscopy. *Nature*, 317(6039), 1985. https://doi.org/10.1038/317748a0.

[27] White, J.G., Amos, W.B. and Fordham, M. An evaluation of confocal versus conventional imaging of biological structures by fluorescence light microscopy. *The Journal of Cell Biology*, 105(1):41-48, 1987. https://doi.org/ 10.1083/jcb.105.1.41.

[28] Pawley, J.B. Handbook of Biological Confocal Microscopy. Third edition, Springer Science & Business Media, LLC, New York. 2006.

[29] Wilson, T. and Sheppard C. Theory and Practice of Scanning Optical Microscopy. Academic Press INC. London, ISBN 0-12-757760-2 LCCCN 83-73235, 1984.

[30] Ntziachristos V. Going deeper than microscopy: the optical imaging frontier in biology. *Nature Methods*, 7(8): 603-14, 2010. https://doi.org/10.1038/nmeth.1483.

[31] Wilson, T. et al. (ed.). *Confocal microscopy*. London: Academic press, 1990.

[32] Fouquet C., Gilles J.F., Heck N., Dos Santos M., Schwartzmann R., Cannaya V., Morel, M.-P., Davidson, R.S., Trembleau, A. and Bolte, S. Improving Axial Resolution in Confocal Microscopy with New High Refractive Index Mounting Media. *PLoS ONE*, 10(3): e0121096, 2015. https://doi.org/10.1371/journal. pone.0121096.

[33] Semwogerere, D. and Weeks, E.R. Confocal Microscopy. *Encyclopedia of Biomaterials and Biomedical Engineering*, 2005. https://doi.org/ 10.1081/E-EBBE-120024153.

[34] Wilson, T. Resolution and optical sectioning in the confocal microscope. *Journal of Microscopy*, 244:113-121, 2011. https://doi.org/ 10.1111/j.1365-2818.2011.03549.x

[35] Schermelleh L., Heintzmann R. and Leonhardt H. A guide to super-resolution fluorescence microscopy, *The Journal of Cell Biology*, 190(2), 165–175, 2010. https://doi.org/10.1083/jcb.201002018.

[36] Centonze V.E. and White J.G. Multiphoton Excitation Provides Optical Sections from Deeper within Scattering Specimens than Confocal Imaging. *Biophysical Journal*, 75: 2015-2024, 1998. https://doi.org/10.1016/S0006-3495(98)77643-X.

[37] Sadegh, S., Yang, M.H., Ferri, Ch.G.L., Thunemann, M., Saisan, P.A., Wei, Z., Rodriguez, E.A., Adams, S.R., Kilic, K., Boas, D.A., Devor A. and Fainman, Y. efficient non-degenerate two-photon excitation for fluorescence microscopy. Optics Express, 27(20): 28022-28035, 2019. https://doi.org/10.1364/OE.27.028022.

[38] Helmchen, F. Two-Photon Functional Imaging of Neuronal Activity. *In Vivo Optical Imaging of Brain Function*, second edition, Boca Raton, Frosting RD, editor (2009).

[39] Tsai, P.S. and Kleinfeld, D. In Vivo Two-Photon Laser Scanning Microscopy with Concurrent Plasma-Mediated Ablation Principles and Hardware Realization. *In In Vivo optical Imaging of Brain Function*. CRC Press/Taylor and Francis. ISBN-13: 978-1-4200-7684-4 Second edition. 2009.

[40] Costanzo, V. and Constanzo, M. Intravital Imaging with Two-Photon Microscopy: A Look into the Kidney., *Photonics*, 9, 294, 2022. https://doi.org/10.3390/photonics9050294.

[41] Zipfel, W.R., Williams, R.M. and Webb, W.W. Nonlinear magic: multiphoton microscopy in the biosciences. *Nature Biotechnology*, 21(11), 2003. https://doi.org/ 10.1038/nbt899

[42] Hillman E.M.C. Optical brain imaging *in vivo*: techniques and applications from animal to man. *Journal of Biomedical Optics*, 12(5), 051402, 2007. https://doi.org/10.1117/1.2789693.

[43] Kobat D., Horton, N.G. and Xu Ch. *In vivo* two-photon microscopy to 1.6-mm depth in mouse cortex. *Journal of Biomedical Optics*, 16(10), 106014, 2011. https://doi.org/10.1117/1.3646209.

[44] Horton N.G., Wang, K., Kobat, D., Clerk, C.G., Wise, F.W., Schaffer, Ch.B. and Xu Ch. In vivo three-photon microscopy of subcortical structures within an intact mouse brain. Nature Photonics, 7(3): 205-209, 2013. https://doi.org/10.1038/nphoton.2012.336.

[45] Liu, H., Zhuang, Z., He, J., Tong, S., He, Ch., Deng, X., Song, G., Qiu, P. and Wang, K. High-energy polarized soliton synthesis and its application to deep-brain 3-photon microscopy in vivo. *Optics Express*, 27(11): 15309-15317, 2019. https://doi.org/10.1364/OE.27.015309.

[46] Chen, X., Cheng, H., Deng, X., Tong, S., Li, J., Qiu, P. and Wang, K. Self-phase-modulated femtosecond laser source at 1603 nm and its application to deep-brain 3-photon microscopy in vivo. *Journal Of Biophotonics*, 2020, https://doi.org/10.1002/jbio.202000349.

[47] Dombeck D.A., Harvey Ch.D., Tian L., Looger L.L., Tank D.W. Functional imaging of hippocampal place cells at cellular resolution during virtual navigation. *Natural Neuroscience*, 13(11), 2010. https://doi.org/10.1038/nn.2648.

[48] Vaidya, A.R., Pujara, M.S., Petrides, M., Murray, E.A. and Fellowe, L.K. Lesion studies in contemporary neuroscience. Trends of Cognitive Sciences, 23(8): 653-671, 2019. https://doi.org/10.1016/j.tics.2019.05.009.

[49] Jung, J.C., Mehta, A.D., Aksay, E., Stepnoski, R. and Schnitzer, M.J. In vivo mammalian brain imaging using one-and two-photon fluorescence microendoscopy. *Journal of Neurophysiology*, 92: 3121–3133, 2004. https://doi.org/10.1152/jn.00234.2004.

[50] Murayama, M., Pérez-Garci, E., Nevian, T., Bock, T., Senn, W. and Larkum, M.E. . Dendritic encoding of sensory stimuli controlled by deep cortical interneurons. *Nature*, 457: 1137, 2009. https://doi.org/10.1038/nature07663.

[51] Murayama, M., Pérez-Garci, E., Lüscher, H.-R. and Larkum, M.E. Fiberoptic system for recording dendritic calcium signals in layer 5 neocortical pyramidal cells in freely moving rats. *Journal of Neurophysiology*, 98: 1791–1805, 2007. https://doi.org/10.1152/jn.00082.2007.

[52] Knittel, J., Schnieder, L., G. Buess, Messerschmidt, B. and Possner, T. Endoscope-compatible confocal microscope using a gradient index-lens system. *Optics Communications*, 188(5-6): 267–273, 2001. https://doi.org/10.1016/S0030-4018(00)01164-0.

[53] Gmitro, A.F. and Aziz, D. Confocal microscopy through a fiber-optic imaging bundle. *Optics Letters*, 18(8): 565–567, 1993. https://doi.org/10.1364/OL.18.000565.

[54] Loterie, D., Goorden, S.A., Psaltis, D. and Moser, Ch. Confocal microscopy through a multimode fiber using optical correlation. *Optics Letters*, 40(24): 5754-5757, 2015. https://doi.org/10.1364/OL.40.005754.

[55] Engelbrecht, C.J., Johnston, R.S., Seibel, E.J. and Helmchen, F. Ultra-compact fiber-optic two-photon microscope for functional fluorescence imaging in vivo. *Optics Express*, 16(8): 5556–5564, 2008. https://doi.org/10.1364/OE.16.005556.

[56] Wilt, B.A., Burns, L.D., Wei Ho, E.T., Ghosh, K.K., Mukamel, E.A. and Schnitzer, M.J. Advances in light microscopy for neuroscience. *Annual Review of Neuroscience*, 32:435–506, 2009. https://doi.org/10.1146/annurev.neuro.051508.135540.

[57] Saleh, B.E.A., Teich, M.C. *Fundamentals of Photonics*, second edition, John Wiley & Sons, Inc, 2007, ISBN: 978-0-471-35832-9.

[58] Jung J.C. and Schnitzer M.J. Multiphoton endoscopy. *Optics Letters*, 28(11):902-904, 2003. https://doi.org/10.1364/OL.28.000902.

[59] Jung, J.C., Mehta, A.D., Aksay, E., Stepnoski, R. and Schnitzer, M.J. In vivo mammalian brain imaging using one-and two-photon fluorescence microendoscopy. *Journal of Neurophysiology*, 92(5):3121–3133, 2004. https://doi.org/10.1152/jn.00234.2004.

[60] Antonini, A., Sattin, A., Moroni, M., Bovetti, S., Moretti, C., Succol, F., Forli, A., Vecchia, D., Rajamanickam, V.P., Bertoncini, A., Panzeri, S., Liberale, C. and Fellin, T. Extended field-of-view ultrathin microendoscopes for high-resolution two-photon imaging with minimal invasiveness, *eLife*, 9:e58882, 2020. https://doi.org/10.7554/eLife.58882.

[61] Barretto R.P.J. and Schnitzer M.J. In vivo Optical Microendoscopy for Imaging Cells Lying Deep within Live Tissue. *Cold Spring Harb Protocols*, 2012(10): 1029-1034, 2012. https://doi.org/10.1101/pdb.top071464.

[62] Levene, M.J., Dombeck, D.A., Kasischke, K.A., Molloy, R.P. and Webb, W.W. In vivo multiphoton microscopy of deep brain tissue. *Journal of Neurophysiology*, 91(4): 1908-1912 (2004). https://doi.org/10.1152/jn.01007.2003.

[63] Flusberg, B.A., Jung, J.C., Cocker, E.D., Anderson, E.P. and Schnitzer, M.J. In vivo brain imaging using a portable 3.9 gram two-photon fluorescence microendoscope. *Optics Letters*, 30(17): 2272-2274, 2005. https://doi.org/10.1364/OL.30.002272.

[64] Huland, D.M., Brown, C.M., Howard, S.S., Ouzounov D.G., Pavlova, I., Wang, K., Rivera, D.R., Webb, W.W. and Xu, Ch. In vivo imaging of unstained tissues using long gradient index lens multiphoton endoscopic systems. *Biomedical Optics Express*, 3(5): 1077–1085, 2012. https://doi.org/10.1364/BOE.3.001077.

[65] Huland, D.M., Charan, K., Ouzounov D.G., Jones, J.S., Nishimura, N. and Xu, Ch. Three-photon excited fluorescence imaging of unstained tissue using a GRIN lens endoscope. *Biomedical Optics Express*, 4(5): 652-658, 2013. https://doi.org/10.1364/BOE.4.000652.

[66] Chien, Y.-F., Lin, J.-Y., Yeh, P.-T., Hsu, K.J., Tsai, Y.-H., Chen, S.-K. and Chu, S.-W. Dual Grin lens two-photon endoscopy for high-speed volumetric and deep brain imaging. Biomedical Optics Express, 12(1): 162-172, 2021. https://doi.org/10.1364/BOE.405738.

[67] Llewellyn M.E., Barretto R.P.J., Delp S.L. and Schnitzer M.J. Minimally invasive high-speed imaging of sarcomere contractile dynamics in mice and humans. *Nature*, 454(7205): 784-788, 2008. https://doi.org/10.1038/nature07104.

[68] Leiner, D.C. and Prescott, R. Correction of chromatic aberrations in GRIN endoscopes. *Applied Optics*, 22(3): 383-386, 1983. https://doi.org/10.1364/AO.22.000383.

[69] Sato, M., Sano, S., Watanbe, H., Kudo, Y. and Nakai, J. An aspherical microlens assembly for deep brain fluorescence microendoscopy. *Biochemical and Biophysical Research Communications*, 527(2): 447-452, 2020. https://doi.org/10.1016/j.bbrc.2020.04.009.

[70] Bortoletto, F., Bonoli, C., Panizzolo, P., Ciubotaru, C.D., and Mammano, F. Multiphoton Fluorescence Microscopy with GRIN Objective Aberration Correction by Low Order Adaptive Optics. *PLoS ONE*, 6(7): e22321 (2011). https://doi.org/ 10.1371/journal.pone.0022321.

[71] W. M. Lee, W.M. and S. H. Yun, S.H. Adaptive aberration correction of GRIN lenses for confocal endomicroscopy. *Optics Letters*, 36(23): 4608-4610, 2011. https://doi.org/10.1364/OL.36.004608.

[72] Wang Ch. and Ji N. Pupil-segmentation-based adaptive optical correction of a high-numerical-aperture gradient refractive index lens for two-photon fluorescence endoscopy. i, 37(11): 2001-2003, 2012. https://doi.org/10.1364/OL.37.002001.

[73] Wang Ch. and Ji N. Characterization and improvement of three-dimensional imaging performance of GRIN-lens-based two-photon fluorescence endomicroscopes with adaptive optics. *Optics Express*, 21(22): 27142-27154 (2013). https://doi.org/10.1364/OE.21.027142.

[74] Bocarsly, M.E., Jiang, W.-Ch., Wang, Ch., Dudman, J.T., Ji, N. and Aponte Y. Minimally invasive microendoscopy systemfor *in vivo* functional imaging of deep nuclei in the mouse brain. *Biomedical Optics Express*, 6 (11): 4546-4556, 2015. https://doi.org/10.1364/BOE.6.004546.

[75] Gosh, K.K., Burns, L.D., Cocker, E.D., Nimmerjahn, A., Ziv, Y., El Gamal, A. and Schnitzer, M.J. Miniaturized integration of a fluorescence microscope. *Nature Methods*, 8(10): 871-878, 2011. https://doi.org/ doi:10.1038/nmeth.1694.

[76] Göbel, W., Kerr, J.N., Nimmerjahn, A. and Helmchen, F. Miniaturized two-photon microscope based on a flexible coherent fiber bundle and a gradient-index lens objective. *Optics letters*, 29(21): 2521 - 2523, 2004. https://doi.org/10.1364/OL.29.002521.

[77] Hoy, C. L., Durr, N.J., Chen, P., Piyawattanametha, W., Ra, H., Solgaard, O. and Ben-Yakar, A.. Miniaturized probe for femtosecond laser microsurgery and two-photon imaging. *Optics Express*, 16(13): 9996-10005, 2008. https://doi.org/10.1364/OE.16.009996.

[78] Flusberg, B.A., Nimmerjahn, A., Cocker, E.D., Mukamel, E.A., Barretto, R.P.J., Jung, J.C. and Schnitzer, M.J. High-speed, miniaturized fluorescence microscopy in freely moving mice. *Nature Methods*, 5(11): 935-938, 2008. https://doi.org/10.1038/nmeth.1256.

[79] Laing B.T., Siemian J.N., Sarsfield S. and Aponte Y. Fluorescence microscopy for in vivo deep-brain imaging of neuronal circuits. Journal of Neuroscience Methods, 15(348): 109015, 2021. https://doi.org/10.1016/j.jneumeth.2020.109015.

[80] Barretto, R.P.J., Ko, T.H., Jung, J.C., Wang, T.J., Capps, G., Waters, A.C., Ziv, Y., Attardo, A., Recht, L. and Schnitzer, M.J. Time-lapse imaging of disease progression in deep brain areas using fluorescence microendoscopy. *Nature Medicine*, 17(2): 223-228, 2011. https://doi.org/10.1038/nm.2292.

[81] Mekhail, S.P., Arbuthnott, G., and Chormaic, S.N. Advances in Fibre Microendoscopy for Neuronal Imaging. *Optical Data Processing and Storage*, 2:30-42, 2016. https://doi.org/10.1515/odps-2016-0003.

[82] Delaney, P. and Martin Harris, M. Fiber-Optics in Scanning Optical Microscopy. In *Handbook of Biological Confocal Microscopy*, pages 508–515. Springer US, New York, USA, Third edition, 2006.

[83] Rector, D. and Harper, R. Imaging of hippocampal neural activity in freely behaving animals. *Behavioural brain research*, 42(2): 143-49, 1991. https://doi.org/10.1016/s0166-4328(05)80005-1.

[84] Rector, D., Poe, G. & Harper, R. Imaging of hippocampal and neocortical neural activity following intravenous cocaine administration in freely behaving cats. *Neuroscience*, 54(3): 633-41, 1993. https://doi.org/10.1016/0306-4522(93)90234-7.

[85] Ozbay, B.N., Losacco, J.T., Cormack, R., Weir, R., Bright, V.M., Gopinath, J.T., Restrepo, D. and Gibson, E.A. Miniaturized fiber-coupled confocal fluorescence microscope with an

electrowetting variable focus lens using no moving parts. *Optics Letters*, 40(11): 2553-2556, 2015. https://doi.org/10.1364/OL.40.002553.

[86] Engelbrecht, C.J., Voigt, F. and Helmchen, F. Miniaturized selective plane illumination microscopy for high-contrast *in vivo* fluorescence imaging. *Optics Letters*, 35(9): 1413-1415, 2010. https://doi.org/10.1364/OL.35.001413.

[87] Laemmel, E., Genet, M., Le Goualher, G., Perchant, A., Le Gargasson, J.-F. and Vicaut, E. Fibered Confocal Fluorescence Microscopy (Cell-viZio™) Facilitates Extended Imaging in the Field of Microcirculation. *Journal of Vascular Research*, 41(5): 400-411, 2004. https://doi.org/10.1159/000081209.

[88] Orth, A., Ploschner, M., Wilson, E.R., Maksymov, I.S. and Gibson, B.C. Optical fiber bundles: Ultra-slim light field imaging probes. Science Advances, 5(4), 2019. https://doi.org/ 10.1126/sciadv.aav1555.

[89] Flusberg B.A., Cocker E.D., Piyawattanametha W., Jung J.C., Cheung E.L.M. and Schnitzer M.J. Fiber-optic fluorescence imaging. *Nature Methods*, 2(12): 941-50, 2005. https://doi.org/10.1038/nmeth820.

[90] Giniunas, L., Juskaitis, R. and Shatalin, S.V. Scanning fibre-optic microscope. *Electronics Letters*, 27: 724-726, 1991. https://doi.org/ 10.1049/el:19910450.

[91] Kim, H.K., Digonnet, M.J.F., Kino, G.S., Shin, J. and Fan, S. Simulations of the effect of the core ring on surface and air-core modes in photonics bandgap fibers. *Optics Express*, 12(15): 3436-3442, 2004. https://doi.org/10.1364/OPEX.12.003436.

[92] M. Gu and C. J. R. Sheppard, Optik (Stuttgart) 86, 104 (1990).

[93] Čižmár, T. and Dholakia, K. Exploiting multimode waveguides for pure fibre-based imaging. *Nature Communication*, 3: 1027, 2012. https://doi.org/10.1038/ncomms2024.

[94] Papadopoulos, I.N., Farahi, S., Moser, C. and Psaltis, D. High-resolution, lensless endoscope based on digital scanning through a multimode optical fiber. *Biomedical Optics Express*, 4(2): 260–270, 2013. https://doi.org/10.1364/BOE.4.000260.

[95] Szabo, V., Ventalon, C., De Sars, V., Bradley, J. and Emiliani, V. Spatially selective holographic photoactivation and functional fluorescence imaging in freely behaving mice with a fiberscope. *Neuron*, 84(6): 1157-69, 2014. https://doi.org/10.1016/j.neuron.2014.11.005.

[96] Xu, H.T., Pan, F., Yang, G. and Gan, W.B. Choice of cranial window type for in vivo imaging affects dendritic spine turnover in the cortex. *Nature Neuroscience*, 10(5): 549-51, 2007. https://doi.org/10.1038/nn1883.

[97] Moshayedi, P., Ng, G., Kwok, J.C.F., Yeo, G.S.H., Bryant, C.E., Fawcett, J.W., Franze, K. and Guck, J. The relationship between glial cell mechanosensitivity and foreign body reactions in the central nervous system. *Biomaterials*, 35(13): 3919-25, 2014. https://doi.org/10.1016/j.biomaterials.2014.01.038.

[98] Eguchi, M. and Horinouchi, S. Finite-element modal analysis of large-core multimode optical fibers. *Applied Optics*, 43(10): 2163-2167, 2004. https://doi.org/10.1364/AO.43.002163.

[99] Čižmár, T., Mazilu, M. and Dholakia, K. In situ wavefront correction and its application to micromanipulation. *Nature Photonics*, 4: 388-394, 2010. https://doi.org/10.1038/nphoton.2010.85.

[100] Čižmár, T., Dholakia, K. Shaping the light transmission through a multimode optical fibre: complex transformation analysis and applications in biophotonics. *Optics Express*, 19(20): 18871-18884, 2011. https://doi.org/10.1364/OE.19.018871.

[101] Mahalati, R.N., Gu, R.Y. and Kahn, J.M. Resolution limits for imaging through multi-mode fiber. *Optics Express*, 21(2): 1656-1668, 2013. https://doi.org/10.1364/OE.21.001656.

[102] Plöschner, M., Tyc, T. and Čižmár, T. Seeing through chaos in multimode fibres. *Nature Photonics*, 9:529-535, 2015. https://doi.org/10.1038/nphoton.2015.112.

[103] Turtaev, S., Leite, I.T., Altwegg-Boussac, T., Pakan, J.M.P., Rochefort, N.L. and Čižmár, T. High-fidelity multimode fibre-based endoscopy for deep-brain *in vivo* imaging. *Light: Science and Applications*, 7:92, 2018. https://doi.org/10.1038/s41377-018-0094-x.

[104] Wadsworth, W., Percival, R., Bouwmans, G., Knight, J., Birks, T., Hedley, and P. S. Russell, P.S., "Very high numerical aperture fibers," *Photonics Technology Letters*, 16: 843–845, 2004. https://doi.org/10.1109/LPT.2004.823689.

[105] Mosk, A.P., Lagendijk, A., Lerosey, G., and Fink, M. Controlling waves in space and time for imaging and focusing in complex media. *Nature Photonics*, 6: 283-292, 2012. https://doi.org/10.1038/nphoton.2012.88.

[106] Vellekoop, I.M. & Mosk, A. Universal Optimal Transmission of Light Through Disordered Materials. *Physical Review Letters*, 101:120601 2008. https://doi.org/10.1103/PhysRevLett.101.120601.

[107] Leonardo, R.D. and Bianchi, S. Hologram transmission through multi-mode optical fibers. *Optics Express*, 19(1): 247–254, 2011. https://doi.org/10.1364/OE.19.000247.

[108] Popoff, S., Lerosey, G., Fink, M., Boccara, A.C. and Gigan, S. Image transmission through an opaque material. *Nature Communications* 1(81), 2010. https://doi.org/10.1038/ncomms1078.

[109] Vellekoop, I.M. and Mosk, A. Focusing coherent light through opaque strongly scattering media. *Optics Letters*, 32(16): 2309–2311, 2007. https://doi.org/10.1364/OL.32.002309.

[110] Conkey, D.B., Brown, A.N., Caravaca-Aguirre, A.M. and Piestun, R. Genetic algorithm optimization for focusing through turbid media in noisy environments. *Optics Express*, 20(5): 4840–4849, 2012. https://doi.org/10.1364/OE.20.004840.

[111] Popoff, S.M., Aubry, A., Lerosey, G., Fink, M., Boccara, A.C. and Gigan, S. Exploiting the Time-Reversal Operator for Adaptive Optics, Selective Focusing, and Scattering Pattern Analysis. *Physical Review Letters*, 107(26): 263901, 2011. https://doi.org/10.1103/PhysRevLett.107.263901.

[112] Mounaix, M., Fontaine, N.K., Neilson, D.T. and Carpenter, J. Time reversal of optical waves. Frontier in Optics+Laser Science APS/DLS, 2019. https://doi.org/10.1364/FIO.2019.FTu6B.5.

[113] Papadopoulos, I.N., Farahi, S., Moser, C. and Psaltis, D. Focusing and scanning light through a multimode optical fiber using digital phase conjugation. *Optics Express*, 20(10): 10583–10590, 2012. https://doi.org/10.1364/OE.20.010583.

[114] Drémeau, A., Liutkus, A., Martina, D., Katz, O., Schülke, C., Krzakala, F., Gigan, S._ and Daudet, L. Reference-less measurement of the transmission matrix of a highly scattering material using a DMD and phase retrieval techniques. *Optics Express*, 23(9). 11898-1911, 2015. https://doi.org/10.1364/OE.23.011898.

[115] Popoff, S.M., Lerosey, G., Carminati, R., Fink, M., Boccara, A.C. and Gigna, S. Measuring the transmission Matrix in Optics: An Approach to the Study and Control of Light Propagation in disordered Media. *Physical Review Letters,* 104(10): 100601 2010. https://doi.org/10.1103/PhysRevLett.104.100601.

[116] Vasquez-Lopez, S. A., Koren, V., Plöschner, M., Padamsey, Z., Čižmár, T. and Emptage, N. J. Minimally invasive deep-brain imaging through a 50 μm-core multimode fibre. *bioRxiv,* 2018. https://doi.org/10.1101/289793.

[117] Ohayon, S., Caravaca-Aguirre, A., Piestun, R. and DiCarlo, J.J. Minimally invasive multimode optical fiber microendoscope for deep brain fluorescence imaging. Biomedical *Optics Express,* 9(4): 1492-1509, 2018. https://doi.org/10.1364/BOE.9.001492.

[118] Thorlabs, Inc.

[119] Leite, I. T., Turtaev, S., Jiang, X., Šiler, M., Cuschieri, A., Russell, P. St. J. and Tomáš Čižmár. Three-dimensional holographic optical manipulation through a high-numerical-aperture soft-glass multimode fibre. *Nature Photonics,* 12(7): 33-39, 2017. https://doi.org/10.1038/s41566-017-0053-8.

[120] Choi, Y., Yoon, C., Kim, M., Yang, T.D., Fang-Yen, C., Dasari, R.R., Lee, K.J. and Choi, W. Scanner-Free and Wide-Field Endoscopic Imaging by Using a Single Multimode Optical Fiber. Physical Review Letters, 109(20): 203901, 2012. https://doi.org/10.1103/PhysRevLett.109.203901.

[121] Turtaev, S. Leite, I.T., Mitchell, K.J., Padgett, M.J., Phillips, D.B. and Čižmár T. Comparison of nematic liquid-crystal and DMD based spatial light modulation in complex photonics. *Optics Express,* 25(24): 29874-29884, 2017. https://doi.org/10.1364/OE.25.029874.

[122] Sampsell J.B. Digital micromirror device and its application to projection displays. *Journal of Vacuum Science and Technology B,* 12,3242 1994. https://doi.org/10.1116/1.587506.

[123] Nesbitt R.S., Smith S.L., Molnar R.A. and Benton S.A., Holographic recording using a digital micromirror device, *SPIE,* 3637, 1999. https://doi.org/10.1117/12.343767.

[124] Kreis T., Aswendt P., Hoefling, R. Hologram reconstruction using a digital micromirror device. *Society of Photo-Optical Instrumentation Engineers,* 40(6): 926-933, 2001. https://doi.org/10.1117/1.1367346.

[125] Dudley D., Duncan W. and Slaughter J. Emerging Digital Micromirror Device (DMD) Applications, SPIE, 4985, 2003. 10.1117/12.480761.

126] Brown, B.R. and Lohmann, A.W. Complex spatial filtering with binary masks. *Applied Optics,* 5(6): 967–969, 1966. https://doi.org/10.1364/AO.5.000967.

[127] Chandrasekaran, S.N., Ligtenberg, H., Steenbergen, W. and Vellekoop, I.M. Using digital micromirror devices for focusing light through turbid media. *SPIE,* 8979, 897905, 2014. https://doi.org/10.1117/12.2038893.

[128] Gomez, A.D., Turtaev, S., Du, Y. and Čižmár, T. Near perfect focusing through multimode fibres, *Optics Express,* 30(7): 10645-10663, 2022. https://doi.org/10.1364/OE.452145.

[129] Phillips, D.B., Sun, M-J., Taylor, J.M., Edgar, M-P, Barnett, S.M., Gibson, G.G. and Padgett, M.J. Adaptive foveated single-pixel imaging with dynamic super-sampling.arXiv:1607.08236,2016. https://doi.org/10.48550/arXiv.1607.08236.

[130] Mitchell, K.J., Turtaev, S., Padgett, M.J., Čižmár, T. and Phillips, D.B. High-speed spatial control of the intensity, phase and polarization of vector beams using a digital micro-mirror device. *Optics Express,* 24(25): 29269-29282, 2016. https://doi.org/10.1364/OE.24.029269.

[131] Lee, W.-H. Binary computer-generated holograms. *Applied Optics*, 18(21): 3661–3669, 1979. https://doi.org/10.1364/AO.18.003661.

[132] Bianchi, S. and Di Leonardo, R. A multi-mode fiber probe for holographic micromanipulation and microscopy. *Lab on a Chip,* 12: 635–639, 2012. https://doi.org/10.1039/C1LC20719A.

[133] Rudolf, B., Du, Y., Turtaev, S., Leite, I.T. and Čižmár T. Thermal stability of wavefront shaping using a DMD as a spatial light modulator. *Optics Express*, 29(25): 41808-41818, 2021. https://doi.org/10.1364/OE.442284.

[134] Polikov, V.S., Tresco, P.A. and Reichert, W.M. Response of brain tissue to chronically implanted neural electrodes. *Journal of Neuroscience Methods,* 148(1): 1–18, 2005. https://doi.org/ 10.1016/j.jneumeth.2005.08.015.

[135] Bertero, M., Boccacci, P., Desiderà, G. and Vicidomini, G. Image deblurring with poisson data: from cells to galaxies. Inverse Problems, 25(12): 123006, 2009. http://iopscience.iop.org/0266-5611/25/12/123006.

[136] Karl,W. "3.6 - regularization in image restoration and reconstruction," in *Handbook of Image and Video Processing (Second Edition)*, A. Bovik, ed. (Academic, 2005), Communications, Networking and Multimedia, pp. 183 – V, 2nd.ed.

[137] Makitalo, M. and Foi, A. Optimal inversion of the ascombe transformation in low-count poisson image denoising. *IEEE Transactions on Image Processing*, 20(1): 99–109, 2011. https://doi.org/ 10.1109/TIP.2010.2056693.

[138] Wang, Z., Bovik, A., Sheikh, H. and Simoncelli, E. Image quality assessment: from error visibility to structural similarity. *IEEE Transactions on Image Processing*, 13(4): 600–612, 2004. https://doi.org/ 10.1109/TIP.2003.819861.

[139] Yu, Y.-C., Bultje, R.S., Wang, X. and Shi, S.-H.Specific synapses develop preferentially among sister excitatory neurons in the neocortex. Nature Letters, 458(7237): 501-504, 2009. https://doi.org/10.1038/nature07722.

[140] Mateo, C., Avermann, M., Gentet, L.J., Zhang, F., Deisseroth, K. and Petersen, C.C.H. In Vivo Optogenetic Stimulation of Neocortical Excitatory Neurons Drives Brain-State-Dependent Inhibition. *Current Biology*, 21(19): 1593-602, 2011. https://doi.org/ 10.1016/j.cub.2011.08.028.

[141] Miller, S.M. and Sahay, A. Functions of adult-born neurons in hippocampal memory interference and indexing. Nature Neuroscience, 22: 1565-1575, 2019. https://doi.org/10.1038/s41593-019-0484-2.

[142] Turcotte, R., Schmidt, C.C., Booth, M.J. and Emptage, N.J. Volumetric two-photon fluorescence imaging of live neurons using a mmultimode optical fiber. Optics Letters, 45(24): 6599-6602, 2020. https://doi.org/10.1364/OL.409464.

[143] Kakkava, E., Romito, M., Loterie, D., Stankovich, K., Moser, C. and Psaltis, D. Two-photon imaging and selective laser ablation of cochlea hair cells through a multimode fiber probe. *SPIE*, 10872, 2019. https://doi.org/10.1117/12.2510202.

[144] Loterie, D., Farahi, S., Papadopoulos, I., Goy, A., Psaltis, D. and Moser, C. Digital confocal microscopy through a multimode fiber. *Optics Express*, 23(18): 23845-23858, 2015. https://doi.org/10.1364/OE.23.023845.

[145] Loterie, D., Psaltis, D. and Moser, C. Confocal microscopy via multimode fibers: fluorescence bandwidth. SPIE, 9717, 2016. https://doi.org/10.1117/12.2208017.

[146] Leite I., Turtaev, S., Boonzajer Flaes, D.E. and Čižmár, T. Observing distant object with a multimode fiber-based holographic endoscope. *APL Photonics*, 6, 036112, 2021. https://doi.org/10.1063/5.0038367.

[147] Silveira, B.M., Pikálek, T., Stibůrek, M., Ondráčková, P., Jákl, P., Leite, I.T. and Čižmár, T. Side-view holographic endomicroscopy via a custom-terminated multimode fibre. *Optics Express*, 29(15):23083-23095, 2021. https://doi.org/10.1364/OE.426235.

[148] Stibůrek, M., Ondráčková, P., Tučková, T., Turtaev, S., Šiler, M., Pikálek, T., Jákl, P., Gomes, A., Krejčí, J., Kolbábková, P., Uhlířová, H. and Čižmár, T. Hair-thin endo-microscope for deep-brain in-vivo observations of neuronal connectivity, activity and blood flow dynamics. *Submitted* 2022.

Author's publications and other outputs

Journal contributions:

1. Tučková, T., Šiler, M., Boonzajer Flaes, D.E., Jákl, P., Turtaev, S., Krátký, S., Heintrmann, R., Uhlířová, H. and Čižmár, T. Computational image enhancement of multimode fibre-based holographic endo-microscopy: harnessing the muddy modes. *Optics Express*, 29(23): 38206-38220, 2021. https://doi.org/10.1364/OE.434848.
2. Stibůrek, M., Ondráčková, P., Tučková, T., Turtaev, S., Šiler, M., Pikálek, T., Jákl, P., Gomes, A., Krejčí, J., Kolbábková, P., Uhlířová, H. and Čižmár, T. Hair-thin endo-microscope for deep-brain in-vivo observations of neuronal connectivity, activity and blood flow dynamics. *Submitted* 2022.
3. Tučková, T., Pikálek, T., Stibůrek, M., Ondráčková, P., Turtaev, S., Šiler, M., Jákl, P., Kolbábková, P., Krejčí, J., Uhlířová, H. and Čižmár, T. Fluorescence confocal imaging via holographic endo-microscopy. *In preparation*.

Conference and workshop contributions:

1. Tučková, T., Jákl, P., Šiler, M., Trägardh, J., Hons, M., Pikálet, T., Dražanová, E., Krátká, L., Simpson S., Tyc, T., Uhlířová H., Čižmár, T. Multimode fibre-based endoscope for high resolution fluorescence imaging of bulk tissue (poster presentation), The 21st Czech-Polish-Slovak Optical konference on Wave and Quantum Aspects of Contemporary Optics, September 2018, Lednice, Czech Republic.
2. Tučková, T., Hons, M., Jákl, P., Šiler, M., Turtaev, S., Dražanová, E., Krátká, L., Trägardh, J., Pikálet, T., Tyc, T., Uhlířová H., Čižmár, T. Improving quality of optical fiber-based endoskopy for *in vivo* brain imaging (poster presentation). Neuroscience 2018, Society for Neuroscience, November 2018, San Diego, California, USA.
3. Tučková,T., Šiler, M., Heintzmann, R., Jákl, P., Uhlířová, H. Čižmár, T. Image enhancement in multi-mode fiber-based endoscopy imaging (oral presentation). ELMI 2019 - European Light Microscopy Initiative Meeting, Jun 2019, Brno, Czech Republic.
4. Tučková, T., Šiler, M., Boonzajer Flaes, D.E., Turtaev, S., Stibůrek, M., Pikálek, T., Heintzmann, R., Ondračková, P., Jákl, P., Hana Uhlířová, H. and Čižmár, T. Holografic endo-microscopy: imaging approaches (oral presentation). Laser61, October 2021, Lednice, Czech Republic.
5. Tučková, T., Šiler, M., Boonzajer Flaes, D.E., Jákl, P., Turtaev, S., Krátký, S., Heintzmann, R., Hana Uhlířová, H. and Čižmár, T. Computational image enhancement of multimode fibre-based holographic endo-microscopy using the *muddy modes* (poster presentation). FENS Forum 2022, International Neuroscience Conference, July 2022, Paris, France.
6. Stibůrek, M., Ondráčková P, Tučková, T., Turtaev, S., Šiler, M., Pikálek, T., Jákl, P., Gomés, A., Kolbábková, P., Krejčí, J., Uhlířová, H. and Čižmár, T. Hair-thin holographic endo-microscope for deep brain in vivo observations (poster presentation). 16th Multinational Congress on Microscopy, 16MCM, September 2022, Brno, Czech Republic.